

Thermo Electron Engineering Corporation, 85 First Avenue, Waltham, Massachusetts 02154

EMITTER CRYSTAL STRUCTURE STUDY  
FINAL TECHNICAL REPORT


by

G. Miskolczy, S. Kitrilakis, L. van Someren  
J. H. Weinstein

February 1964

Prepared for  
Jet Propulsion Laboratory  
Pasadena, California

Approved by:

  
S. S. Kitrilakis  
Research Manager



## TABLE OF CONTENTS

	<u>Page No.</u>
CHAPTER I - INTRODUCTION . . . . .	I-1
CHAPTER II - SUMMARY AND CONCLUSIONS . . . . .	II-1
CHAPTER III - PHOTOELECTRIC SCANNER . . . . .	III-1
A. PRINCIPLE OF OPERATION. . . . .	III-1
B. OPTICAL SYSTEM . . . . .	III-2
C. ELECTRONIC SCANNING SYSTEM. . . . .	III-4
D. PHOTOCURRENT DETECTION AND AMPLIFICATION SYSTEM . . . . .	III-4
E. DESCRIPTION OF PHOTOELECTRIC SCANNER CELL . . . . .	III-10
1. <u>Preliminary Model</u> . . . . .	III-10
2. <u>Advanced Model</u> . . . . .	III-10
F. RESULTS FROM PHOTOELECTRIC SCANNER. . . . .	III-11
1. <u>Preliminary Experiments</u> . . . . .	III-11
2. <u>Experimental Results</u> . . . . .	III-13
G. DISCUSSION. . . . .	III-14
CHAPTER IV - THERMIONIC SCANNER . . . . .	IV-1
A. PRINCIPLE OF OPERATION. . . . .	IV-1
B. THERMIONIC SCANNER CELL . . . . .	IV-1
1. <u>Preliminary Model</u> . . . . .	IV-1
2. <u>Advanced Model</u> . . . . .	IV-4
C. THERMIONIC SCANNING SYSTEM. . . . .	IV-5
D. SIGNAL DETECTION AND AMPLIFICATION . . . . .	IV-7
E. EXPERIMENTAL RESULTS FROM THERMIONIC SCANNER. . . . .	IV-7
1. <u>Preliminary Experiments</u> . . . . .	IV-7
2. <u>Experimental Results</u> . . . . .	IV-9





TABLE OF CONTENTS (Continued)

	<u>Page No.</u>
CHAPTER V - CONVERTER STUDIES . . . . .	V-1
A. GENERAL . . . . .	V-1
B. THE TEST VEHICLE . . . . .	V-1
C. INSTRUMENTATION . . . . .	V-2
D. PERFORMANCE TESTING . . . . .	V-4
E. WORK FUNCTION MEASUREMENTS . . . . .	V-7
CHAPTER VI - METALLURGICAL STUDIES . . . . .	VI-1
A. GENERAL . . . . .	VI-1
B. EXPERIMENTAL RESULTS . . . . .	VI-3
C. CONCLUSIONS . . . . .	VI-5

## CHAPTER I

### INTRODUCTION

This is the Final Report on the "Emitter Crystal Structure Study" under JPL Contract No. 950228 which is sponsored by NASA. The objective of the study was to develop a better understanding of the relationship among emitter crystal structure, emitter preparation, and emitter performance in order to determine methods for obtaining higher-performance thermionic converters.

Three areas of effort have been pursued to achieve the program objective. These are:

1. Metallurgical preparation and analysis of emitters;
2. Work function examinations of the same emitters in scanning-type devices where the cesium covered work function maps may be obtained under a wide range of equilibrium conditions;
3. Operation of the previously studied emitters in thermionic converter test vehicles.

In order to perform the work function mapping, two scanning devices were developed. Each required a proof-of-principle iteration before the actual test device was designed and fabricated. The proof-of-principle devices for both the thermionic and photoelectric scanners were successful, and two actual test devices were then completed and used extensively. Metallurgical techniques for preparation of a number of different emitter surfaces were developed, and a variety of surfaces were tested both in scanners and in thermionic converters.

The results, which are described in this report, have provided important insight into the emission physics of cesium converters and have provided a



wealth of data for the development of correlations. They have also confirmed earlier analytical predictions and broadened the base which is required for improvements in converter performance for future hardware application.



## CHAPTER II

### SUMMARY AND CONCLUSIONS

This program was primarily concerned with the relationship between the performance of a thermionic emitter and its metallurgical state. The first step in relating the two is the determination of the work function of emitter surfaces on a point-by-point basis. To accomplish this, two very highly specialized devices were developed. Each of these devices is capable of measuring the work function of a cesium-covered refractory surface on a point-by-point basis while the surface is in equilibrium with cesium vapor, and is capable of performing these measurements over a considerable span of surface temperature.

The first device is based on photoelectric emission and consists of a mechanism which scans a light beam over the emitter surface in TV fashion. The photoelectrons emitted from the surface by this light are then collected, and the resulting current is related to the work function of the surface. Several emitter surfaces have been examined in two versions of this device, and the method has proved to be useful in determining work function distributions. It is limited, however, to relatively low surface temperatures — temperatures at which the thermionic emission is low and does not mask the photoelectric emission. It is particularly useful for studying the history of a given surface as its temperature is raised from room temperature to thermionic emitter temperature. Relative work function measurements can readily be performed by this method, but absolute work function values are quite difficult to obtain without the use of monochromatic light. The scope and time of this program did not allow the development of such a light source.

The second device developed under this program employs thermionic emission which is then collimated and scanned over an aperture. This, again,

produces a TV type of work function picture. This method proved very satisfactory for absolute measurement of work function. Single-crystal and polycrystalline emitters were examined in this device, and the results were correlated with converter test data.

A second phase of this program consisted of the preparation of emitter surfaces by several techniques, all of which were aimed primarily at generating a surface which is highly stable at emitter temperatures. The most significant conclusion of this phase of the work is the fact that, from the standpoint of emission capability, the preparation of a given surface can be far more important than the material itself or the bulk orientation underlying the surface. This was shown by the fact that the performance of the specially prepared polycrystalline tungsten emitter in a converter, as well as in work function measurements in the thermionic scanner, was practically identical to the performance of the single-crystal  $\langle 110 \rangle$  emitter to which it was compared, and that these results were superior to those obtained using polycrystalline tungsten emitters in earlier programs.

The third phase of the program consisted of experiments performed in converters, and this work furnished the ultimate confirmation of the results obtained by scanning comparisons of specimens with different metallurgical preparation. Two converters were used primarily for performance testing. One of these employed a polycrystalline tungsten emitter which had been stabilized thermally, and the other used a single-crystal  $\langle 110 \rangle$  tungsten emitter also thermally stabilized. The performance of both these emitters was quite similar, and subsequent emitter work function measurements showed that the average work function of these two surfaces was very similar. This performance level was substantially higher than the performance level of a polycrystalline emitter

tested under another program which had not been subjected to this thermal stabilization technique. The results of the program can be summarized in the form shown in Figure II-1, which is a plot of work function versus the ratio of emitter surface temperature to cesium reservoir temperature. The solid lines shown are theoretical lines for the bare work function values indicated. The converter experimental results are designated by open circles for the  $\langle 110 \rangle$  emitter and by open triangles for the polycrystalline emitter, and these points are seen to correlate very well with the 4.62 value of bare work function. There is some degree of deviation at the high end of the plot, probably due to experimental error. The values of work function observed in the scanners for the  $\langle 110 \rangle$  plane are also correlated with this same bare work function line.

In addition, two sets of points showing the results of work function measurements on the  $\langle 111 \rangle$  surface are also shown. The solid triangles give the work function of points from the general background of this surface, and they correspond to the lowest bare work function values observed during the program. The solid squares give the work function of bright spots (high emission) on the same  $\langle 111 \rangle$  surface, and they correlate along the same line as the  $\langle 110 \rangle$  surface. Thus, the span of work function values actually measured extends from about 4.2 up to 4.62 in bare work function values, which is in good agreement with the previous measurements on the various faces of single-crystal tungsten.

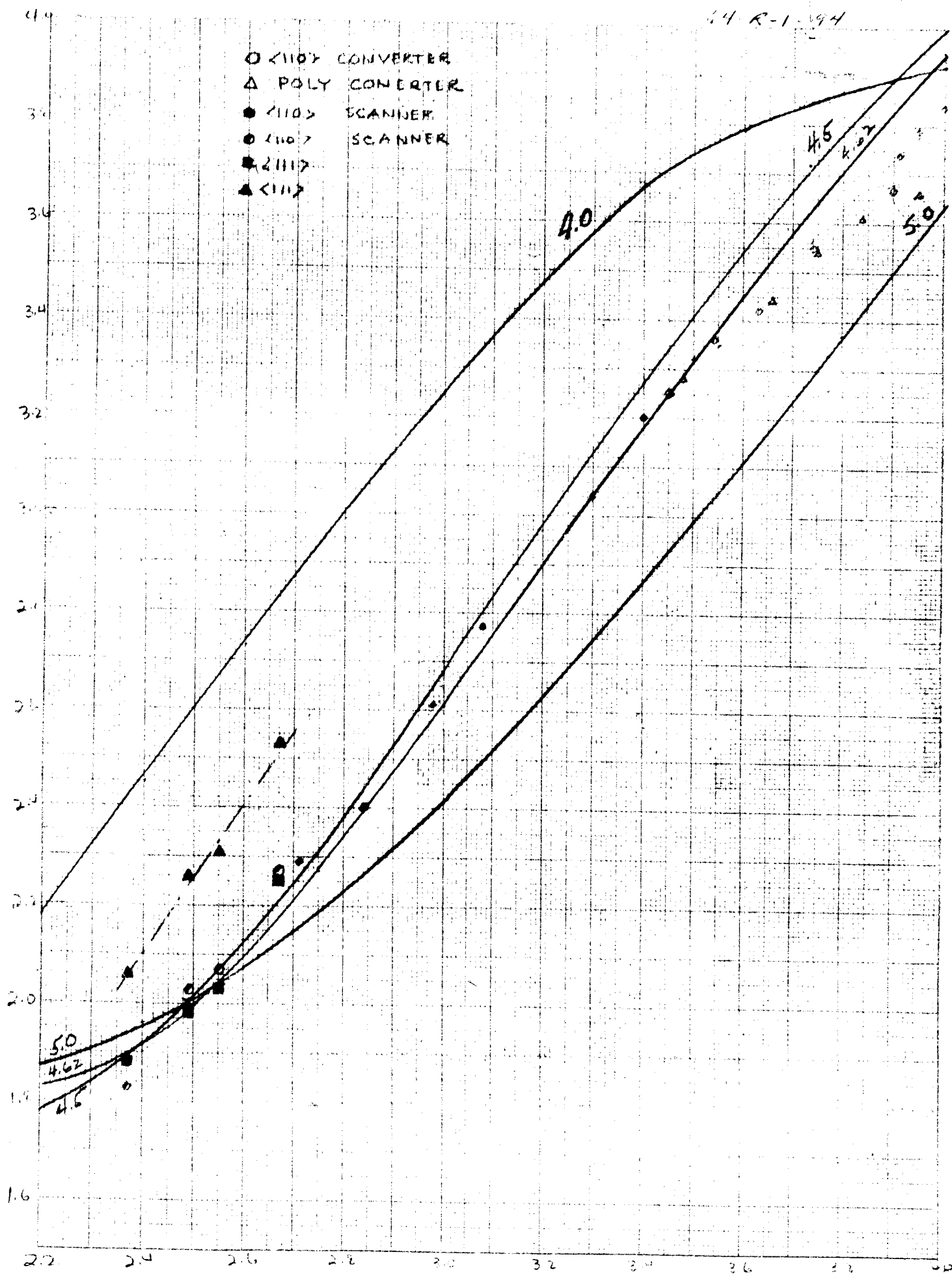


FIG II 1. SUMMARY OF WORK FUNCTIONS MEASUREMENTS



## CHAPTER III

### PHOTOELECTRIC SCANNER

#### A. PRINCIPLE OF OPERATION

The photoelectric scanning device is an instrument which can be used to make detailed work function maps of a metal surface in equilibrium with cesium vapor. It can be used over a range of surface temperatures. The device maps the work function of a surface by scanning it with a light spot and measuring the resulting photocurrent. The light spot contains a wide range of frequencies, varying from the infrared to the ultraviolet. Appreciable photocurrent is obtained from a surface having a work function  $\phi$  only when the frequency of the incident light exceeds the threshold frequency

$$\nu_t = \frac{e\phi}{h} \quad (1)$$

where  $e$  is the electronic charge and  $h$  is Planck's constant. Therefore, when the light spot is swept over a surface, the resulting photocurrent is modulated by the variations in work function on the surface.

In the present device, the position of the light spot is synchronized with that of an oscilloscope beam spot whose intensity is modulated by the photocurrent. The pattern resulting on the oscilloscope, as the light spot scans the emitter surface, corresponds to a "picture" of the emitter surface, with bright spots corresponding to low work function and dark spots to high work function areas. The instrument is also capable of measuring the surface work function directly by fixing the light spot on a selected portion of the emitter and measuring the work function by standard photoelectric techniques.





The photoelectric scanning device consists of the following four subsystems:

1. Optical system
2. Electronic scanning system
3. Photocurrent detection and amplification system
4. Test cell and emitter assembly.

A block diagram of the entire device is shown in Figures III-1a and III-1b.

## B. OPTICAL SYSTEM

The optical system consists of the following components shown in Figure III-1a:

Arc source  
Chopper  
Variable aperture  
Focusing lens  
Deflecting mirrors.

These components were designed for flexibility to afford a field of investigation as unrestricted as possible. Certain compromises were nevertheless unavoidable, the basic compromise being the choice of a mirror deflection system limited in frequency to a few hundred cycles per second. One alternative to this choice would be a moving spot source such as a projection kinescope. Although several advantages in instrumentation would be gained by the use of a kinescope, such a source would have an intensity  $10^4$  less than high-pressure gas arcs. This limitation of the kinescope source was judged as too severe because of the consequent reduction of photocurrent.

The particular advantage of a mirror deflection system is the wide variety of light sources which can be used, with mercury, xenon, carbon, and zirconium



arc lamps being readily available. These lamps provide a wide range of spectra which vary from the ultraviolet to the infrared. For light of all these wavelengths to pass through the optical system efficiently, all mirrors were coated with magnesium fluoride films which have good reflectivity well into the ultraviolet region. Sapphire lenses were used in the system because they have good transmissivity over the entire range of arc radiation. The spectra of mercury, xenon and zirconium as functions of wavelength are shown in Figures III-2, III-3, and III-4, respectively. Figure III-5 relates wavelength to photon energy in electron volts. This figure illustrates the range of surface work function which each arc can investigate.

A lamp power supply has been constructed which is capable of running either the PEK-109 mercury arc or the PEKX-75 xenon arc. It was designed to have an extremely low ripple voltage in order to avoid minute variations of arc intensity which could appear as noise in the photocurrent. A ripple of less than 0.05% was achieved, which is a sufficiently low level.

The galvanometers and a mechanical light chopper have been mounted on a rigid stand capable of being positioned over any device with a minimum setup. The chopper consists of a gear wheel mounted on a variable-speed motor and arranged to intercept the light beam near the source aperture. The resultant modulation frequency may be made as high as 40 kc and, since the photocurrent will be similarly modulated, the desired currents may be easily separated from any noise. The motor driving this chopper is not a synchronous motor at the present time, and therefore it has a tendency to drift in frequency to some extent. The scanner cell is contained completely inside the vacuum chamber. This precaution was taken in order to avoid oxidizing the ceramic-to-metal seal at the sapphire window. This arrangement required that an additional window in the vacuum chamber be placed in front of the emitter.



### C. ELECTRONIC SCANNING SYSTEM

The electronic scanning system is made up of the following components shown in Figure III-1b:

X-scan generator

Y-scan generator

X galvanometer

Y galvanometer

Galvanometer driver amplifiers and zero-control circuits.

The x-scan is obtained from an audio-signal generator, while the y-scan is conveniently obtained from the oscilloscope saw-tooth also used to display the surface map. Two Sanborn Co. galvanometers No. 618X and No. 618Y are used for deflecting two plane mirrors which cause the light beam to scan the emitter surface. These galvanometers are powered by two Sanborn No. 670-200B driver amplifiers and a No. 670-300 driver power supply. The amplifiers and power supply are mounted on the galvanometer control board which also includes zero-control circuits for the galvanometers, and attenuators for the galvanometer driving signals.

### D. PHOTOCURRENT DETECTION AND AMPLIFICATION SYSTEM

The proper design of the photocurrent detection circuit depends strongly on the magnitude of both the photocurrent and the thermionic current passing from emitter to collector. A short calculation will serve to estimate the magnitude of the photocurrent.

It is desired to scan the emitter surface with a light spot, approximately 1 mil (0.001 inch) in diameter. The present optical system using 1-inch lenses and mirrors is capable of focusing a light source 3 mils in diameter down to a



1-mil light spot on the emitter. In order to maximize the amount of light focused into the 1-mil spot, it is required that the first 1-inch lens be placed 9 inches from the light source, thus defining the solid angle of the light source focused on the emitter. The energy of light which is focused on the emitter is given by

$$P = I \Omega T \frac{\pi d^2}{4} \quad (2)$$

where  $I$  is the light source intensity,  $\Omega$  is the solid angle of the source which the optical system receives,  $d$  is the diameter of the portion of the light source focused on the emitter, and  $T$  is the transmissivity of the optical system.

For the present system

$$d = 0.003 \times 2.54 = 7.60 \times 10^{-3} \text{ cm.}$$

The solid angle can be found by

$$\Omega = \frac{\pi r^2}{4 \pi R^2} \quad (3)$$

where  $r$  is the radius of the first lens and  $R$  is the distance of the light source from the first lens. It is estimated that

$$T \approx 0.80.$$

The intensity of the PEK-109 high-pressure mercury lamp is

$$\begin{aligned} I &= 1.4 \times 10^5 \text{ candles/cm}^2 \\ &= 2.33 \times 10^5 \text{ watts/cm}^2. \end{aligned}$$

Substituting the above values in Eq. (2), one finds

$$P = 6.56 \times 10^{-3} \text{ watts.}$$

To determine the photocurrent, it is necessary to know the photoelectric yield of the emitter surface. This quantity is defined as the photocurrent in microamperes per microwatt of light intensity. The system was tested with a 926 phototube which has a photoelectric yield of

$$Y = 0.0018 \frac{\mu \text{ amp}}{\mu \text{ watt}} .$$

In the 926 phototube, the optical system should produce a photocurrent of the magnitude

$$\begin{aligned} i &= Y P & (4) \\ &= 0.0018 \times 6.56 \times 10^{-3} \\ &= 11.8 \times 10^{-6} \text{ amp.} \end{aligned}$$

This is indeed the approximate current experimentally obtained from the phototube when it is scanned by the optical system.

Preliminary experiments have shown that the yield of a tungsten surface covered with cesium is about 100 times less than the 926 phototube, or

$$Y_{\text{Cs-W}} = 10^{-5} \frac{\mu \text{ amp}}{\mu \text{ watt}} .$$

The above yield for a cesium-tungsten surface implies a photocurrent of

$$\begin{aligned} i &= 6.56 \times 10^{-3} \times 10^{-5} \\ &\approx 10^{-7} \text{ amp.} \end{aligned}$$

The photocurrent detection circuit must therefore be capable of measuring from  $10^{-6}$  to  $10^{-9}$  amperes. If the photocurrent is measured across 1 megohm, the detection circuit must be sensitive to voltages of the order of 1 millivolt. It



is necessary, however, to amplify this signal to a level of 10 volts in order to modulate the oscilloscope beam intensity. The detection circuit, therefore, must have a gain of at least  $10^4$ .

The display system consists of a modified Hewlett Packard 130 CR oscilloscope with an additional battery-powered ac amplifier, Tektronix Type 123, a variable-bandwidth filter, and an input transformer. The arrangement of the equipment is shown in Figure III-1b. The use of an interrupted photocurrent eliminates problems of amplifier dc drift and voltage matching in coupling. The bandwidth-limiting filter rejects most of the noise which may be white noise in the thermionic current or hum present in the laboratory. A compromise must be made in the amount of detail that has to be retained in the signal versus the amount of noise that is to be rejected. This compromise determines the choice of the bandwidth of this filter. The oscilloscope has been modified to allow separate use of the vertical amplifier as a z-axis amplifier. The y-axis scanning oscillator is, therefore, coupled directly to the vertical plates through a phase shifter which compensates for phase shift in the galvanometer. Horizontal deflection is obtained from the time base with an additional sawtooth output for the x scanning. The z-axis signal may be observed by switching the horizontal amplifier from the time base to the vertical amplifier, vertical deflection being provided by the scanning oscillator directly. The z-axis system has sufficient gain to completely modulate the intensity with the input amplifier noise and, therefore, it is this noise which limits the maximum usable sensitivity to 10 microvolts. The corresponding minimum detectable photocurrent depends upon the dynamic impedance of the cell, but is ultimately limited by the resistance across the leadthrough (typically less than 100,000 ohms). The minimum detectable photocurrent is thus about  $10^{-10}$  amps. Saturation of the present input transformer limits the thermionic current output to about 1 milliamp.



With a larger transformer, the thermionic shot noise will limit thermionic currents to about 100 milliamps.

The circuit in Figure III-6a is only useful when the tube has a reasonably high dynamic impedance. This can be shown by an analysis of the equivalent circuit. Consider Figure III-6b. In this circuit,  $i_p$  represents the photocurrent and  $R_1$  represents the tube dynamic impedance. The load resistance and collecting potential resistance can be neglected since the thermionic current is considered to be large compared to the photocurrent. The resistance  $R_3$  is the input impedance of a pre-amplifier, so that the voltage across  $R_3$  is the quantity to be determined.

The following equations can then be written:

$$i_p = i_1 + i_2 \quad (5)$$

$$i_1 R_1 = i_2 \omega L_2 + \frac{1}{\alpha} i_3 \omega L_3 \quad (6)$$

and

$$i_3 R_3 = i_3 \omega L_3 + \alpha i_2 \omega L_2 \quad (7)$$

where  $\omega$  is the light modulation frequency, and  $\alpha$  is the voltage transfer ratio of the transformer  $L_3, L_2$ .

Solving these equations for  $i_3$ , one can then calculate  $V_3$  as

$$V_3 = i_3 R_3 = \frac{i_p \omega L_3}{\left[ 1 - \omega \left( \frac{L_3}{R_3} - \frac{L_2}{R_1} \right) \right]} \quad (8)$$

To maximize  $V_3$ , the quantity in parentheses is set equal to zero,

$$L_3/R_3 - L_2/R_1 = 0 \quad (9)$$

or

$$L_3/L_2 = R_3/R_1 \quad (10)$$



In addition  $L_3/R_3$  and  $L_2/R_1$  must be small so that the response time of the circuit is short.

Desirable parameters for the circuit would be

$$\omega = 10^5 \text{ radians/sec}$$

$$L_3/R_3 \leq 10^{-6}$$

and

$$\omega L_3 = 10^6.$$

Then

$$L_3 = 10 \text{ henries}$$

and

$$R_3 \geq 10^7 \text{ ohms.}$$

Practicable transformers have a maximum voltage transfer ratio of 1000. Therefore, this ratio and Eq. 10 fix  $L_2$  and  $R_1$  as

$$L_2 = 10^{-2} \text{ henries}$$

and

$$R_1 \geq 10^4 \text{ ohms.}$$

This circuit would be capable of measuring a photocurrent  $10^{-11}$  amperes when used in conjunction with the amplifiers.

The lower limits, set by the tube dynamic resistance, point out that difficulties in detecting the photocurrent become increasingly important as the region of practical converter operation is approached. In this region, converter dynamic resistance can be less than 1 ohm, which is several orders of magnitude below the limit set on  $R_3$ . This means that the sensitivity of the circuit is several orders of magnitude less than the  $10^{-11}$  amperes calculated above.





## E. DESCRIPTION OF PHOTOELECTRIC SCANNER CELL

### 1. Preliminary Model

As shown in Figure III-7, parts numbered 1 through 4 make up the standard emitter assembly which can be fitted to both the thermionic scanner and the converter. The emitter assembly is attached to the tube by means of a flange using a copper gasket. Part 9 is the collector, and part 15 is the sapphire window through which the emitter is scanned. The leadthrough (12, 13, 21 and 22) is heliarc-welded onto part 11. Should the leadthrough fail in any manner, it may easily be replaced by grinding off the weld and rewelding a new leadthrough to the unit. Deterioration of the leadthrough electrical resistance is expected to necessitate frequent replacement of this part. The sapphire window is also welded to the unit so that it can also be replaced. Part 10 is a copper ring on which a heating coil is mounted for heating the casing to a temperature above that of the cesium reservoir. The cesium reservoir is attached to a nickel tube brazed to the side of the casing. The model is designed to be set on top of an open-end pyrex bell jar so that the emitter section and bottom portion of the tube can operate in vacuum. The upper flange and sapphire window are heated by a hot inert gas.

### 2. Advanced Model

In testing the preliminary model of the photoelectric scanner several improvements were found to be necessary. It was found that the demountable copper gasket did not function reliably; in the advanced model the emitter was replaced using a demountable weld of the emitter section. Also it was found to be impractical to operate the scanner with part of the casing expanding from the vacuum bell jar, due to difficulty of controlling the casing temperature. An additional sapphire window was required to allow the entire unit to operate in



vacuum. In addition, the entire tube was reduced in size, increasing all-around operating convenience. This model is shown in Figure III-8. The emitter (1) is attached to the emitter sleeve and thermal barrier (2), and to the supporting structure (3). Heat is rejected by a molybdenum radiator (4). A supporting structure (5) is equipped with a demountable weld flange. A titanium getter (6) is provided.

The photoelectrons are collected on the collector (20), which is attached to a demountable leadthrough (21). This leadthrough may be replaced using the demountable flanges if the leadthrough resistance becomes too high for measurement. The light beam enters through the sapphire window (22), also welded to the casing (23) by means of a demountable flange. The cesium is introduced via the tubulation (24). This same tubulation is used for the initial pumpdown and outgassing of the tube. A groove is provided on the casing for mounting a heater to control the casing temperature. The entire unit is mounted on a variable-temperature heat sink, and is supported in an evacuated bell jar fitted with a sapphire window. This is shown in Figure III-9. The mirror drive mechanism is positioned above the sapphire window.

## F. RESULTS FROM PHOTOELECTRIC SCANNER

### 1. Preliminary Experiments

A convenient way for setting up and calibrating this scanning device has proved to be the use of a commercial phototube. Figure III-10 is a map of the phototube surface. The dark diagonal line is the shadow of the anode wire in the phototube. The size of this wire provides a measure of the detail that can be resolved with the device. The diameter of this wire is about 0.040 inch, and the smallest spots discernible in this map are observed to be roughly 0.002 inch. It



is interesting to note that essentially no gray spots appear in this map, indicating that this surface is relatively uniform except for non-emitting black spots. Figure III-11a is a display of the photocurrent along one scanning line in the Y direction of Figure III-10. The large dip near the top of this picture is the shadow of the collecting wire in the phototube. This type of display can be used in quantitative measurements of work function, since the actual magnitude of current is indicated here rather than relative brightness. The simplest method of obtaining quantitative data can be described in terms of the right-hand side of the pattern shown in Figure III-11b. Here the dc level has been adjusted so that all portions of the surface having photoemission less than a certain value will show as black areas on the map. Now, if several photographs are obtained with the dc level at successively increasing values, the areas with work functions between prescribed values will show up as new black areas in the successive maps obtained.

The first emitter to be tested in the photoelectric scanner was a polycrystalline tantalum emitter. Photographs of emission scans of this emitter are shown in Figures III-12a, b. Areas of varying emission are seen in this photograph. By adjusting the intensity of the display to the sensitivity of the film, a greater range of values of gray can be read from the photograph. Figures III-13a, b, c are maps obtained with a polycrystalline tungsten emitter in equilibrium with cesium vapor. In Figure III-13a cesium and emitter temperatures of  $300^{\circ}\text{K}$  are employed. Figure III-13b shows the same area with the same cesium pressure but with an emitter temperature of approximately  $600^{\circ}\text{K}$ . In Figure III-13c the emitter temperature has been raised to  $800^{\circ}\text{K}$ . Note that the best detail and resolution are obtained with the intermediate conditions. The higher-temperature picture is at approximately the limit of the present system which is controlled by the relationship between thermionic current and photocurrent.



## 2. Experimental Results

After the preparation described in Chapter 4 of the Third Quarterly Report and after metallurgical examination, the composite emitter was introduced in the photoelectric scanner. In the scanner it was outgassed at 1600°C for 12 hours. This temperature is well in excess of the operating temperature of the scanner. A typical series of photographs of the emitter surface is shown in Figure III-14. These photographs have been obtained directly from the display on the oscilloscope screen. The cesium reservoir temperature has been held constant at 300° K, and the surface temperature has been varied from 360° K to 660° K. Note that the display is a mirror image of the photograph shown in Figure III-15. The herringbone pattern in these photographs results from the use of a chopper and does not appear when viewed directly using a long-persistence phosphor in the display tube. The diminished intensity toward the edges of the emitter is caused by the effect of stray magnetic fields from the galvanometer magnets. The differences in photoelectric current resulting in dark and bright areas on these photographs are about 15% of the average photocurrent value, corresponding to a work function variation of about 0.2 volt. This is quantitatively consistent with both previous experimental and theoretical results for surfaces with bare work functions between about 4.2 and 5.2 electron volts. The results obtained throughout this program have been correlated in terms of the dependence of covered work function on bare work function and  $T/T_R$ . This method has been found to be the most convenient way of correlating work function variations. In terms of this dependence, the changes occurring in the series of photographs shown in Figure III-14 will now be discussed. The quadrants  $\langle 111 \rangle$  and  $\langle 110 \rangle$  reverse their roles as lowest cesiated work function areas as  $T/T_R$  is increased. The photograph taken at  $T/T_R = 1.2$  shows that the  $\langle 111 \rangle$  quadrant is the brightest, while the  $\langle 110 \rangle$  is the darkest area. At



the other extreme of  $T/T_R = 2.2$ , the  $\langle 110 \rangle$  quadrant exhibits the lowest work function while the  $\langle 111 \rangle$  appears to be the darkest. This is consistent with theoretical expectations if the  $\langle 111 \rangle$  quadrant has a bare work function near 4.3 and the  $\langle 110 \rangle$  near 4.6. The niobium braze is the darkest feature at  $T/T_R = 2.2$ , as expected, but it is the brightest at  $T/T_R = 1.2$ , which is counter to expectation. The electropolished region of the  $\langle 100 \rangle$  face is the darkest extended region below  $T/T_R = 2.2$ , suggesting that it has the lowest bare work function, less than 4.3 ev. This behavior of the two areas of the  $\langle 100 \rangle$  face clearly demonstrates the difference in emission that can result from different methods of preparation of the surface. Finally, at  $T/T_R = 2.2$ , the surface appears most uniform. At this region of  $T/T_R$  this is to be expected for surfaces having work functions between 4.2 and 5 ev.

#### G. DISCUSSION

The usefulness of the photoelectric scanner lies mainly in its ability to operate at much lower surface temperatures than can thermionic display devices. This permits observation of changes in the surfaces of emitters or collectors as they are heated from room temperature to thermionic temperatures. The ability of this scanner to observe these changes is particularly useful since the thermionic scanner takes over at the end of the range of the photoelectric scanner and extends the emission display to very high temperatures. The photoelectric device should be especially useful in the study of collector surfaces. Thus it is evident that these two devices complement each other rather than performing duplicate functions. In the region where they overlap, they provide a cross check to increase confidence in the interpretation of results from both devices.

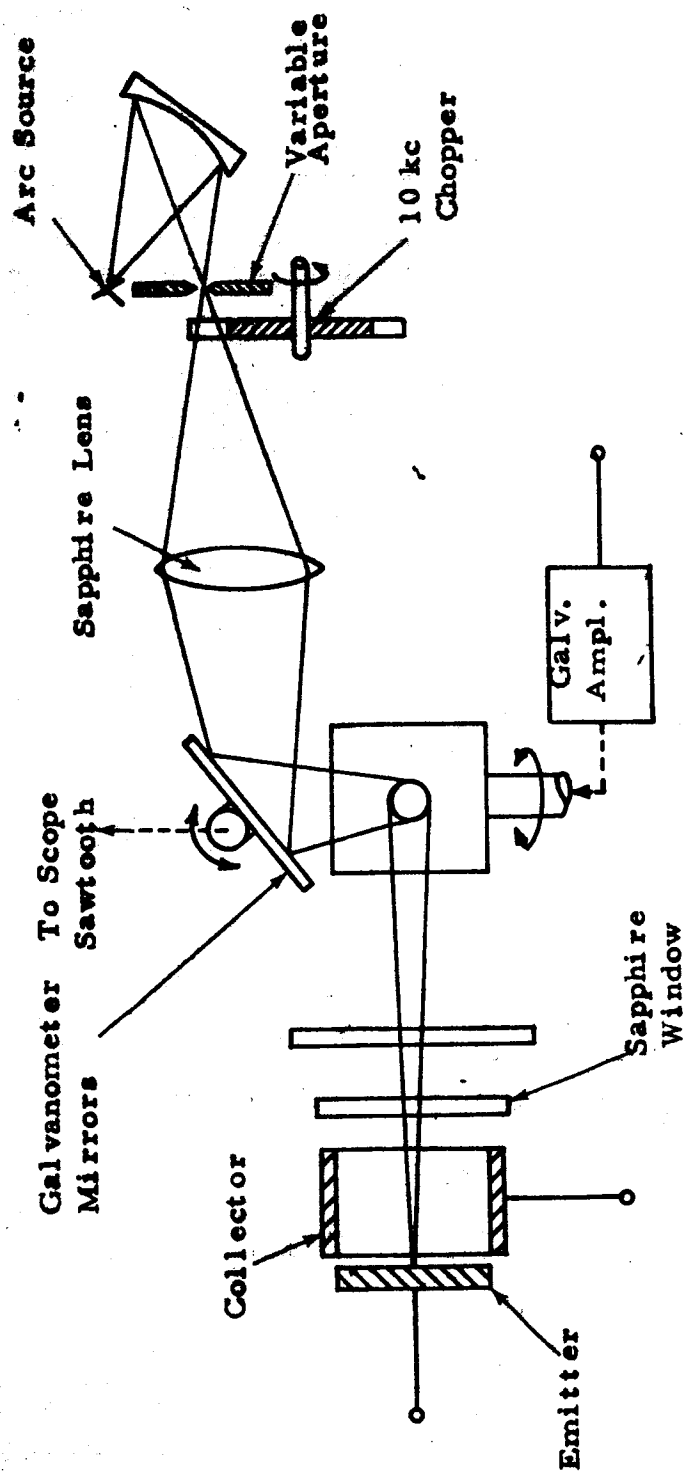


Figure III-la. Block Diagram of Optical System

To Galvanometer Drive

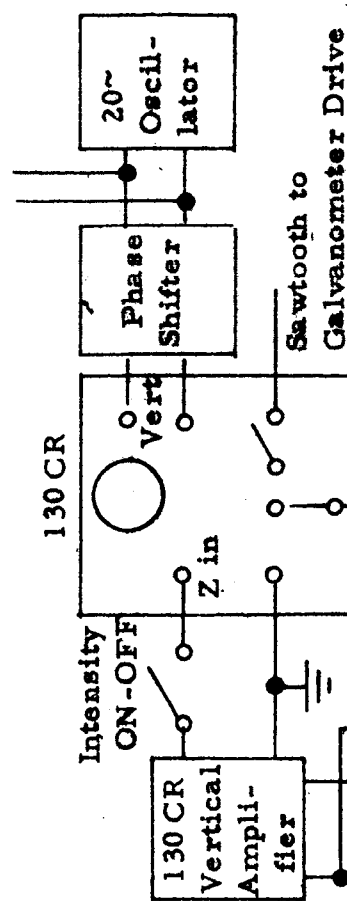


Figure 11-4b. Block Diagram of Display and Amplifier Components

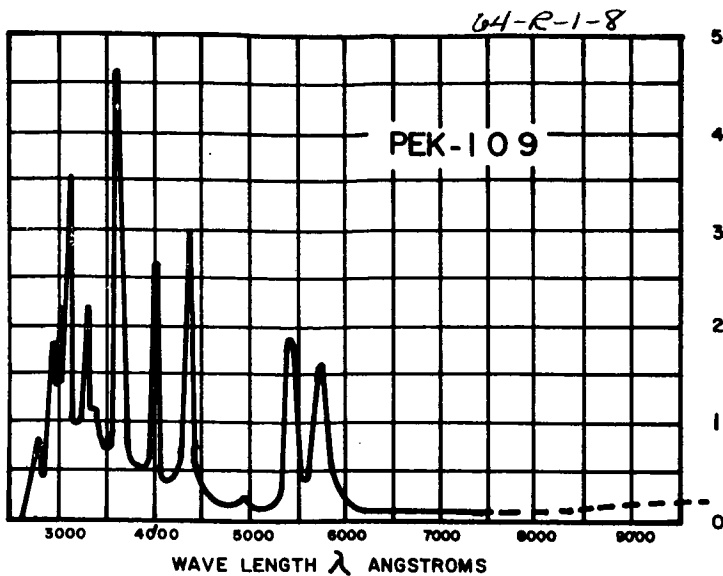


Figure III-2. Spectrum of Mercury  
 PEK-109  
 Arc Size ..... .017 x .017 in.  
 Average  
 Brightness ... 140,000 CD/CMS DIA.

Figure III-3. Spectrum of Zenon  
 PEK X-75  
 Arc Size ..... .015 x .015 in.  
 Average  
 Brightness ... 100,000 CD/CMS DIA.

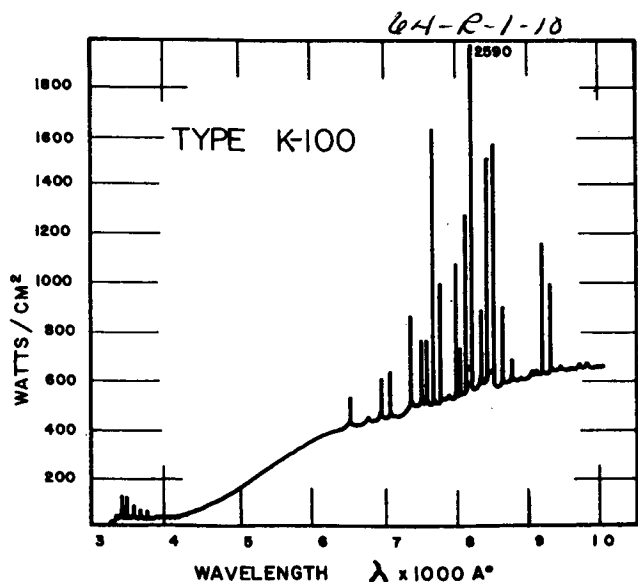
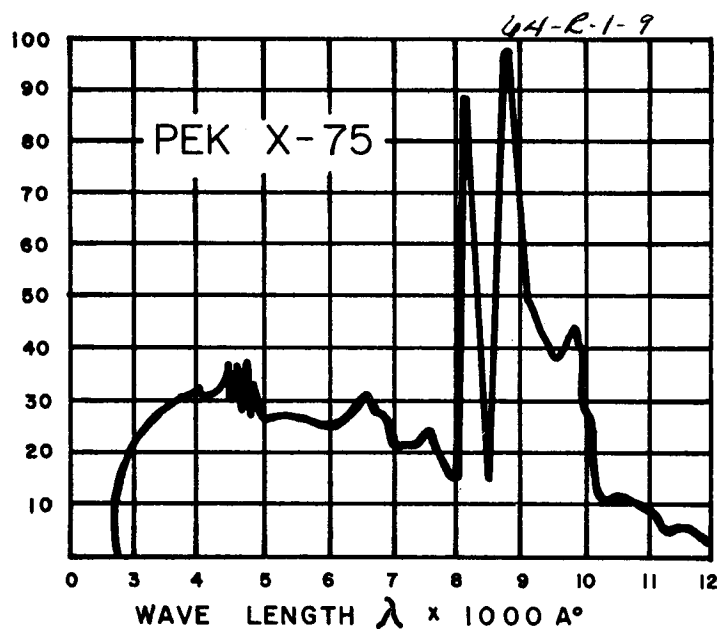


Figure III-4. Spectrum of Zirconium  
 SYLVANIA 100  
 Arc Size ..... .059 in.  
 Average  
 Brightness ... 40,000 CD/CM2 DIA.



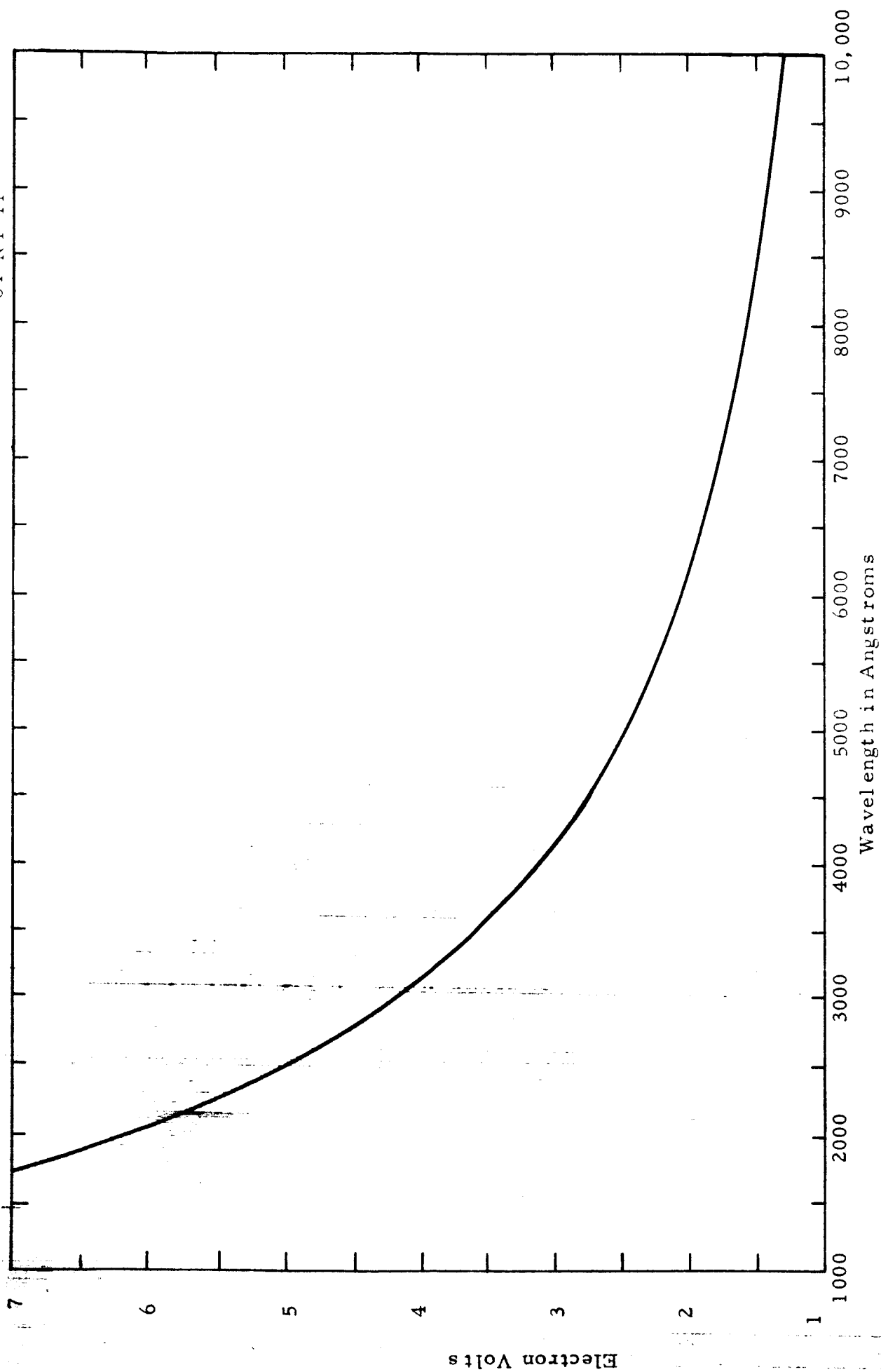


Figure III-5. Wavelength Vs. Photon Energy

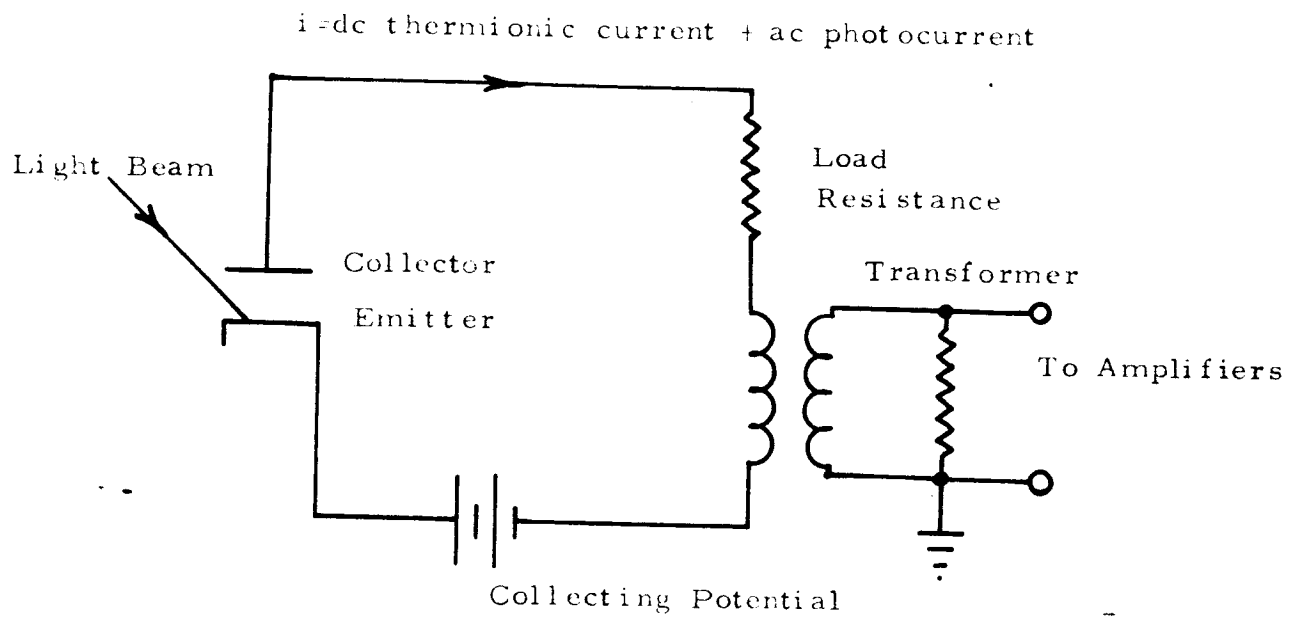


Figure III-6a. Electrical Circuit for Measuring Photocurrent in the Presence of Large Thermionic Currents

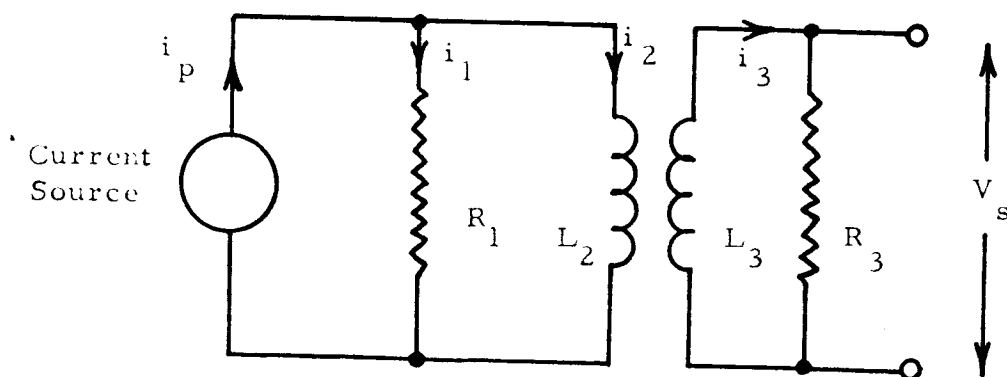
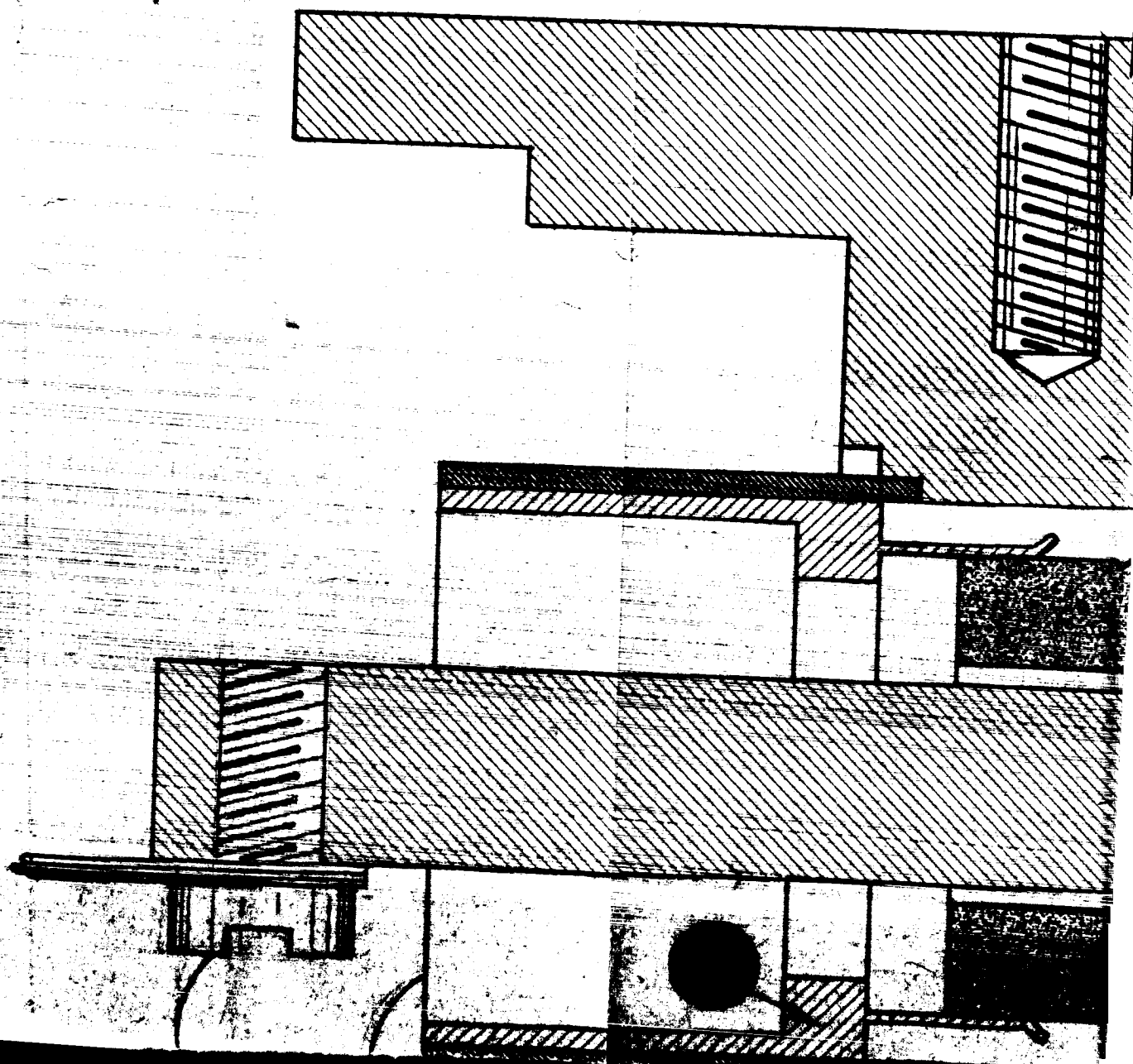
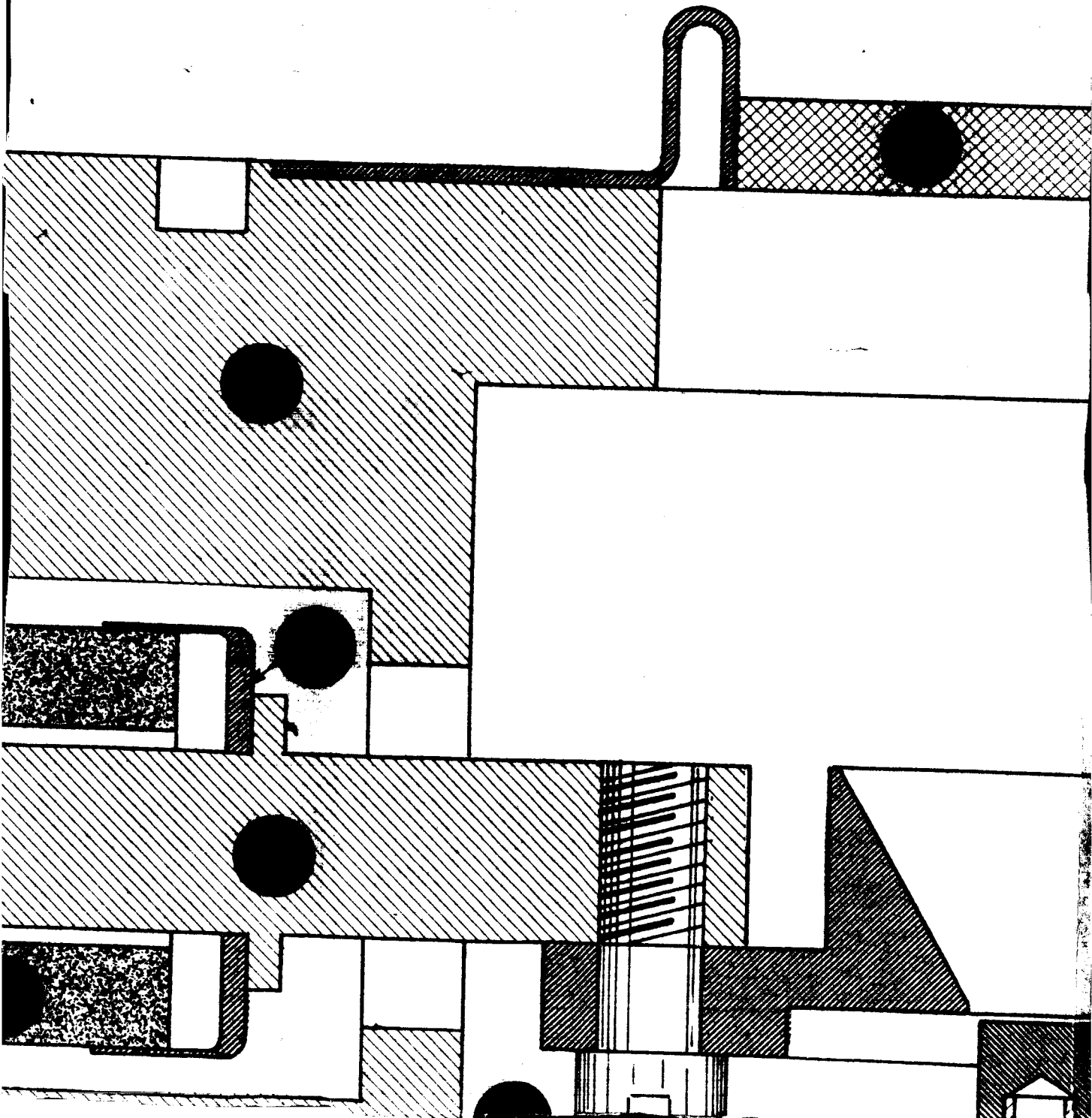


Figure III-6b. Equivalent Dynamic Circuit of Fig. III-6a

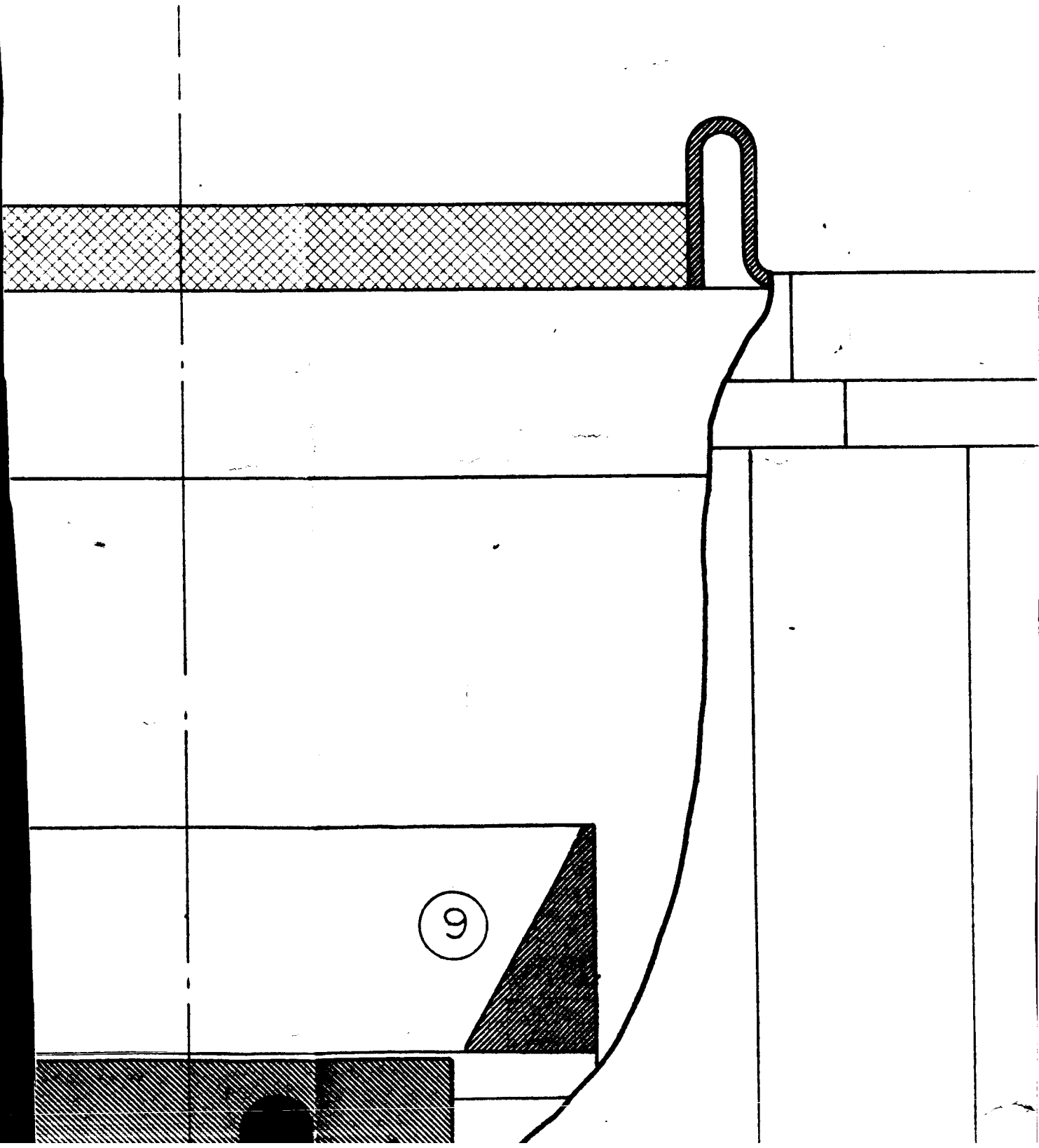
(1)



(2)



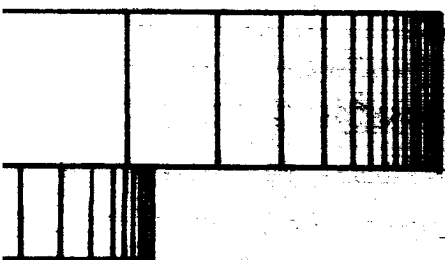
(3)

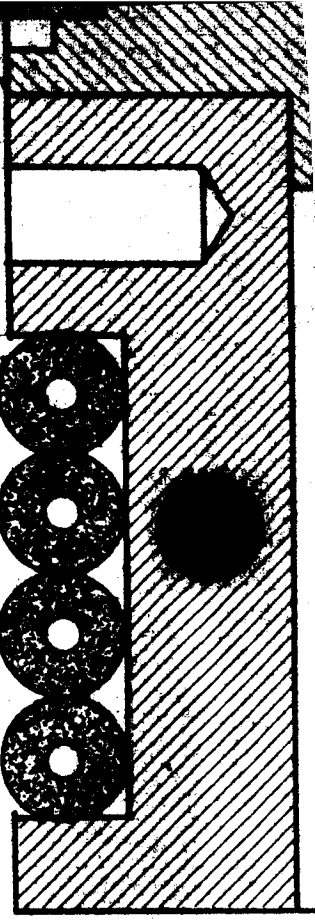


(4)

[illegible]

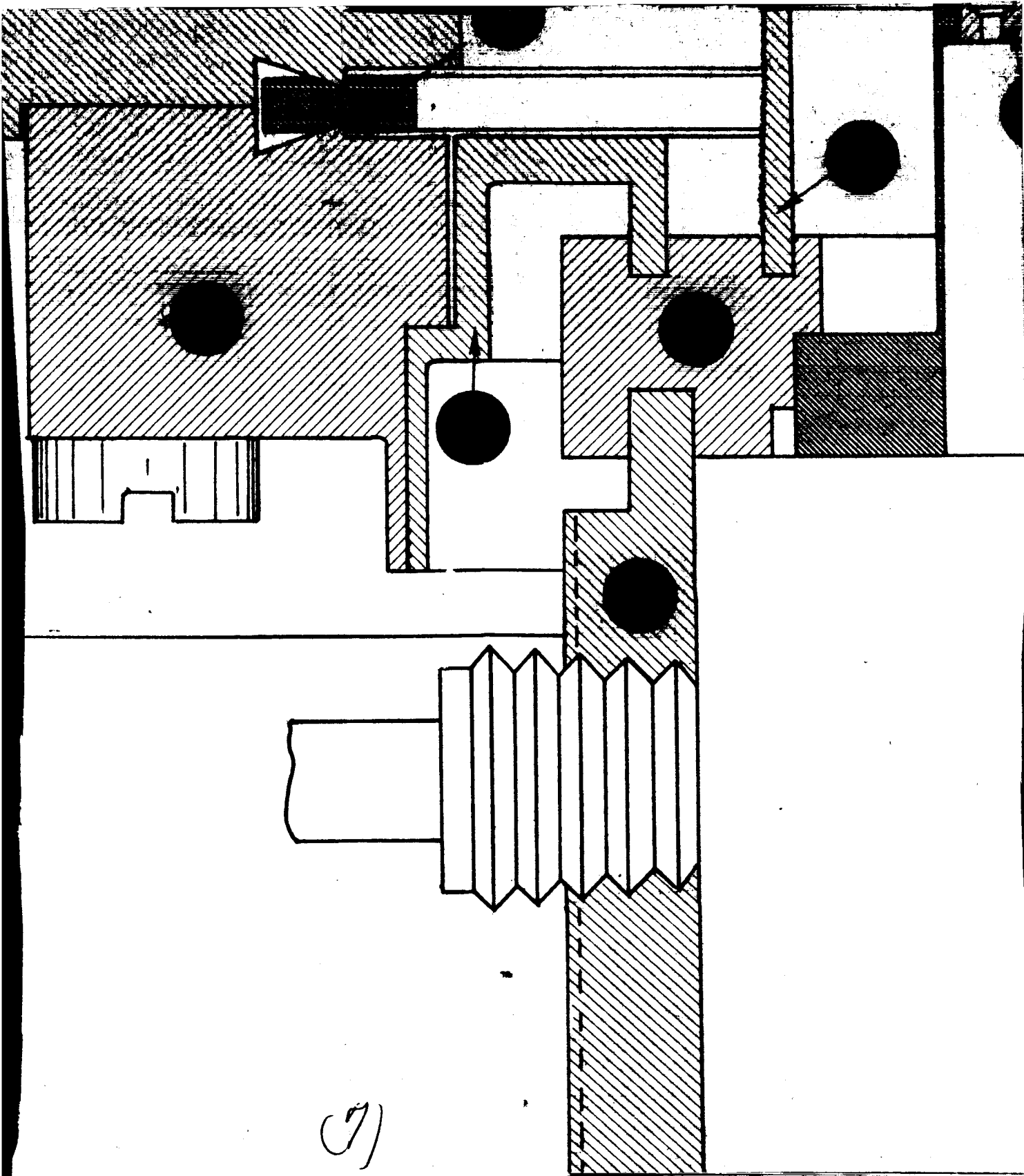
(5)

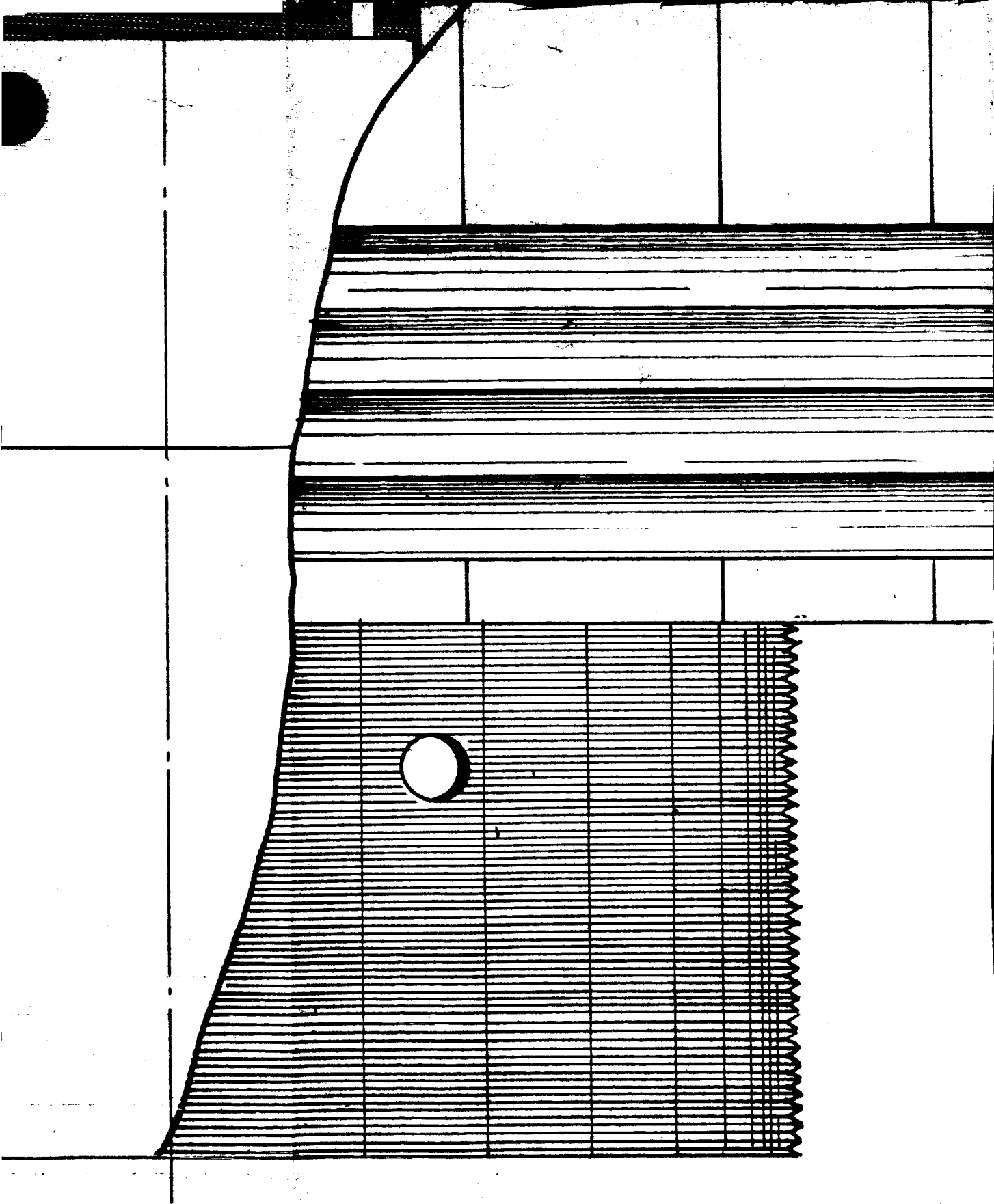




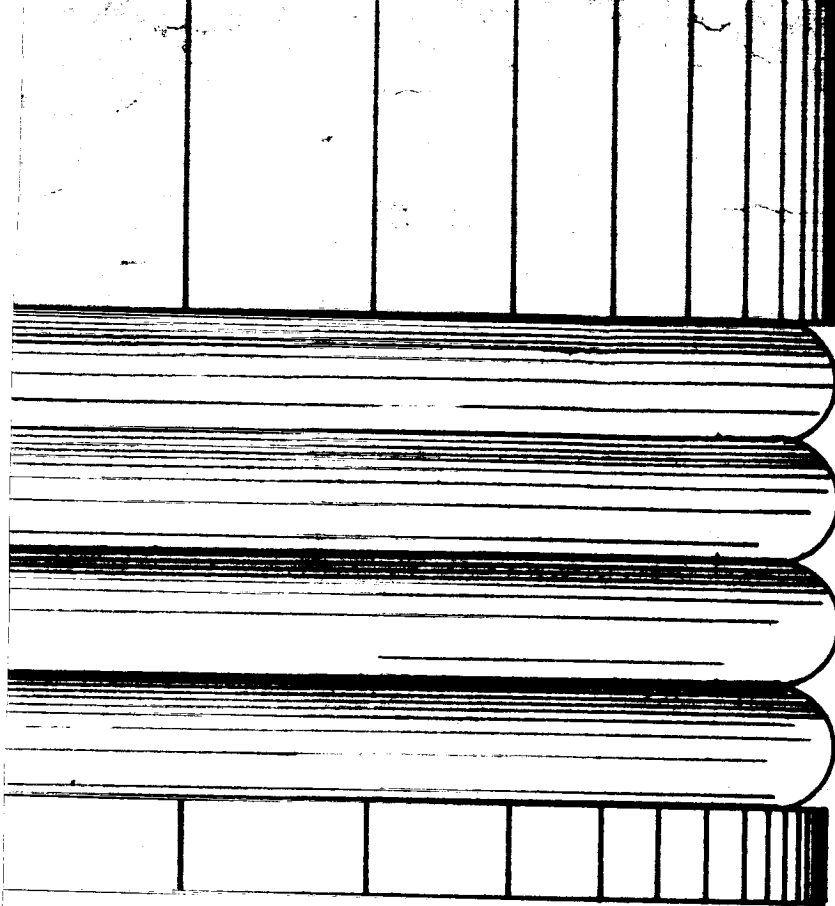
(6)







(8)

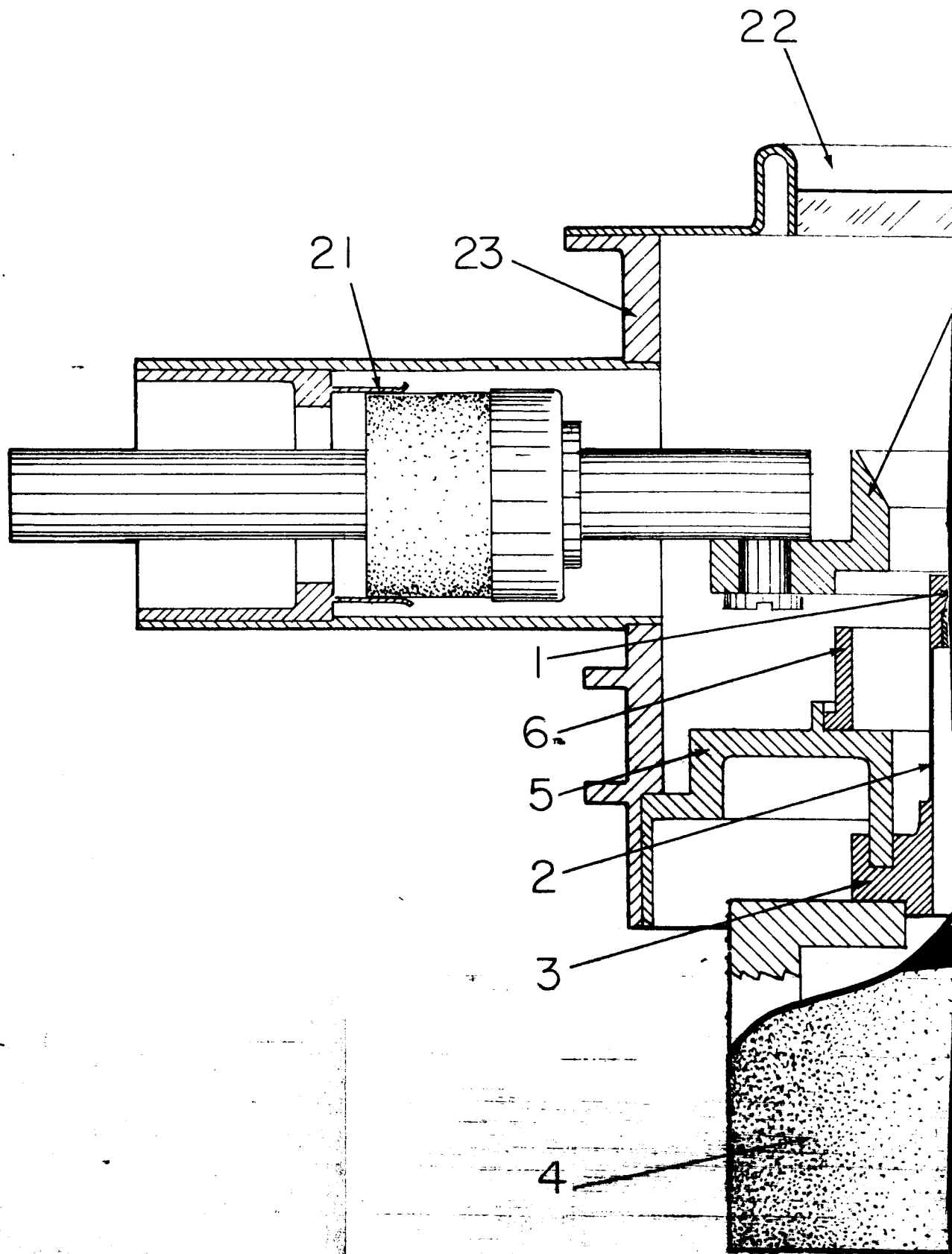


(9)

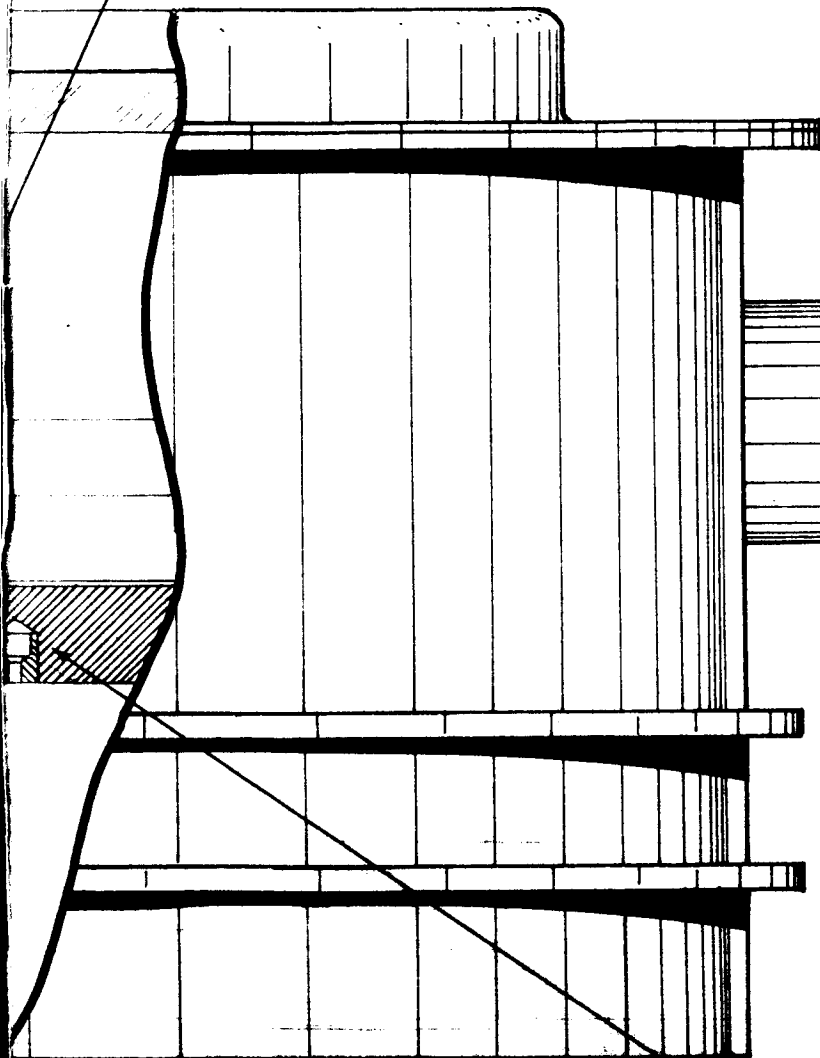
Fig. 1. Assembly of Preliminary  
Model of Photoelectric Apparatus

(1)

Figure III-8 assembly of Advanced model  
of Phosphorus burner



20



24

7

*Can  
50%*

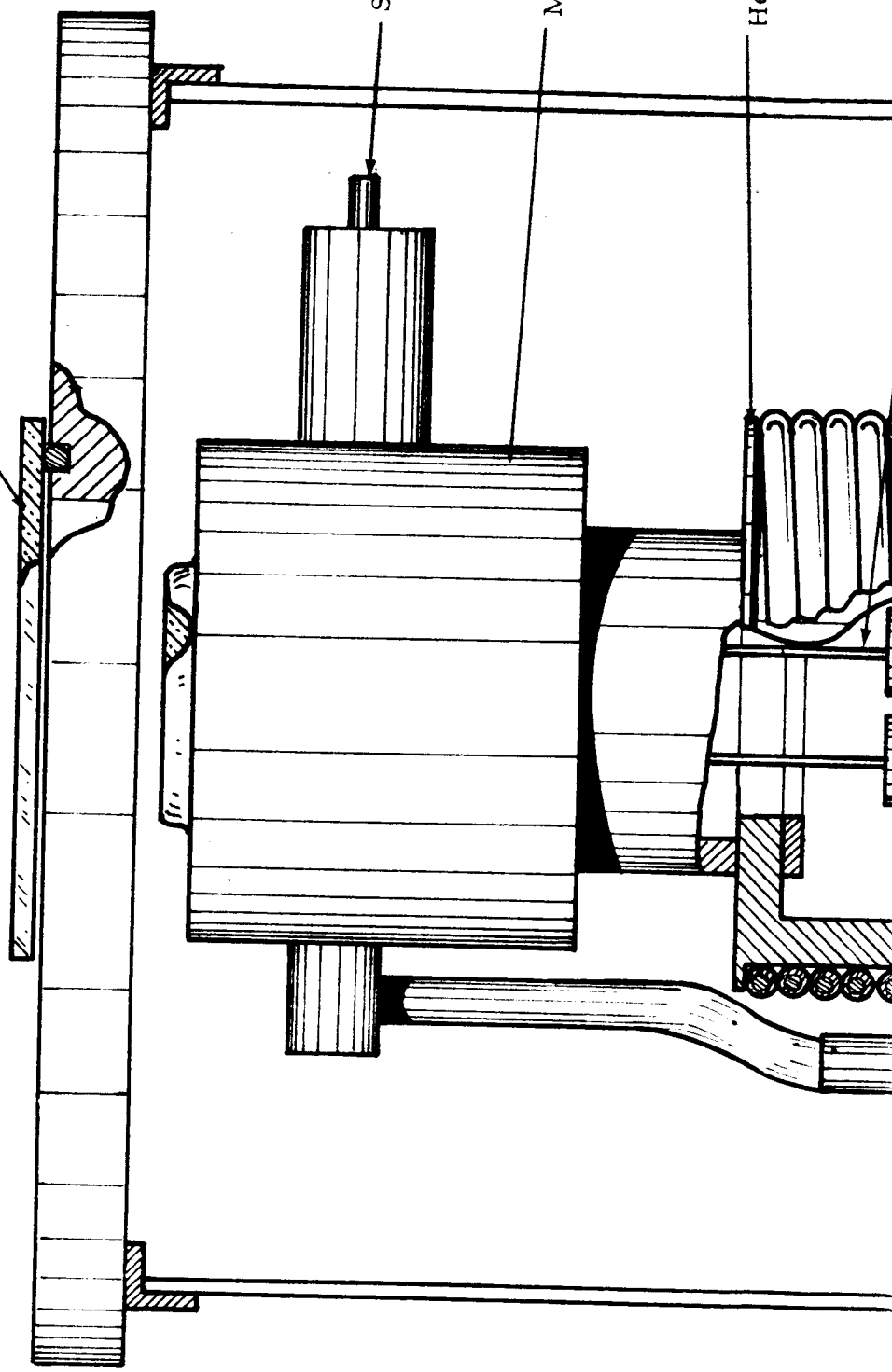
629

Sapphire Window

Signal Leadthrough

Model

Heat Sink



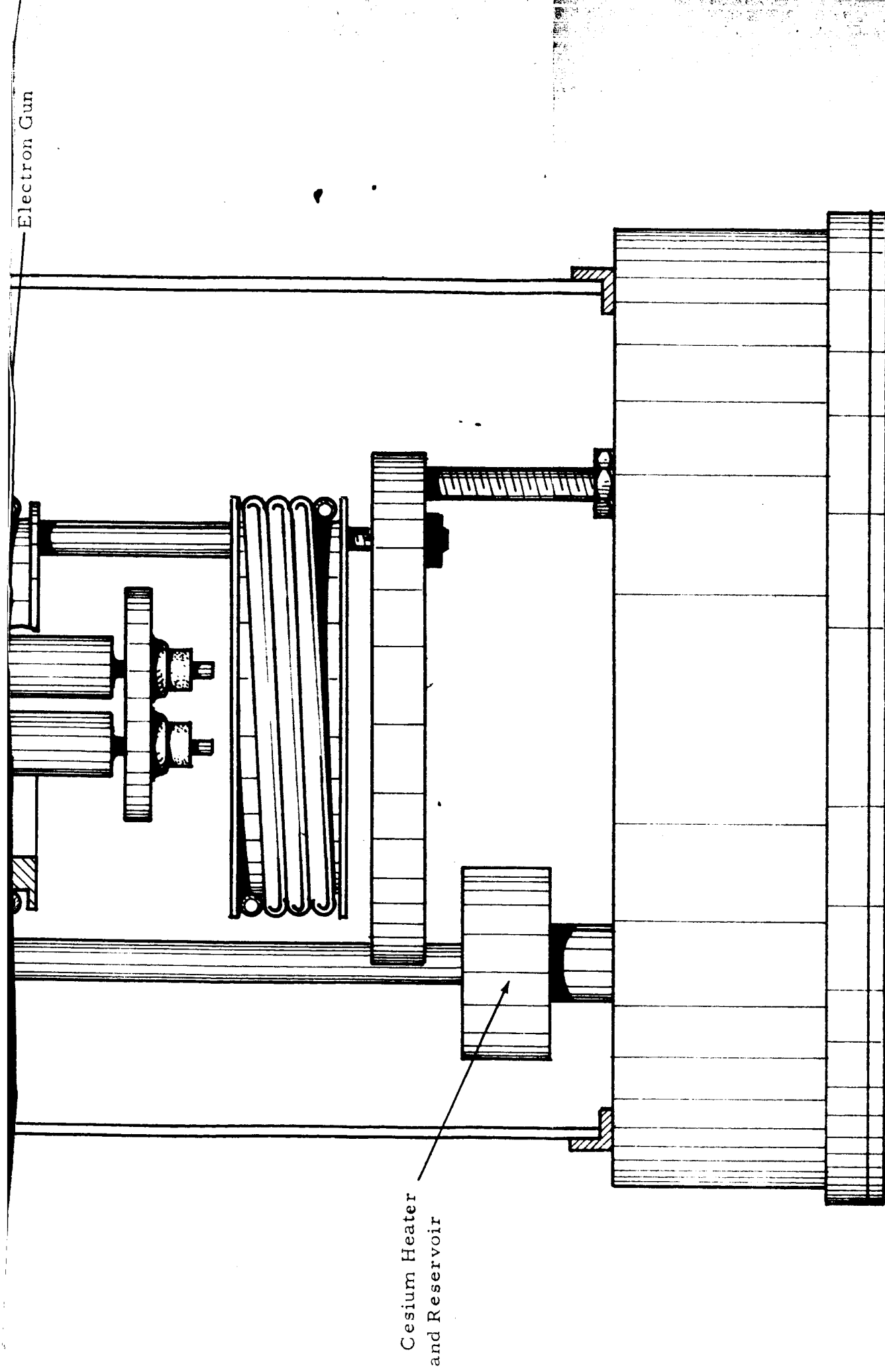


Figure III-9 Advanced Model of Phototube Scanner in  
Test Stand, in Bell Jar



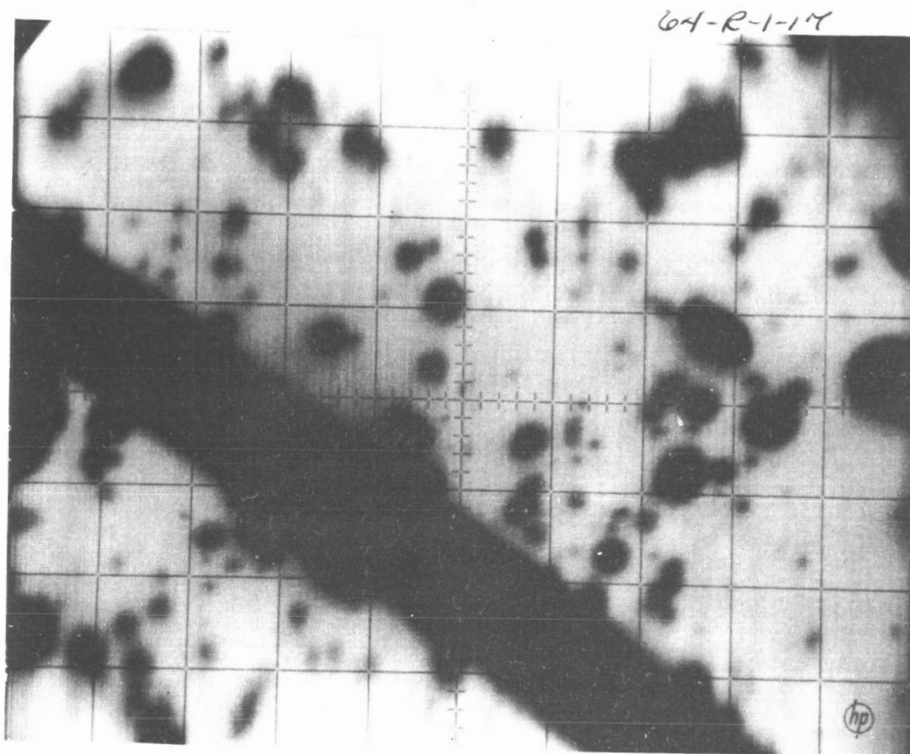


Figure IV-10. Work Function Map of Commercial Photoresist

64-R-1-18

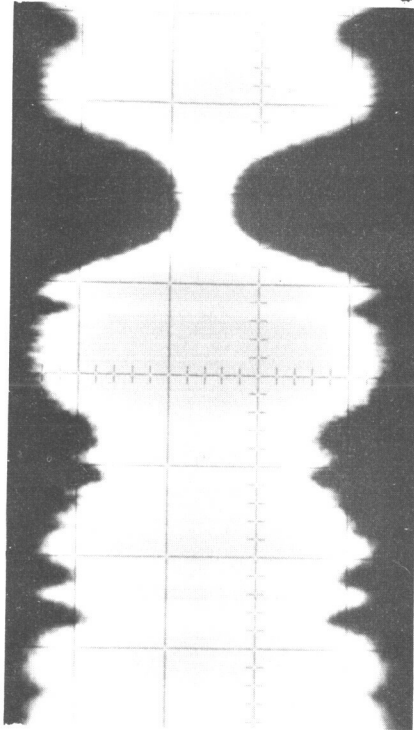


Figure III-11a. Single line scan of surface shown  
in Fig. 9.

64-R-1-19

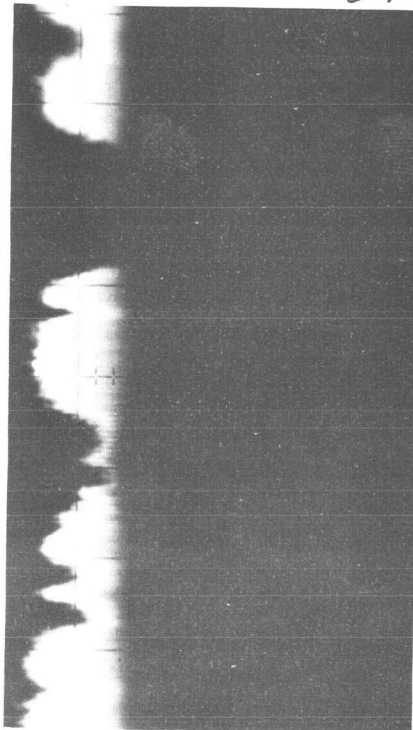


Figure III-11b. Single line scan of surface shown  
in Fig. 9

64-R-1-20

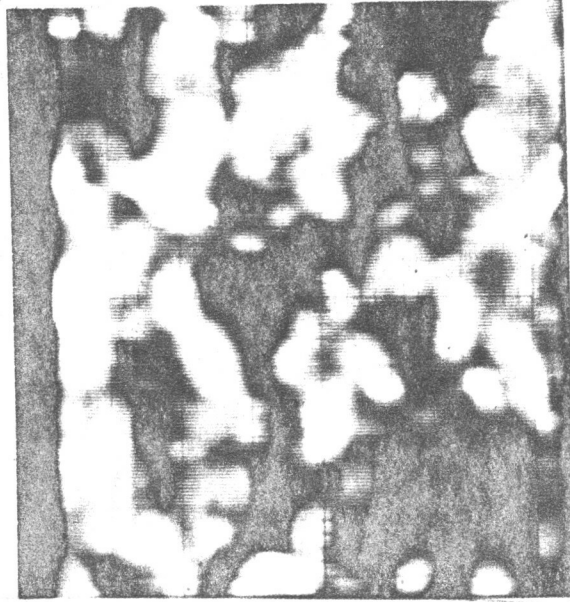


Figure III-12a Work Function Map of a Polycrystalline  
Tantalum Emitter

64-R-1-21

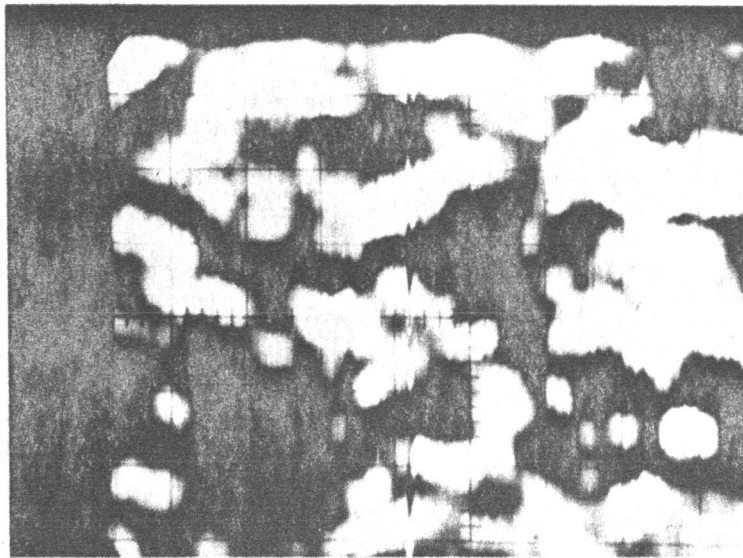


Figure III-12b Work Function Map of a Polycrystalline  
Tantalum Emitter

64-C-1-22

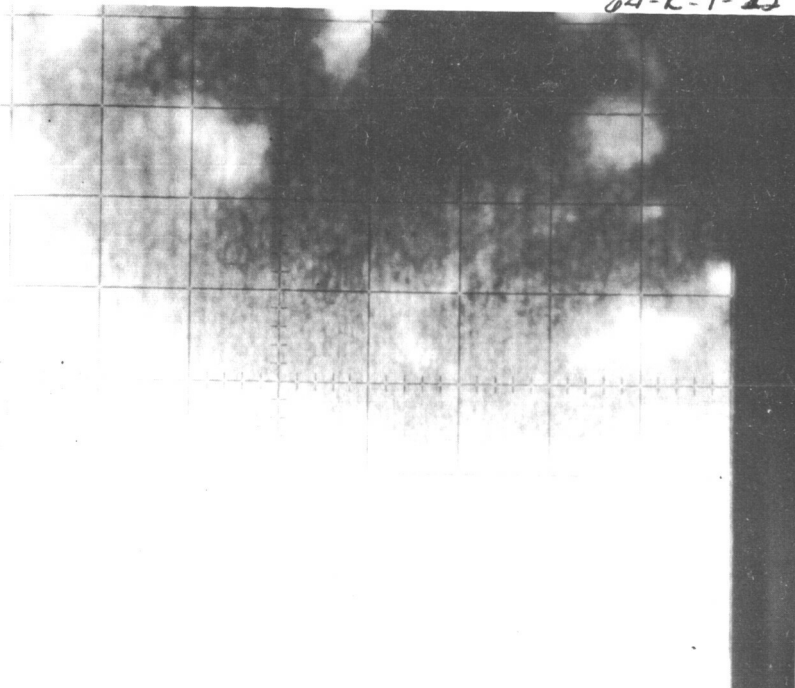


Figure III-13a. Polycrystalline Tungsten Work  
Function map,  $T_E = 3500^\circ K$ ,  $T_C = 3000^\circ K$

64-C-1-23

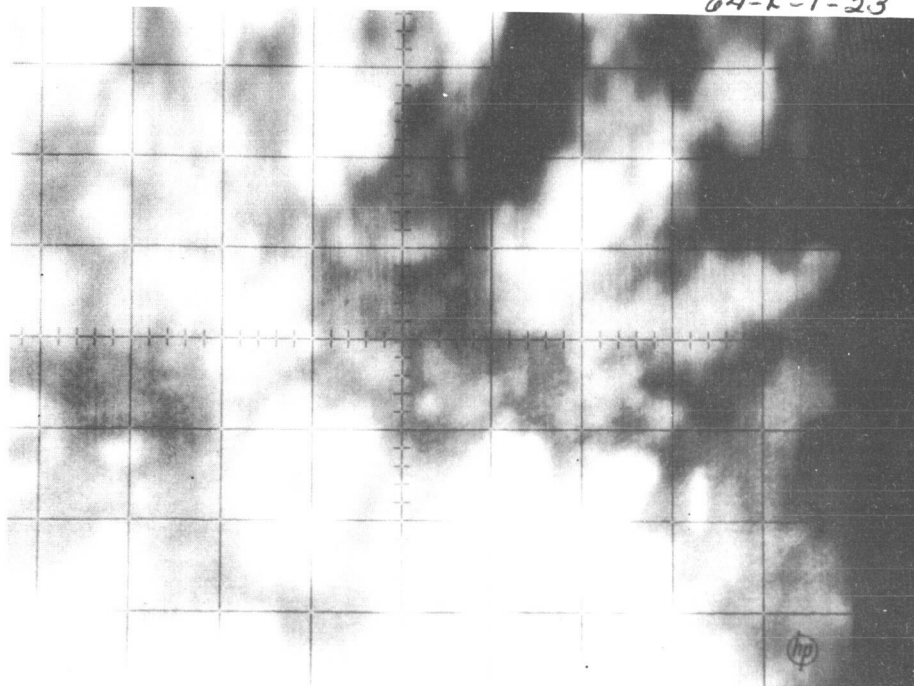


Figure III-13b. Polycrystalline Tungsten Work  
Function map,  $T_E = 6000^\circ K$ ,  $T_C = 3000^\circ K$

64-R-1-24

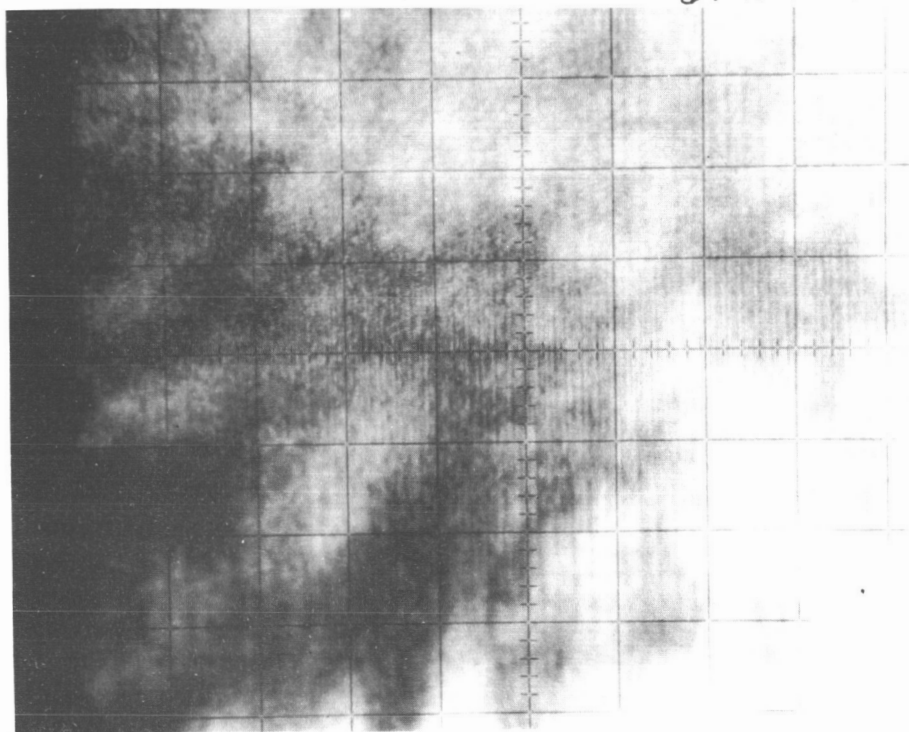
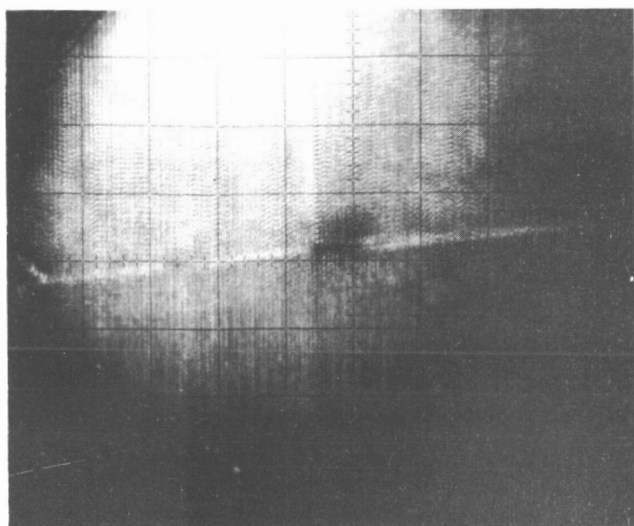
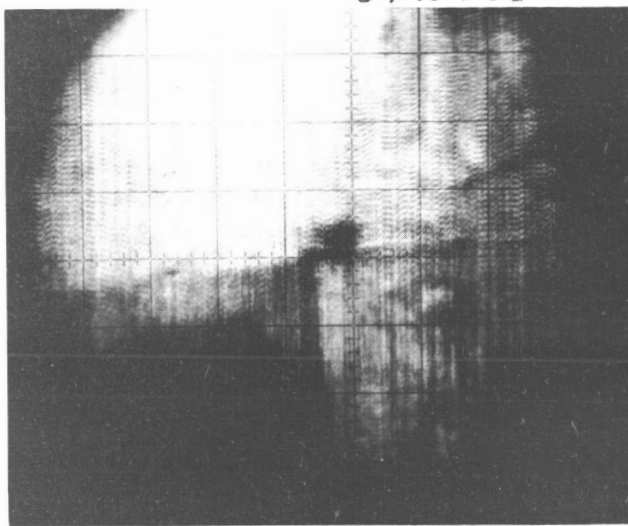


Figure III-13c. Polycrystalline Tungsten Work  
Function Map,  $T_E = 800^\circ K$ ,  $T_C = 300^\circ K$

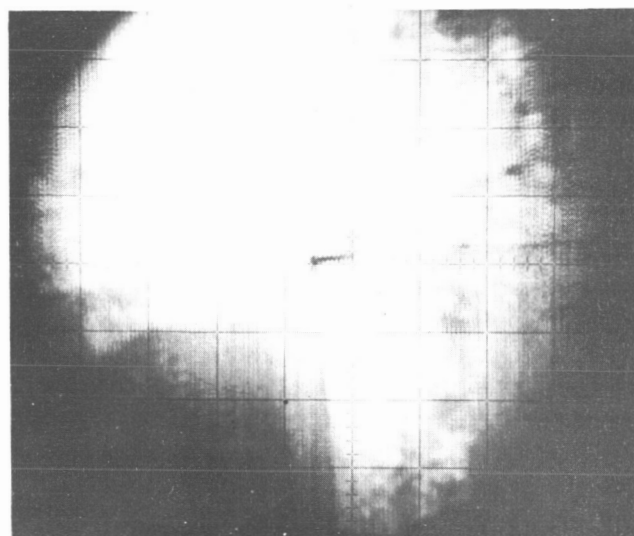
64-R-1-25



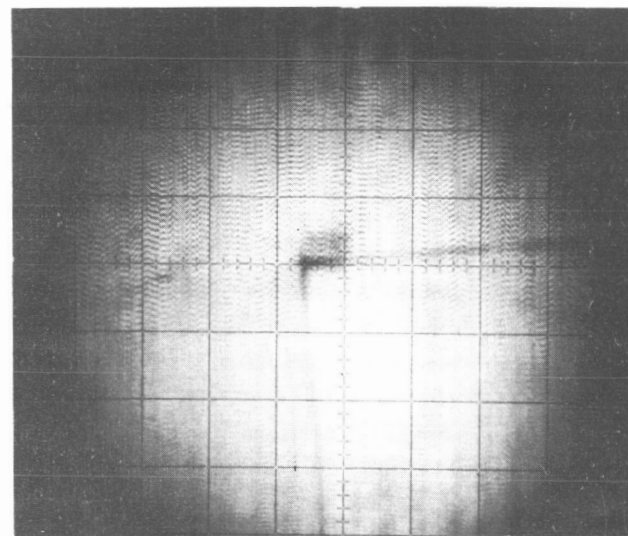
$T/T_R = 1.2$



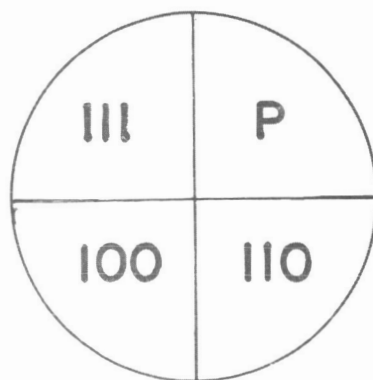
$T/T_R = 1.5$



$T/T_R = 1.9$



$T/T_R = 2.2$



$T_R = 300^\circ\text{K}$

Figure III-14. Work Function Map of Four Quadrant Tungsten Emitter

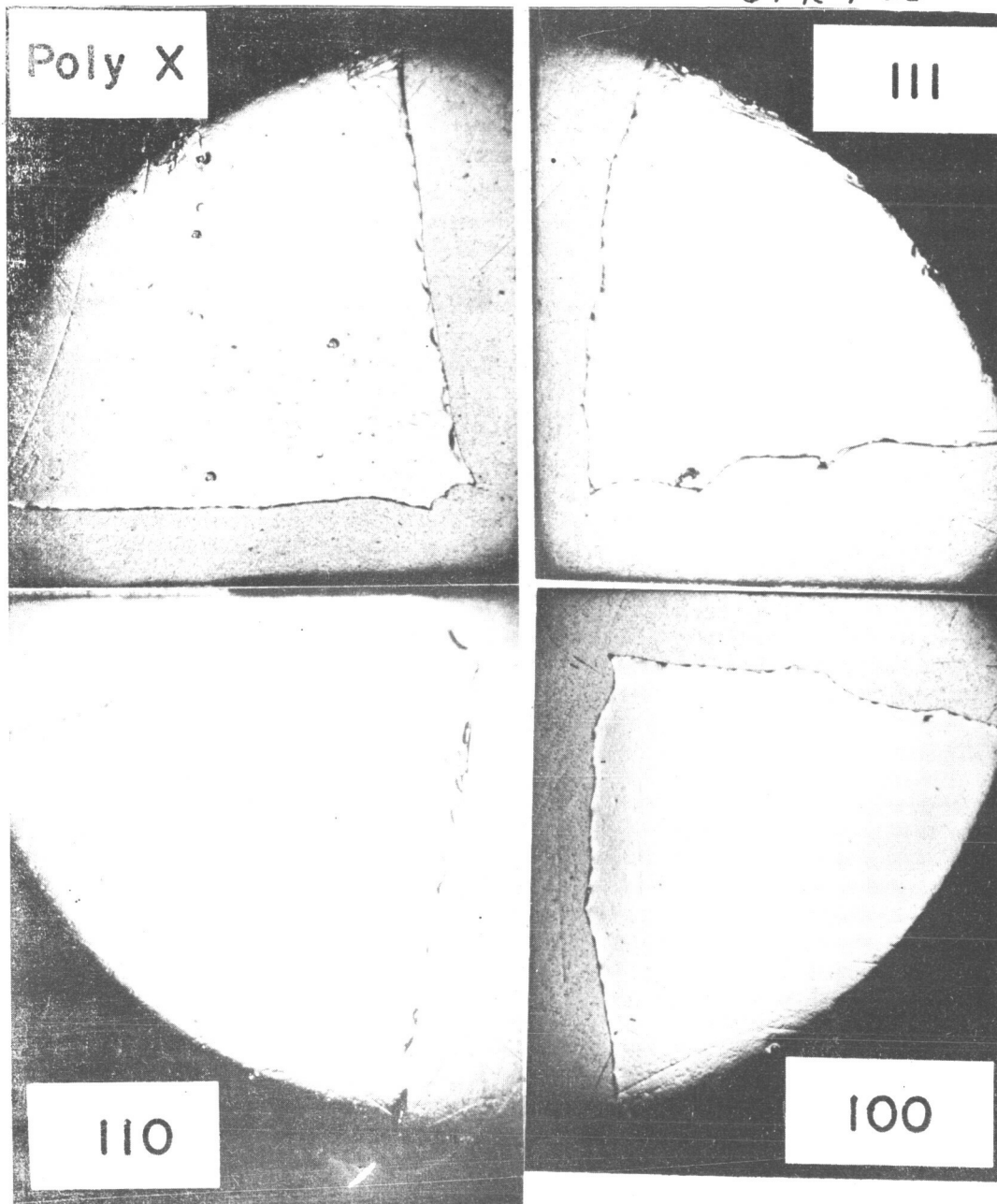


Figure III-15. Photograph of Low Quadrant  
Langster Emitter





## CHAPTER IV

### THERMIONIC SCANNER

#### A. PRINCIPLE OF OPERATION

Assume that the elementary diode shown in Figure IV-1 is placed in a coil capable of producing a strong magnetic field and that the emitter possesses a non-uniform work function over its area. When an accelerating electric field is applied between the emitter and collector, a discharge is produced and a uniform glow is generated in the interelectrode space. When the magnetic field  $B_1$  is turned on, the electrons emitted are forced to follow tight spiral paths from emitter to collector and are prevented from diffusing in the direction parallel to the electrode plane. The uniform flow has now been replaced by "pencils" whose intensity depends on the emission current density. The collector is provided with a small hole, and the electrons passing through the hole are collected by an auxiliary collector. By varying the strength of fields  $B_2$  and  $B_3$ , the paths of the electrons can be deflected through any angle, and the emission current pattern from the emitter surface can be scanned over the hole in the collector. The current from the auxiliary collector can then be used to display this pattern on an oscilloscope in the manner described for the photoelectric system.

#### B. THERMIONIC SCANNER CELL

##### 1. Preliminary Model

The preliminary model of the thermionic scanner cell is shown in Figure IV-2. The emitter (1) is fabricated of tantalum. A one-piece tantalum sleeve is used to connect to the emitter leadthrough (2), and a collector (3) is



opposite the emitter, separated from it by approximately 0.1 inch. A small hole (4) is provided in the collector, allowing electrons to impinge on the probe (5) directly below the small hole. The shield (6) is inserted around the emitter and is intended to reduce stray emissions and permit easy observations of the discharge through the sapphire window (7). The collector is electrically connected to the casing (8). The probe is supported at the end of the nickel tubulation and insulated from the casing by a leadthrough (9). The end of the tubulation holding the probe (10) serves as a trap for any cesium that may enter through the small hole (4). The tube is kept at a low temperature, (20°C) by means of the water cooling coil, condensing all the cesium and maintaining a pressure of  $10^{-6}$  mm Hg. The entire cell may be maintained at any temperature desired using the variable temperature heat sink (11). The electron gun assembly (12) is used to heat the emitter by bombardment. A conventional cesium reservoir is attached at (13). The purpose of the model was primarily to demonstrate and study the principle of thermionic scanning rather than to test fabrication techniques of the advanced model proposed earlier. Therefore, no attempt was made to make the appearance of this preliminary model similar to the final model or to make the emitters interchangeable with those in the photoelectric scanner or the converter. A second model for this purpose is described below.

A cross section of the proposed design for the advanced thermionic scanner is shown in Figure IV-3. It consists of two chambers. The main chamber, located between the emitter (1) and the collector (15) contains cesium vapor at a relatively high pressure — of the order found in an operating converter. The second chamber, located inside the collector and containing the probe (18) is maintained at a cesium pressure corresponding to room

temperature ( $\sim 10^{-6}$  mm Hg). This is accomplished by connecting reservoir (24) to the water cooling coil directly.

It should be noted that the emitter assembly, which includes all the parts above the gasket (6), is identical to the one employed in the test converter and in the photoelectric scanning device. This feature permits the incorporation of a given emitter into any one of these three devices with a minimum of handling and alteration.

The emitter temperature is observed with an optical pyrometer in the blackbody hole provided on the rear face of the emitter. An additional hole is provided on the back face of the emitter for the insertion of high temperature thermocouples if their use is deemed desirable. The heat conducted by the thin-wall emitter spacer, is rejected by the radiator (3). The size of this radiator has been determined by calculations so that the entire emitter structure is maintained at about 900° K or below throughout the entire range of emitter temperature employed. This temperature is a suitable operating temperature for the getter (7) which is made of titanium. The getter has been incorporated in the device for the purpose of collecting any gases that may evolve from the parts of the device after outgassing. A sapphire window (9) has been included to enable the observation of the discharge during operation, and the measurement of the deflections produced by the auxiliary magnetic fields. This sapphire window can easily be replaced by cutting the heliarc weld to the window insert (10).

The envelope of the cell (8) is joined to the collector (15) by means of a leadthrough (11). This leadthrough is not used as a mechanical support. Support as well as cooling is provided by part (17) which is brazed to the collector and mechanically joined to the envelope (8) with a thin sheet of mica



interposed between the two for electrical insulation. The probe (18) is supported on a nickel tube (19). This tube is held in position by a leadthrough (21). The extreme lower end of the tube (19) forms the cesium reservoir of the second chamber. Any cesium that enters through the aperture on the face of the collector is condensed, and the cesium pressure is maintained at a level corresponding to cooling water temperature. Eventually, all the cesium of the main chamber will be distilled into this reservoir. This would take several hundred hours of operation, however, and therefore is of little concern. Part (17) provides cooling for both the collector and the envelope of the unit. The temperature of both the collector and the envelope can be regulated by adjusting the heat input into the variable temperature heat sink (23).

The model described above was not actually constructed. As mentioned in Chapter III the experience with the preliminary model of the photoelectric scanner had shown that several items, i. e., the demountable seal, of that design were not found to be practical. Also, the over-all size of the unit was reduced by redesign permitting greater scanning resolution ranges without an increased magnetic field.

## 2. Advanced Model

Based on the experience with the photoelectric scanner and preliminary models of the thermionic scanner, a prototype was built as shown in Figure IV-4. Parts 1 through 7 comprise the emitter assembly and have already been described under photoelectric scanner, Chapter III. The emitter assembly for the two advanced-model scanners, and the converter are identical and fully interchangeable. Emitters are mounted and demounted by welding the flange and cutting the weld open, respectively. Sufficient length has been incorporated



into this flange to allow the replacement of the emitter several times. The collector (21) has a larger area than the emitter. This is to allow electrons to be collected even when the electron stream is deflected at a  $45^\circ$  angle. A small hole in the collector (22) is provided to allow the electrons to pass through to the probe (23). The small hole is approximately 0.0025 inch in diameter. The probe (23) is connected by a molybdenum rod of substantial cross-section to a probe leadthrough (24). This leadthrough has an intermediary flange which serves for additional insulation between the collector and the probe, and may be used for a bias control. At the end of the molybdenum rod, a provision is made for attaching a thermocouple and clamping to the water reservoir which maintains the probe temperature as close to water temperature as possible. Finally, a cup (25) is used to thermally isolate the collector from the probe. The main collector is connected to the body and to the emitter via leadthrough (26). This model has a fixed spacing, therefore the leadthrough is of a rigid design. A molybdenum ring (27) is provided to maintain the casing at the same temperature as the collector. This ring is insulated from the collector with a mica sheet. The casing is fabricated of nickel and, therefore, during operation its temperature must be raised above the Curie point. To facilitate this, an additional heater filament was included in the electron gun to heat the radiator and consequently the casing. This heater was used for tests conducted at low emitter temperatures. A cesium reservoir is connected at the tubulation (28).

### C. THERMIONIC SCANNING SYSTEM

The most critical component of the thermionic scanning system is a set of coils to achieve suitable collimation and controlled deflection of the magnetic field in the emitter collector interspace. It is desirable to generate the highest possible magnetic fields without the use of iron to permit rapid change in the



fields during scanning. The most practical way to generate this field is by the use of water-cooled copper coils.

Figure IV-5 is a schematic arrangement of the thermionic scanner coils. In this figure, the collimating field coil is seen to surround the entire thermionic scanner casing. Two pairs of coils are disposed in the X and Y directions to obtain the scanning. The deflection coils are potted in epoxy to prevent distortion due to the strong magnetic field. Since the coils are composed of relatively few turns, a high current is required to produce a magnetic field. Two coils, X, are wired in series to provide the X deflection of the electrons; two coils, Y, are also wired in series to provide the Y deflection. The coils, X, are operated at low frequency, 1 or 2 cycles per minute, while the Y coils are operated at 60 cycles per second. The combination of the two motions generates a two-dimensional scan of the emitter surface past the aperture in the collector. The constant current for the collimating coil is supplied by a motor generator set and is controlled by water-cooled resistance banks as well as a field rheostat on the generator. Up to 200 amps may be obtained in this manner. The X deflection coil is powered by a step-down transformer connected to the 60-cycle ac main. The current is controlled by an autotransformer, and this system is capable of producing currents up to 200 amps peak-to-peak. The Y deflection current is obtained from a low-voltage, high-current regulated dc power supply programmed by the sawtooth voltage from the display oscilloscope. Since this is a dc supply, only one-half of the emitter surface may be scanned at one time, and the connections to the deflecting coils must be reversed in order to scan the other half. The current in these coils is limited to 150 amps peak-to-peak by the capability of the supply. A field of intensity of about 200 gauss can be obtained from the deflection coils. Figure IV-6 shows the scanning and display system electronics. The display system uses a modified Type 536 Tektronix



oscilloscope with Type T and Type B plug-in amplifiers. Vertical deflection is obtained through a phase-shifting circuit from an extra winding on the X-scanning transformer. Horizontal deflection is obtained directly from the time base. A negative-going sawtooth from the horizontal output terminal is used to drive the Y-deflection power supply. At this low scanning frequency, no phase problem exists.

#### D. SIGNAL DETECTION AND AMPLIFICATION

The signal from the auxiliary collector has a very-low-frequency component because of the low scanning rates involved. It is, therefore, necessary to use dc amplification throughout the intensity modulation (Z axis) system. The auxiliary collector is connected directly to a Tektronix Type B pre-amplifier with a Type 132 power supply, as shown in Figure IV-6. Sufficient gain is available to completely modulate the intensity within the range of emitter and cesium temperatures. Contrast is controlled through gain, and brightness by adjusting either the intensity control or the dc level. No probe collecting voltage or lead resistor other than the pre-amplifier was used. At the low scanning frequencies used, direct visual observation is very difficult and photographic techniques must be used. A film with a good range of grays must be employed to produce the variations apparent in the output waveform. Calibration of the film is accomplished by feeding a known input to the Z axis pre-amplifier. The display of the signal produced by the X scan may be obtained by switching the vertical input to the Z axis amplifier output and sweeping at a 60-cycle rate.

#### E. EXPERIMENTAL RESULTS FROM THERMIONIC SCANNER

##### 1. Preliminary Experiments

Runs were made with the polycrystalline tantalum emitter with various emitter and cesium temperatures, and with different collimating fields.



Photographs of these results are shown in Figure IV-7. In each case the deflecting fields were held constant. The brightness and contrast of the display were adjusted for the best picture with emitter and cesium reservoir temperatures of  $1210^{\circ}\text{K}$  and  $420^{\circ}\text{K}$ , respectively, resulting in Figure IV-7a. At an emitter temperature of  $1260^{\circ}\text{K}$ , shown in Figure IV-7b, the average current has decreased and the patch effect is much less pronounced. At an emitter temperature of  $1130^{\circ}\text{K}$ , shown in Figure IV-7c, the reverse effect occurs with great contrast between the active and inactive areas. At a lower cesium temperature ( $400^{\circ}\text{K}$ ) as shown in Figure IV-7d, a behavior similar to that at a high emitter temperature is obtained. With the higher cesium temperature ( $450^{\circ}\text{K}$ ) shown in Figure IV-7e, the prominent patches observed at a low emitter temperature are not apparent. The amplifier gain in each case was maintained constant while the dc level was varied to maintain nearly the same average brightness at the start of each scan. Figures IV-7f, IV-7g, IV-7h show the effects of collimating field currents of 0, 50 and 150 amperes, respectively. It can be seen that, as the collimating field is increased, the deflection angle decreases and the picture is, therefore, apparently magnified with a smaller portion of the emitter being displayed. At the same time the resolution is increased. The bright area in the pictures is about  $1/8$  inch in diameter, so that the smallest patches observed are about 0.010 inch in diameter, as shown in Figure IV-7h. Higher currents did not appreciably change the resolution but caused further magnification.

The above discussion is qualitative. In order to obtain quantitative results single-line cross scans were obtained at various locations on the emitter. These cross scans are not shown here but are similar to those in Figures IV-10, -11, -12. The cross scan results were analyzed as explained in Section 2 below, and the resulting work function values have been superimposed on the corresponding



photographic map to clarify the relationship between the quantitative and qualitative results. This is illustrated by Figure IV-8.

## 2. Experimental Results

The composite emitter, Figure III-15, was incorporated in the thermionic scanner, where it was heated at 1600° C for 12 hours. Figures IV-10, -11, -12 show the results obtained with the thermionic scanner when the reservoir temperature was maintained constant at 420° K and the surface temperature was varied. The area displayed in these photographs is only about half the radial distance from the center of the emitter. Also included in the figures are the cross scans corresponding to each photographic map. These cross scans have been obtained along the line in the photograph opposite each trace line zero. The magnitude of signal at each point represents a given value of collected current and can be used to calculate the corresponding work function value by substituting in the Richardson equation.

The most striking result is that the polycrystalline and  $\langle 100 \rangle$  quadrants emit very little current compared to the other quadrants. Using the area of the hole and the measured probe current, apparent values of the local work function at a given feature can be computed from the current profiles, using the Richardson equation with  $A = 120 \text{ amps/cm}^2 - ^\circ \text{K}^2$ . Such values are plotted in Figure IV-9, and their dependence on  $T/T_R$  may be compared with the theoretical curves for three different bare (vacuum) work function values ( $\phi_0$ ). The brightest (highest current) features, i. e., most of the  $\langle 110 \rangle$  and the brightest patches in the  $\langle 111 \rangle$  quadrant, fall on or near the curve corresponding to a bare work function of  $\phi_0 = 4.6 \text{ ev}$ . The light gray and dark gray plateaus between the bright patches in the  $\langle 111 \rangle$  quadrant correlate with about  $\phi_0 = 4.4 \text{ ev}$  and  $\phi_0 = 4.3 \text{ ev}$  respectively, as may be seen in Figure IV-9. Currents from the



dark quadrants were obscured by noise, but they appear to correspond to  $\phi_0 < 4.2$  eV over their entire surface. This latter result is quite surprising, especially since these quadrants contain mechanically polished areas and large etch pits which do not appear in the display.

The data shown were taken with the converter operating just beyond saturation in the first (i.e., intermediate or low-current) ignited mode. When the applied potential difference was further increased into the second (arc of high current) ignited mode, the current from the brightest patches would begin to increase with the onset of a noise (rf) component. Under these same conditions, emission from the cavity between the polycrystalline and  $\langle 110 \rangle$  faces would begin to dominate the display pattern. Other areas were unaffected, however. This effect became more intense as the work function  $\phi$  decreased into the electron-rich region below the "neutralization" work function  $\phi_n$  shown in Figure IV-9. In fact, for  $T/T_R < 2.2$ , the only observable feature was intense emission from the cavity, as confirmed by visual inspection through the sapphire window.

Figure IV-13 shows a photographic map and several cross scans of a single-crystal  $\langle 110 \rangle$  tungsten emitter which was also examined in the thermionic scanner. In contrast to the composite emitter previously discussed, these cross scans show remarkably little variation across the face, indicating a relatively uniform emitter.

To obtain quantitative results measurements of photocurrent vs. diode voltage were taken. These are displayed in Figures IV-14a and IV-14b. The resulting values of work function, as computed from the probe characteristics, are shown as open circles in Figure IV-9. These are in complete agreement with the  $\langle 110 \rangle$  results from the composite emitter, which are shown as solid circles



on the same figure, and with the points shown as solid triangles which were obtained by operating the  $\langle 110 \rangle$  emitter in a test converter.

Except for changes noticed during initial heating in the photoelectric scanner, no time-dependent changes in the emission pattern of any emitter at a given value of  $T/T_R$  have been observed. It must be emphasized, however, that emitters have not been subjected to temperatures above  $1800^\circ\text{K}$  during the test series.

A notable exception to the above statement occurred when the metal envelope of the thermionic scanner cell was heated well above its previous operating point, with other variables held constant. On this occasion, the emission display abruptly changed to a new, diffuse and varying pattern which, after about  $1/2$  hour, returned to the original stable pattern. This presumably occurred due to the release of impurities into the cell atmosphere which contaminated the surface.

It has been observed that the degree of resolution of the thermionic scanner pattern is dependent on the value of the quantity  $H^2/p$  where  $p$  is the cesium pressure and  $H$  is the collimating magnetic field. Since only moderate magnetic fields have been employed (i. e. ,  $< 300$  gauss) the use of reasonably larger fields should permit operation at higher emitter temperatures and cesium pressures than employed thus far. Furthermore, by reducing the size of the collector orifice and by obtaining higher probe leadthrough resistance, higher magnetic fields should permit substantially greater resolution to be obtained.

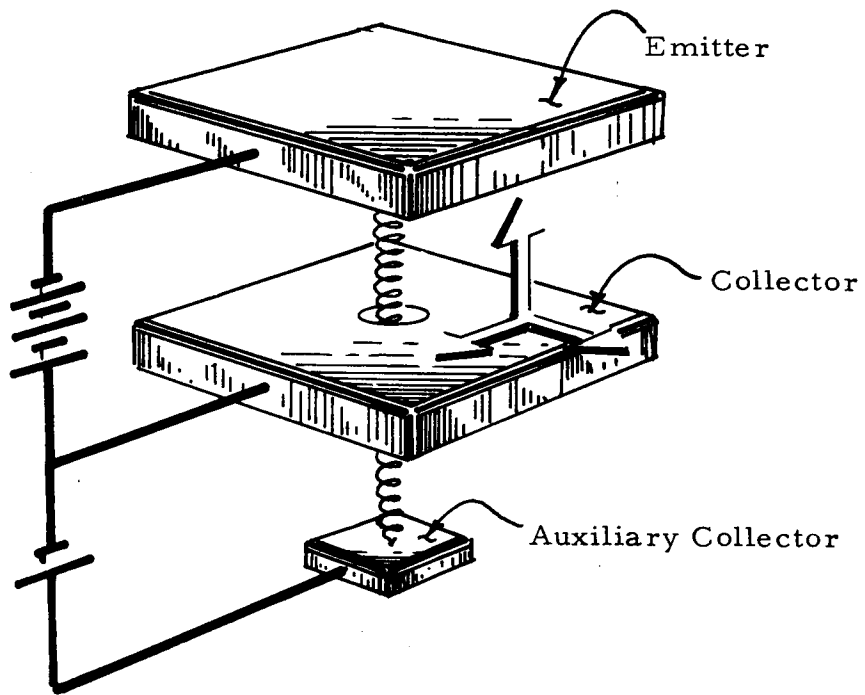


Figure IV-1. Elementary Diode in Magnetic Field

64-R-1-74

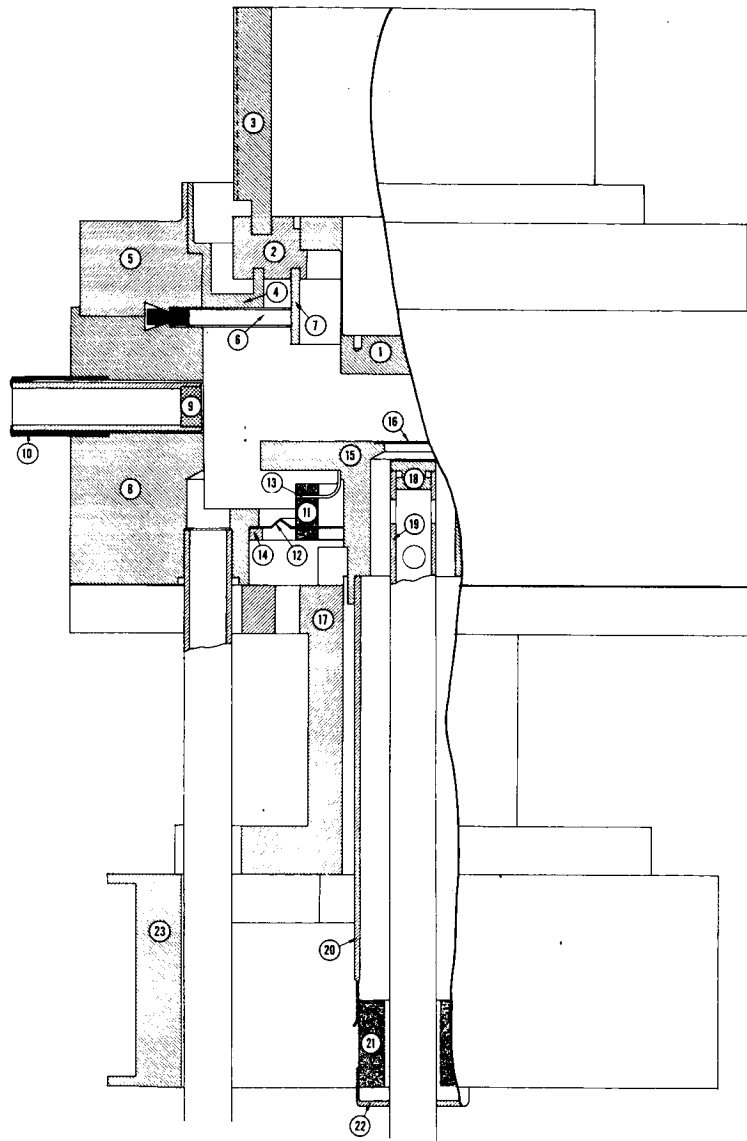
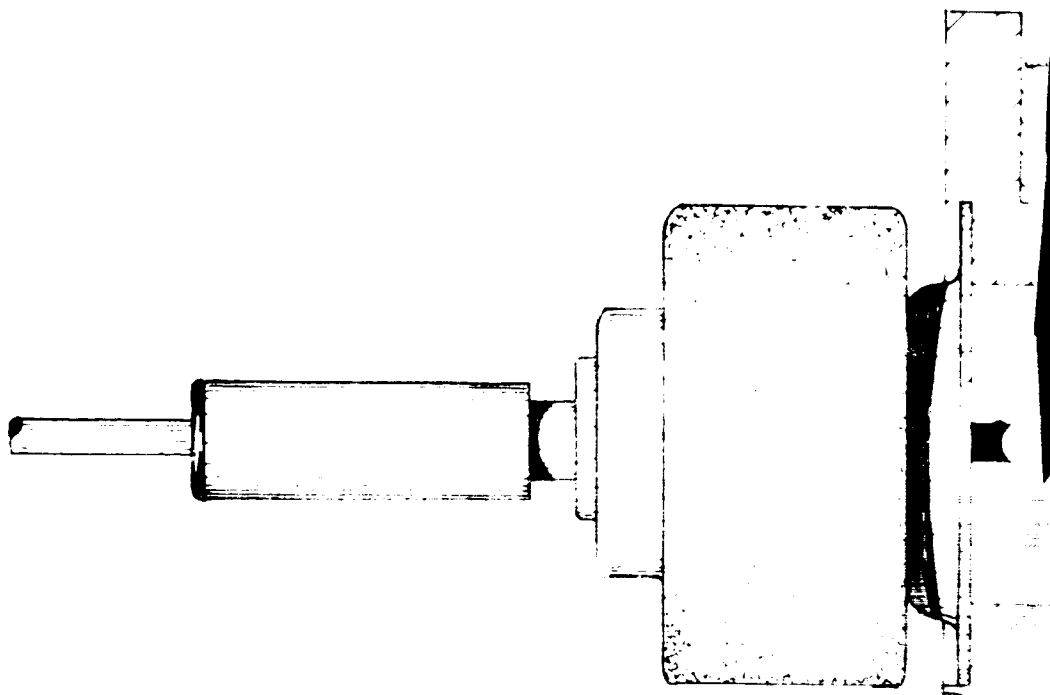
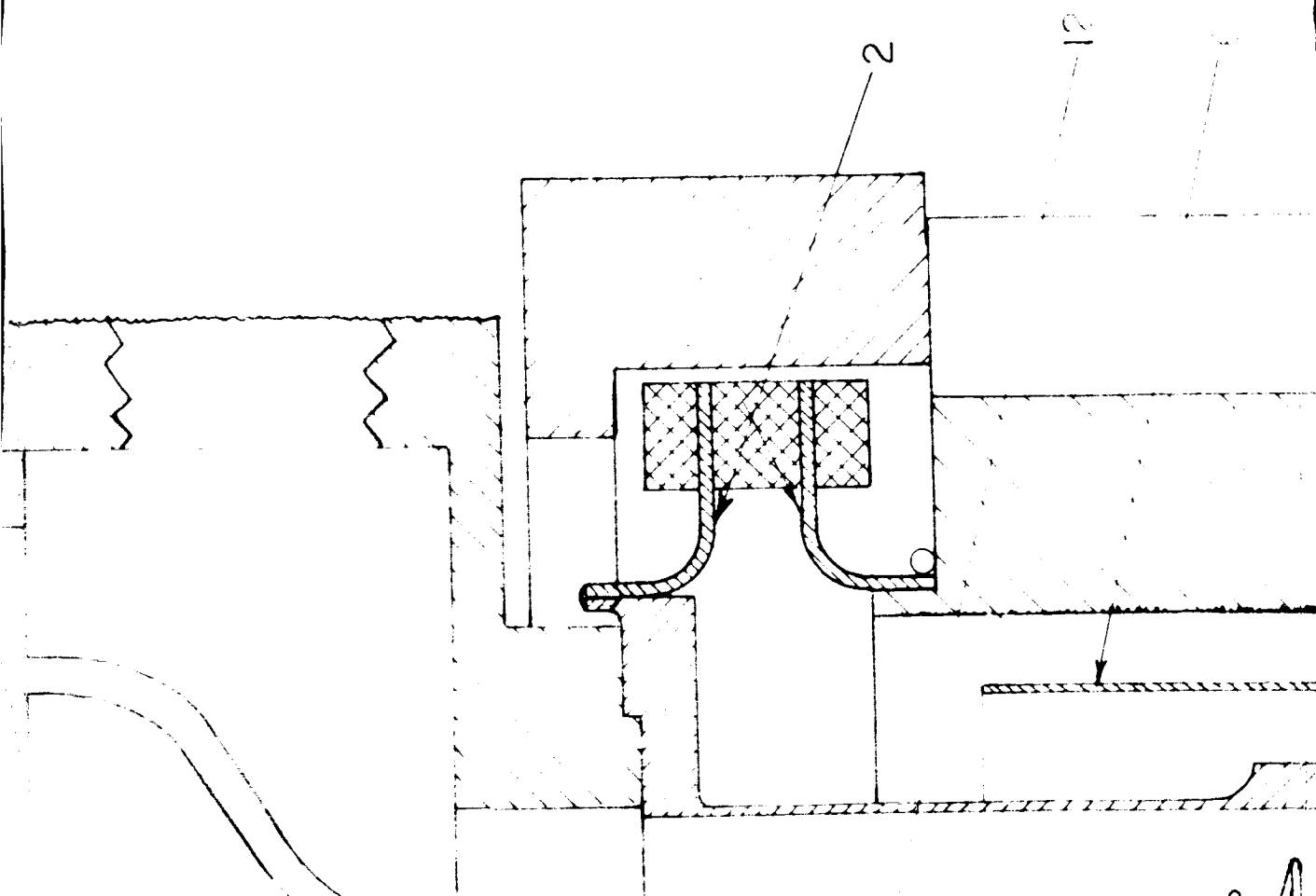


Figure II-3. Assembly of Proposed model of  
Advanced Thermionic Scanner

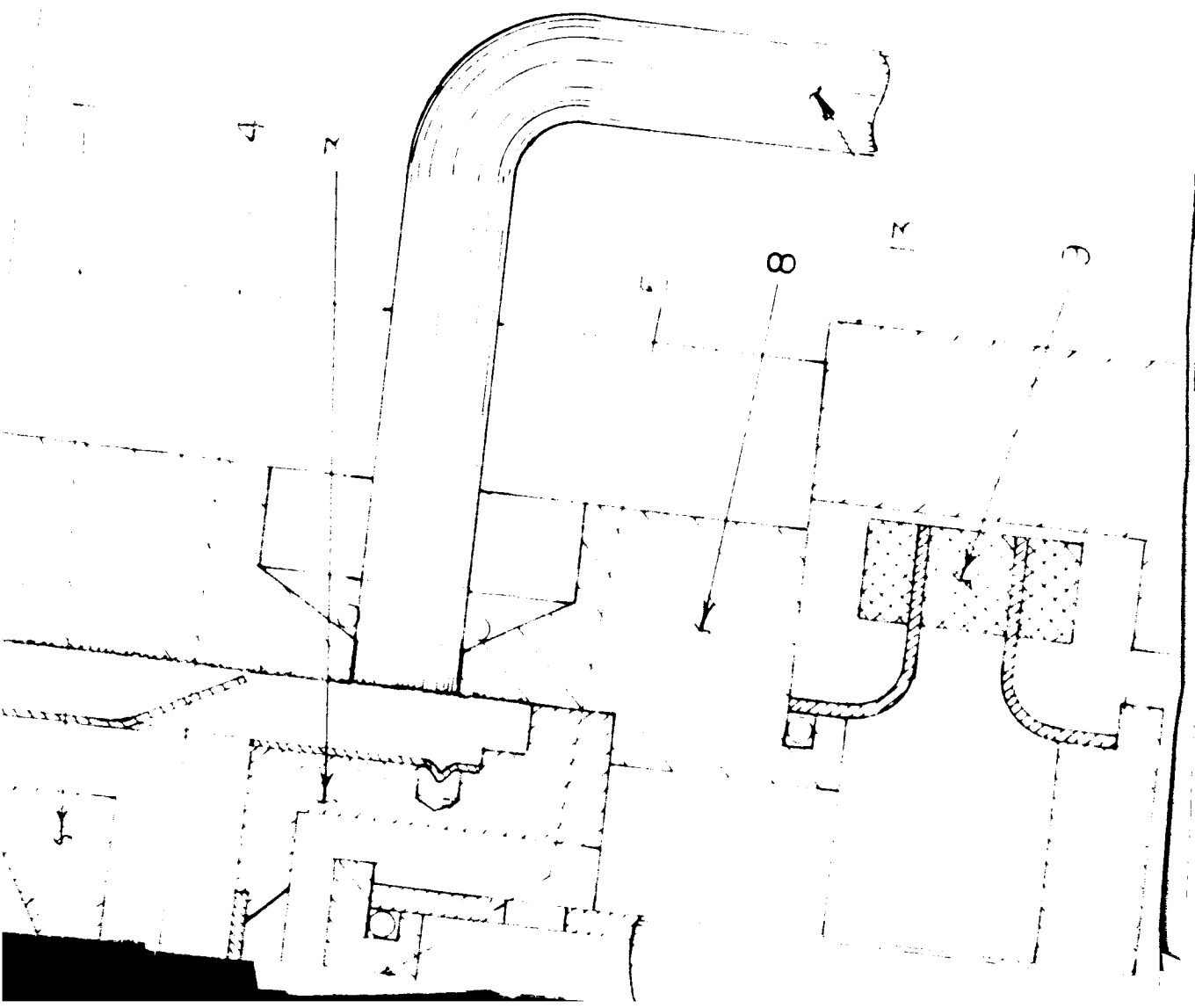
(1)



(2)

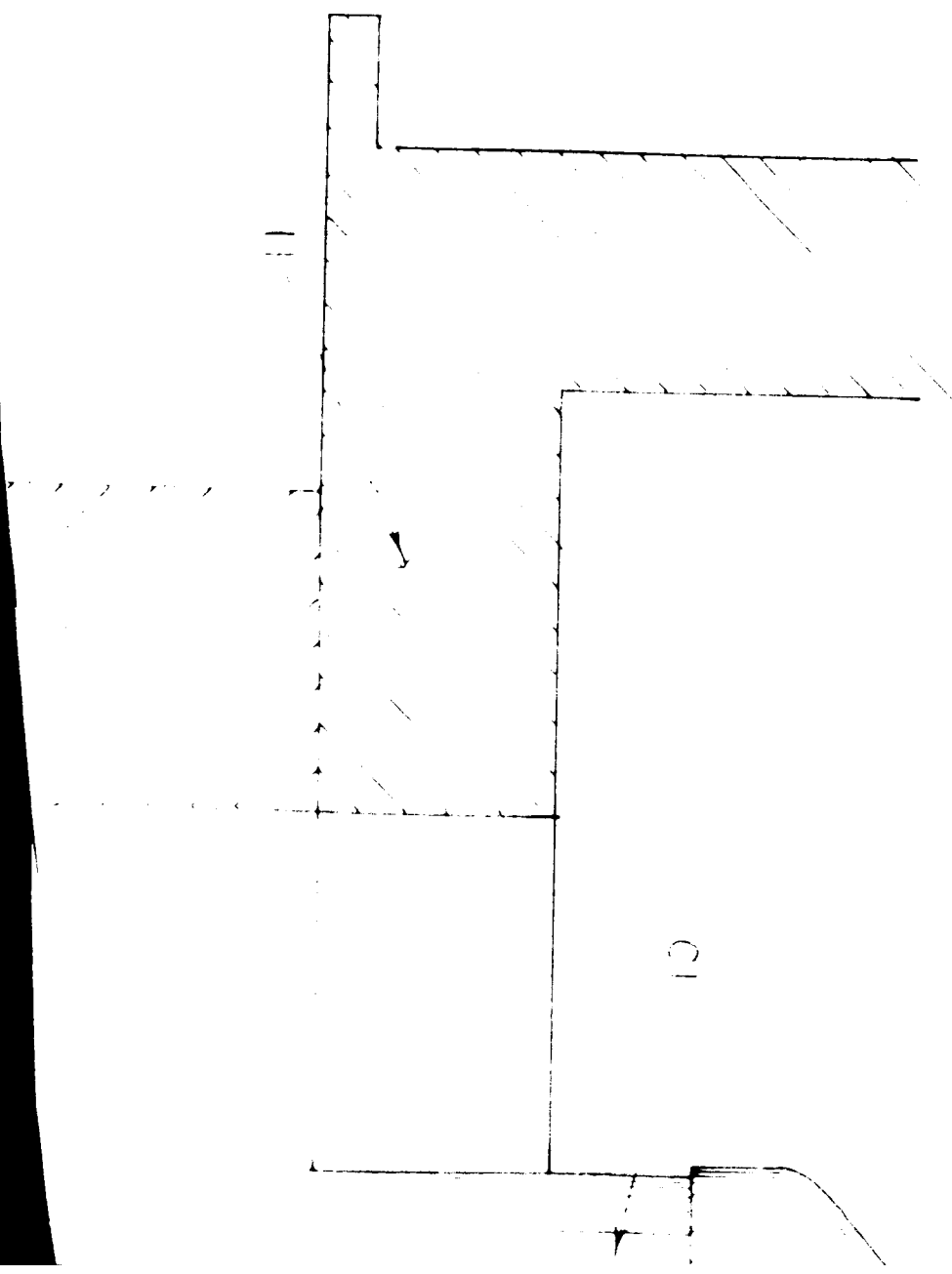


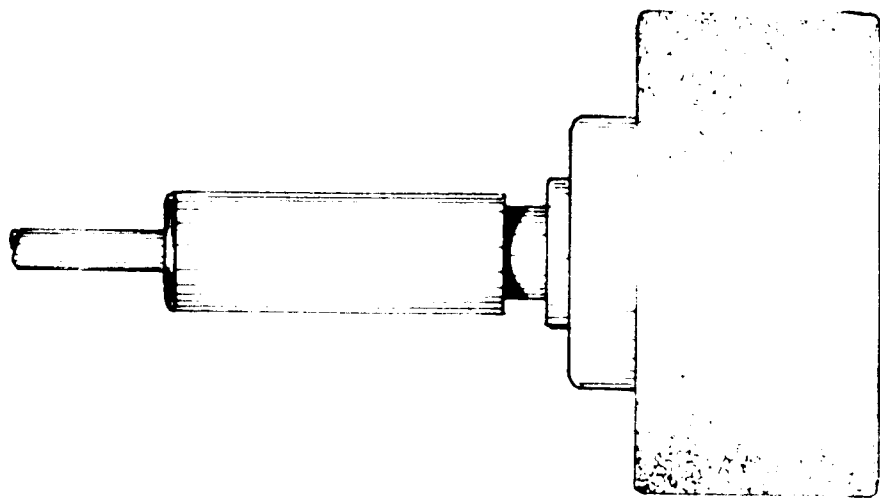
(3)





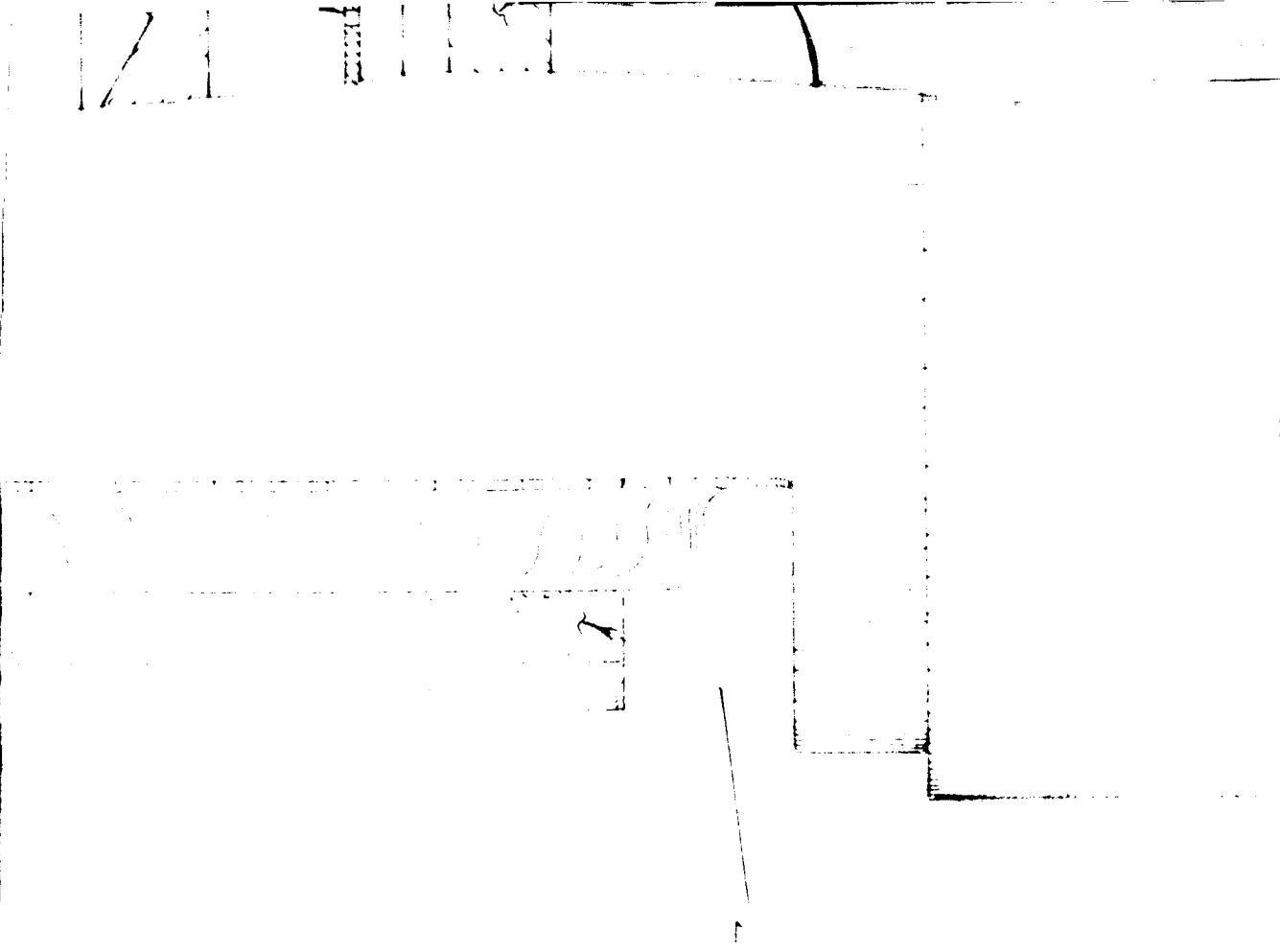
9)





(5)

(6)



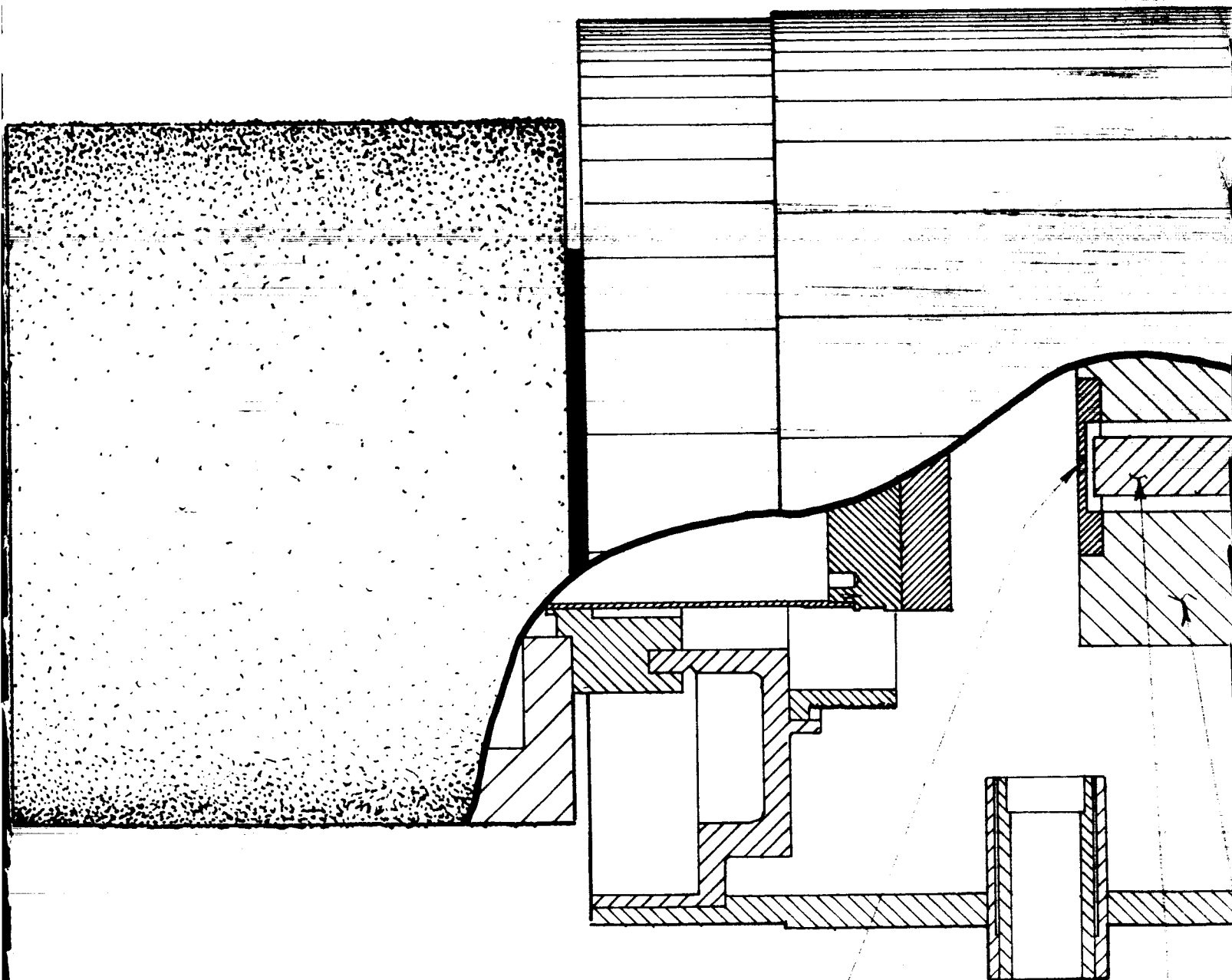
C/1



(8)

(9)

Figure IV-2 Assembly of Preliminary  
Model of Thermistor Scanner Cell



22

23

Drawn  
501

IV-4

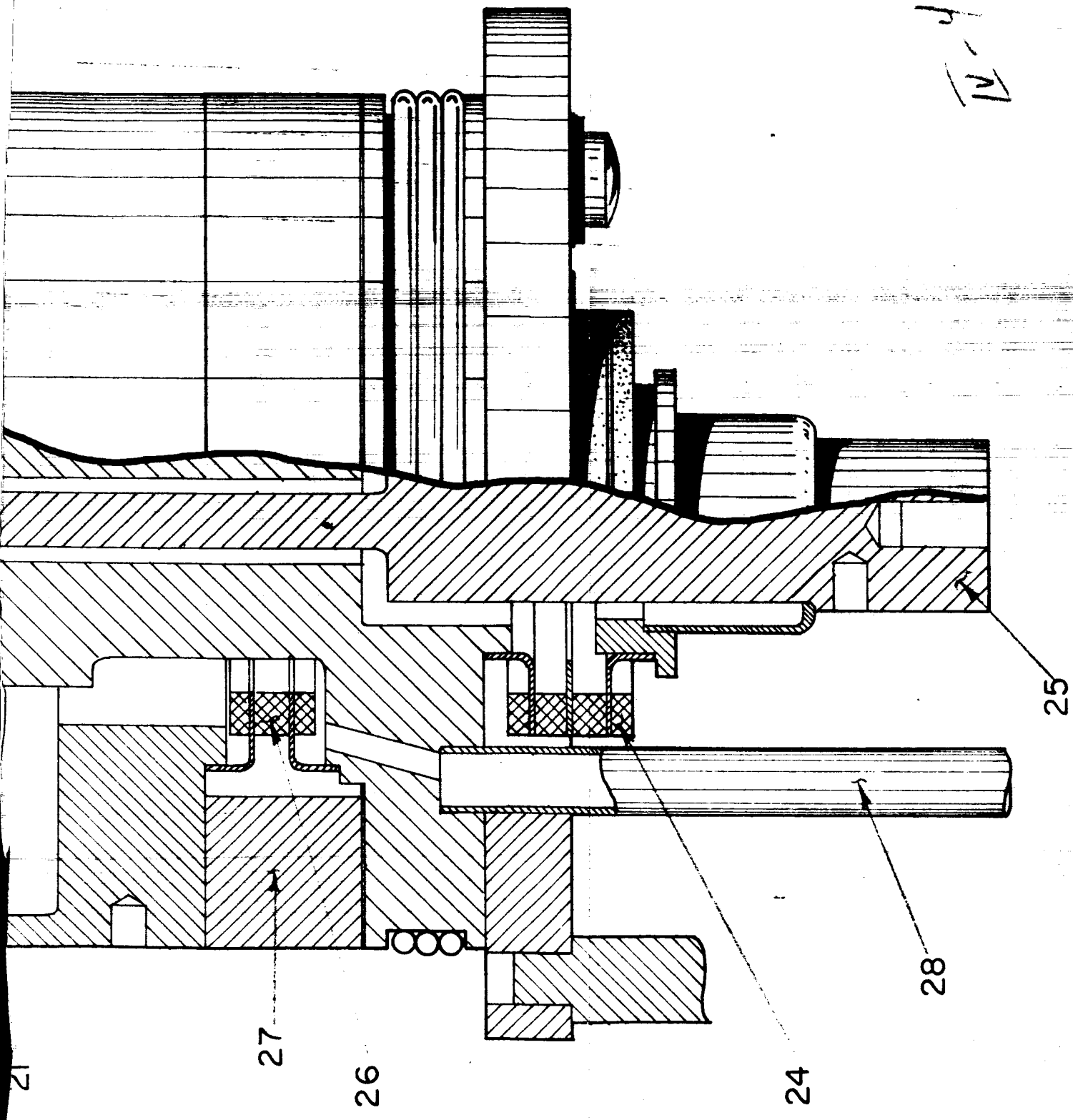


Figure IV-4 Assembly of Advanced Model of Thermite Scanner Cell



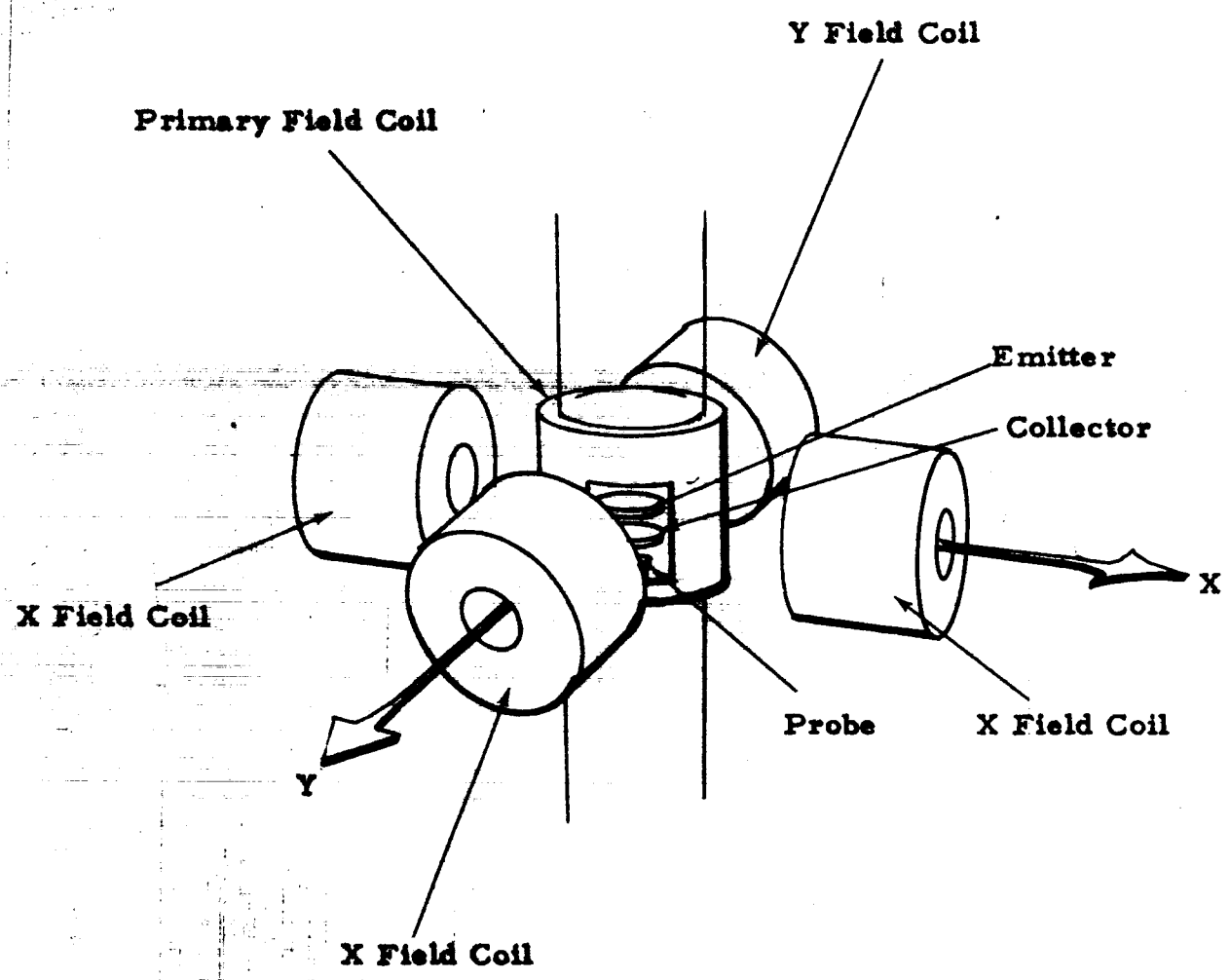
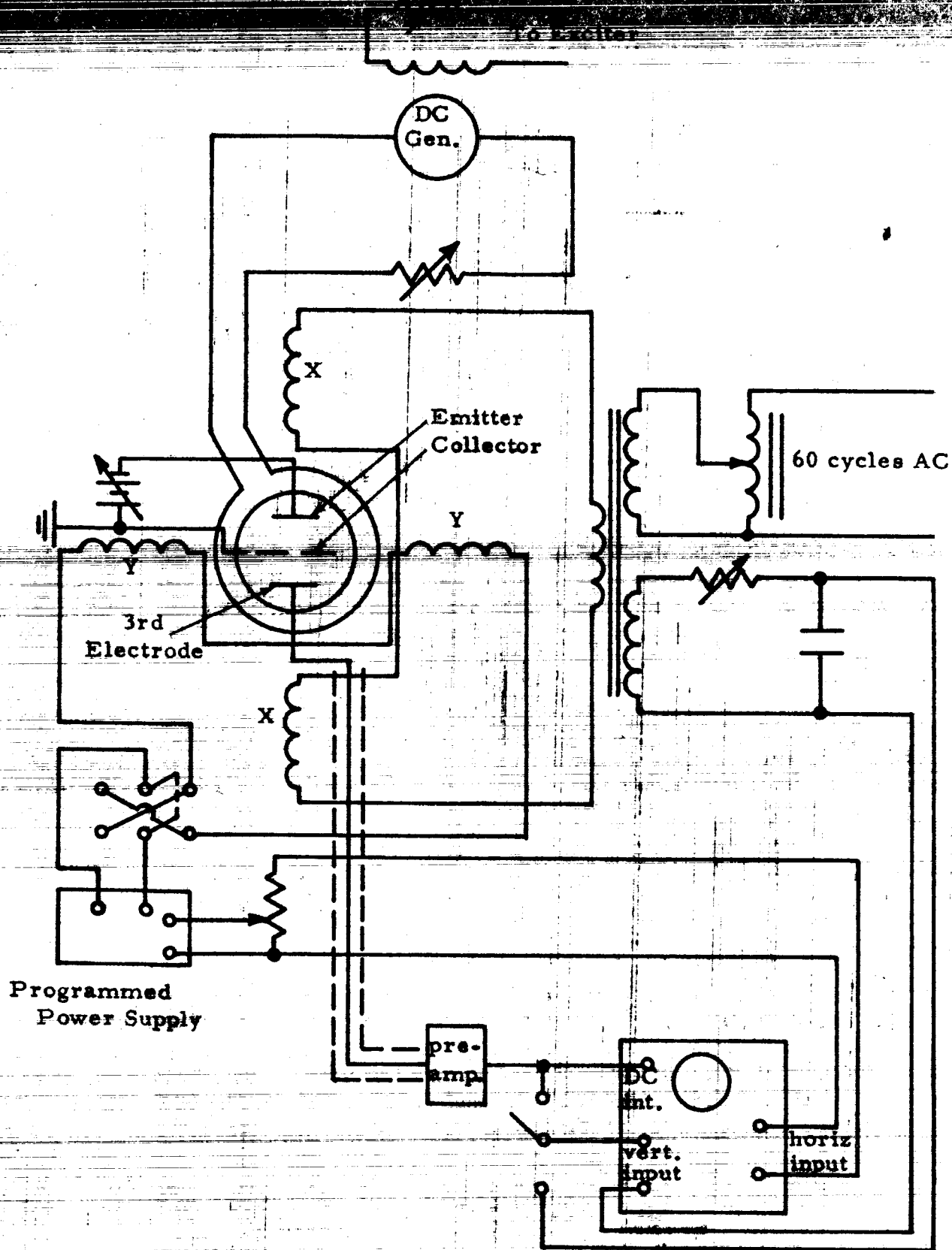


Figure 15-5. Schematic of Thermionic Scanner Coil.



**Figure IV-6 Schematic of Thermionic Scanner Scanning and Display Systems**

64-R-1-78

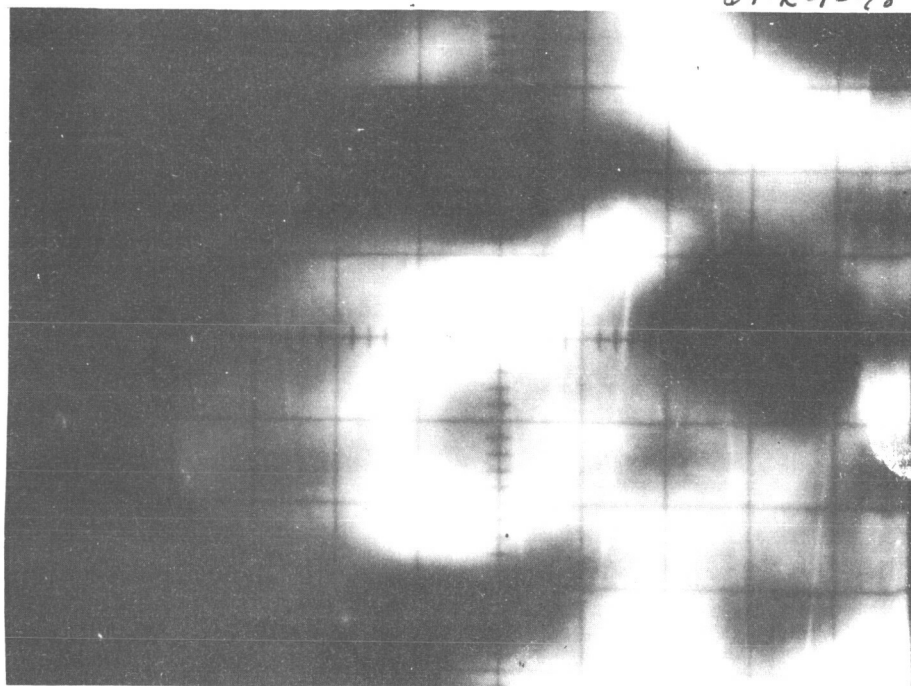


Figure II-7a. Thermionic Scanner Work Function

map,  $T_E = 1210^\circ K$ ,  $T_C = 420^\circ K$

64-K-1-79

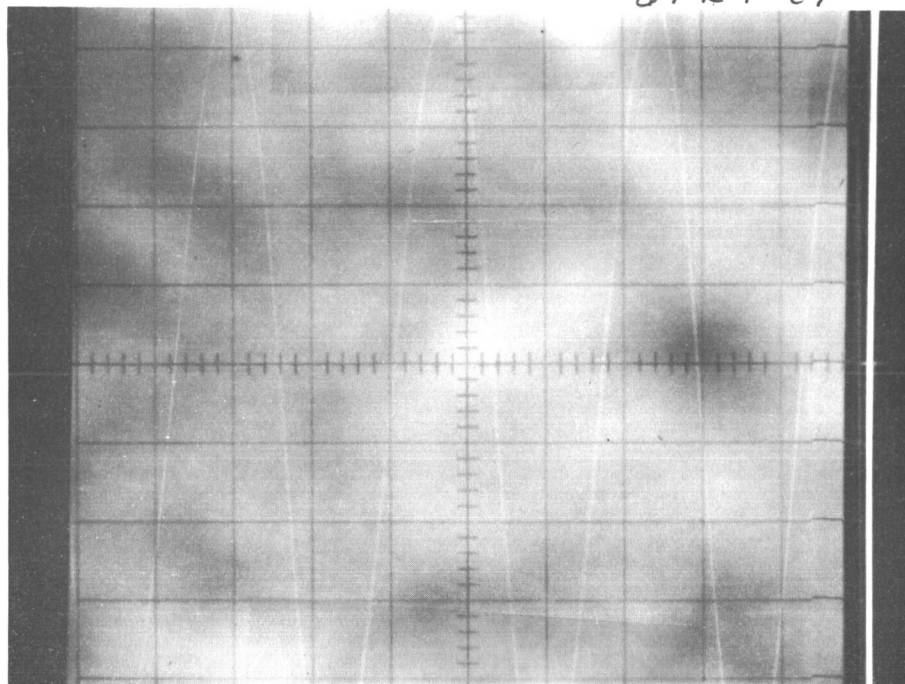


Figure II-7b. Thermionic Scanner Work Function

map,  $T_E = 1200^\circ K$ ,  $T_{C_0} = 420^\circ K$

64-R-1-80

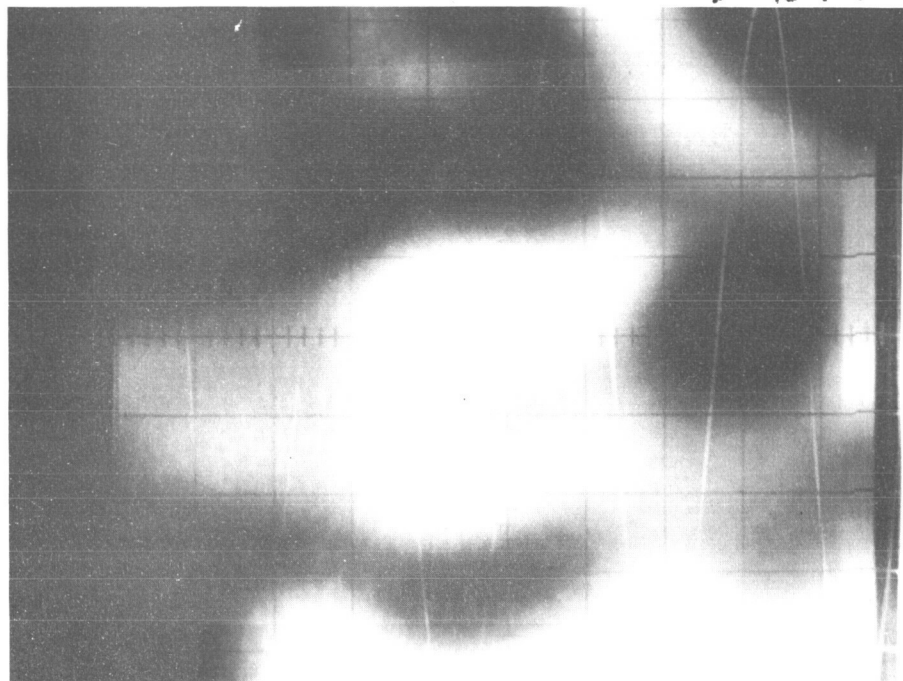


Figure II-7c. Thermionic Scanner Work Function

map,  $T_E = 1330^\circ K$ ,  $T_{C_0} = 420^\circ K$

64-R-1-81

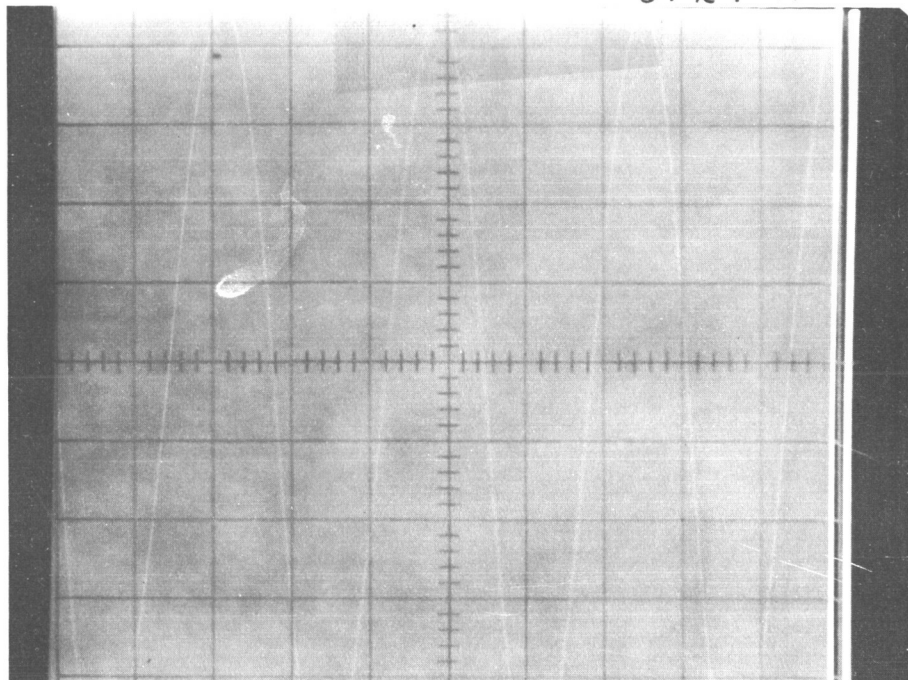


Figure IV-7d - Thermionic Scanner Work Function Map,  $T_E = 1210^\circ K$ ,  $T_{C_0} = 400^\circ K$

64-R-1-82

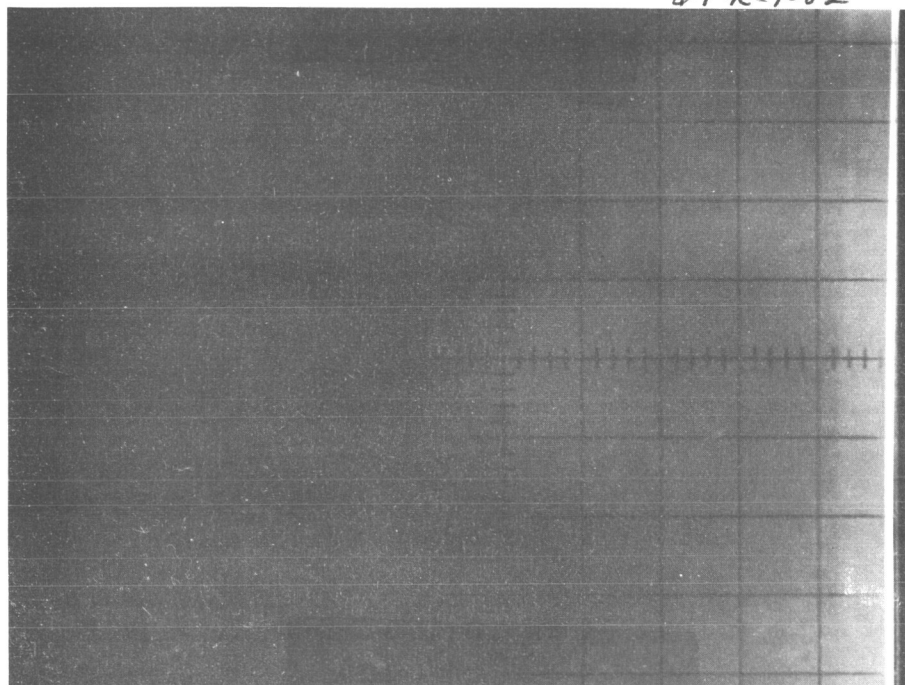


Figure IV-7e - Thermionic Scanner Work Function Map,  $T_E = 1210^\circ K$ ,  $T_{C_0} = 450^\circ K$

64-R-1-83

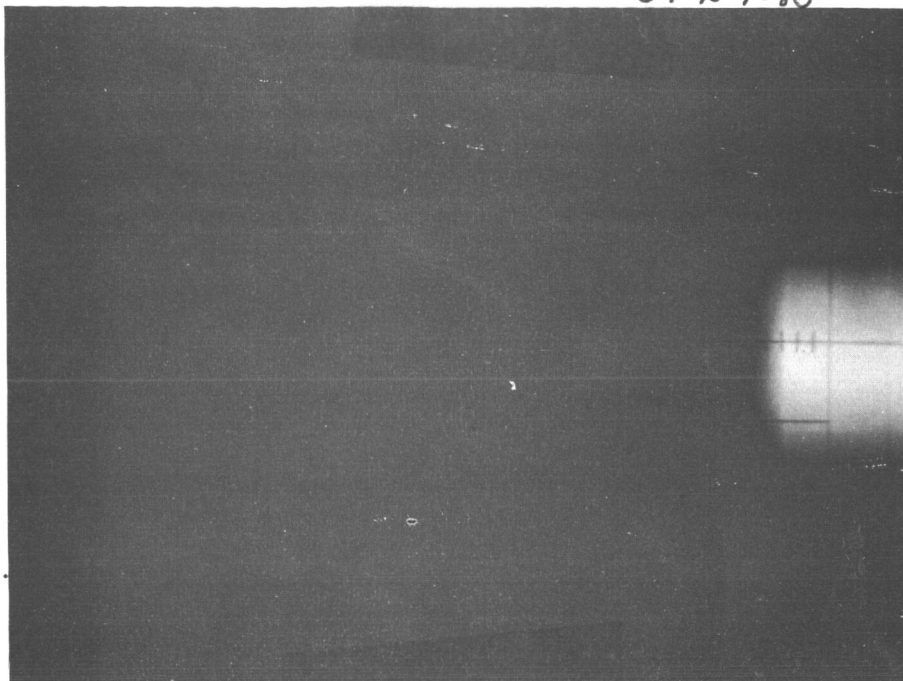


Figure IV-7f. Thermionic Scanner Work Function  
map,  $T_E = 1210^\circ K$ ,  $T_{C_0} = 420^\circ K$ ,  $CFC = 0$

64-R-1-84

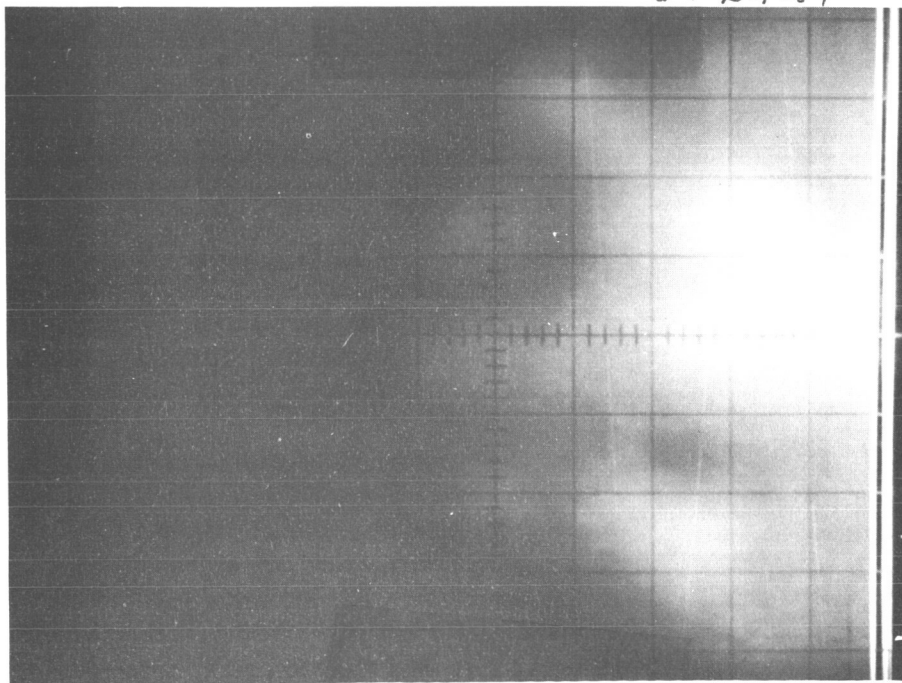


Figure IV-7g. Thermionic Scanner Work Function  
map,  $T_E = 1210^\circ K$ ,  $T_{C_0} = 420^\circ K$ ,  $CFC = 50$

64-R-1-85

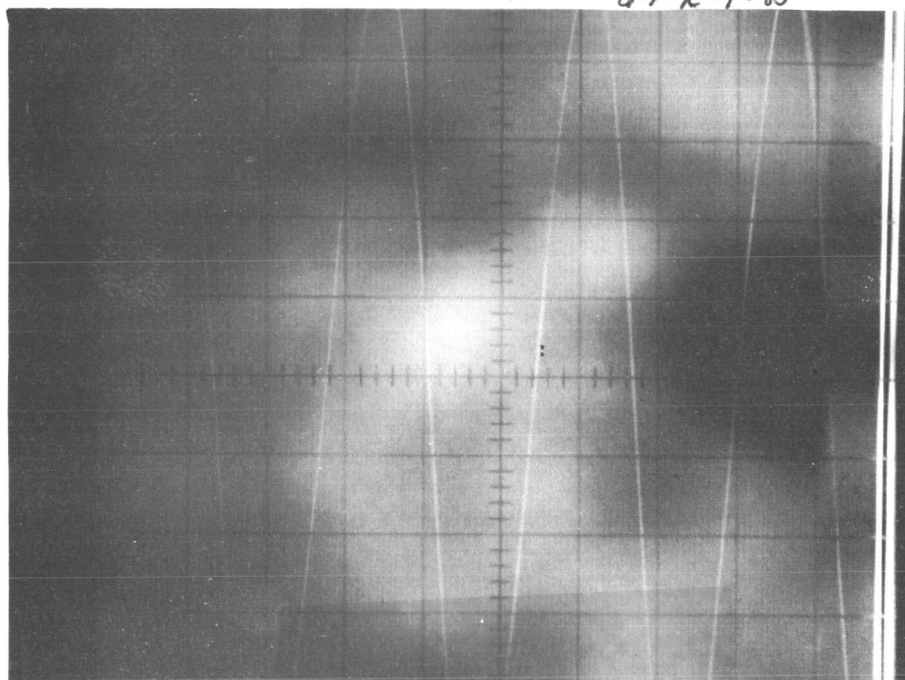


Figure IV-7h. Thermionic Scanner Work Function

Map,  $T_E = 1210^\circ\text{K}$ ,  $T_{C_3} = 420^\circ\text{K}$ , CFC = 150



64-R-1-86

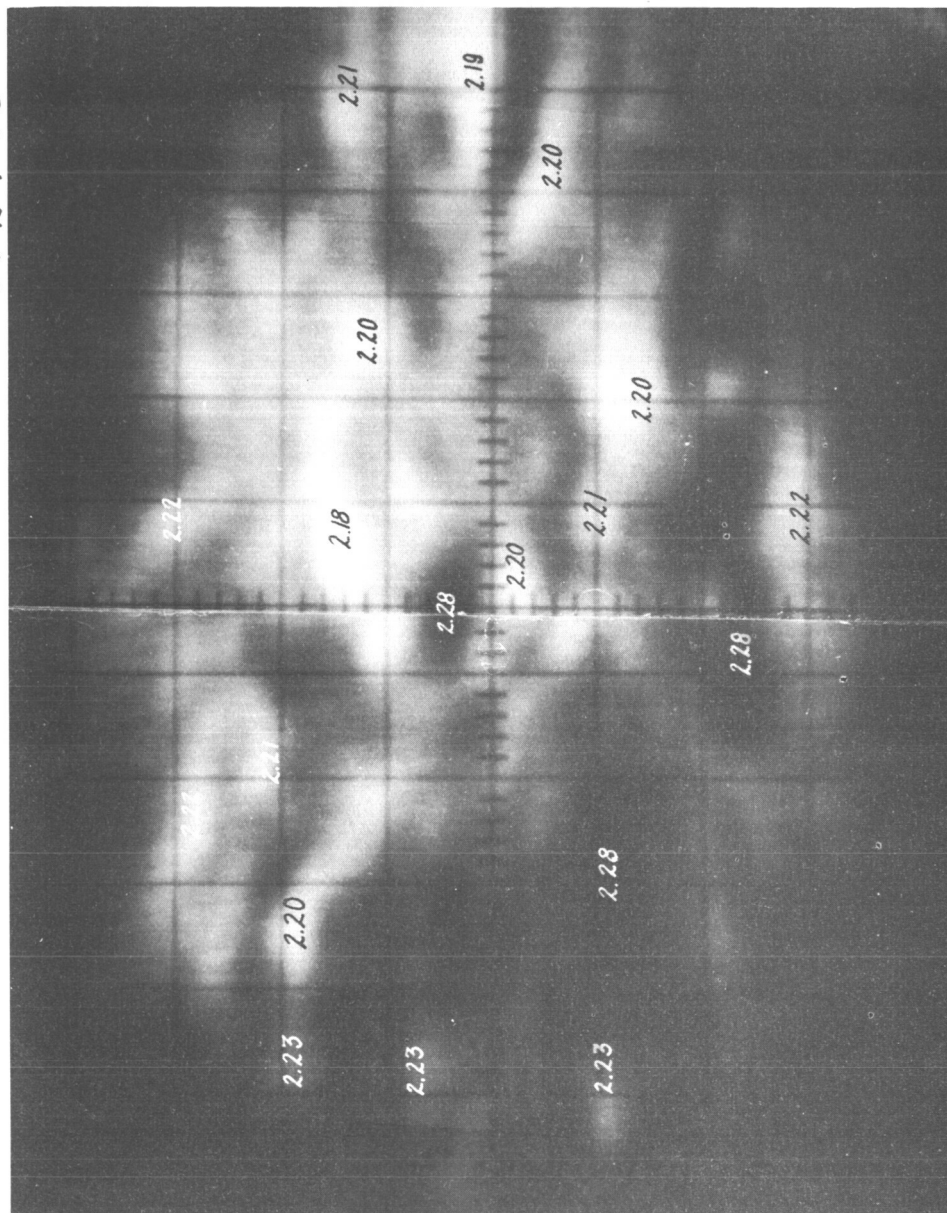
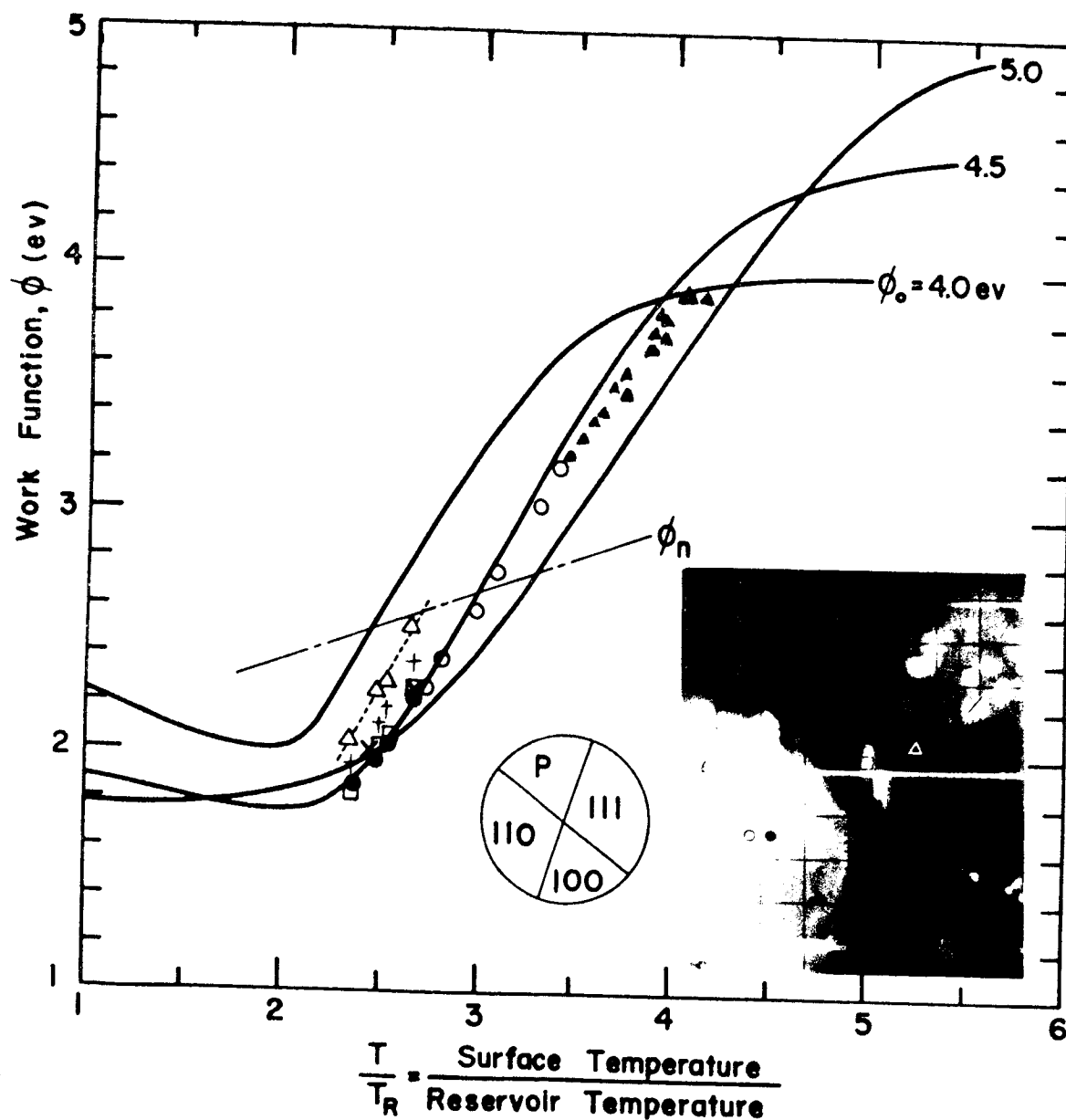


Figure IV-8 Work Function Map Showing Computed  
Values of Work Function from Cross Scan



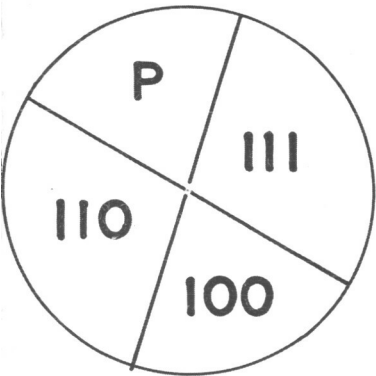
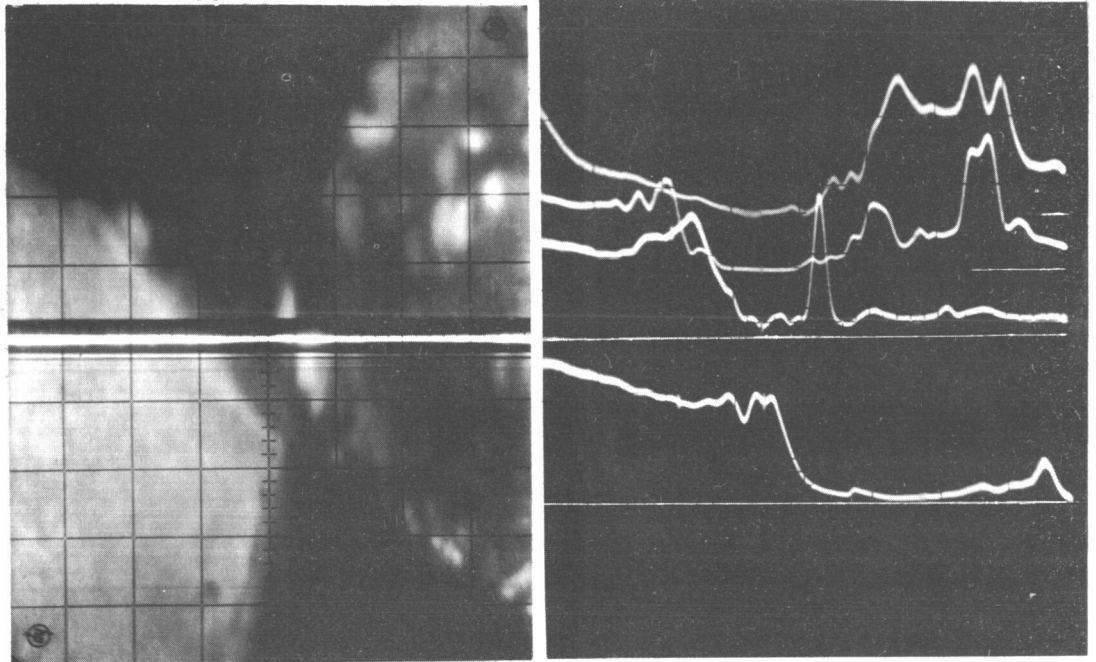


○ Scanner Results -  $\langle 110 \rangle$  Emitter Electro Polished  
 ▲ Converter Results -  $\langle 110 \rangle$  Emitter Electro Polished

Figure IV-9. Apparent Values of Work Function

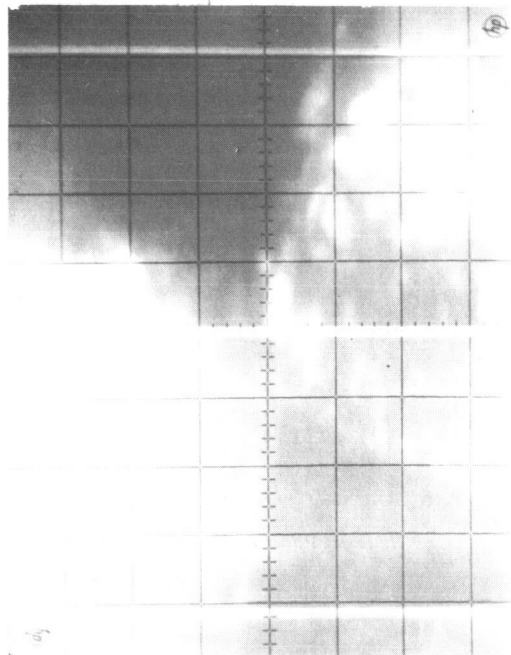
$$T/T_R = 2.5$$

64-R-1-88



$$T_R = 420^\circ\text{K}$$

$$T/T_R = 2.7$$



$$T/T_R = 2.35$$

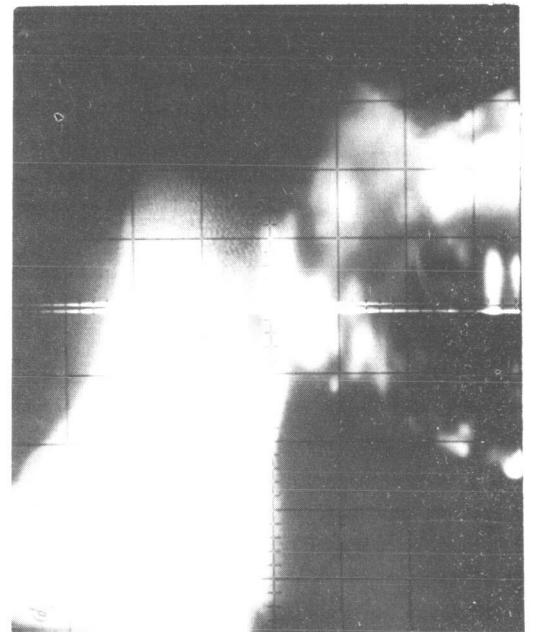
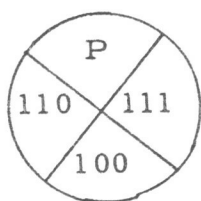
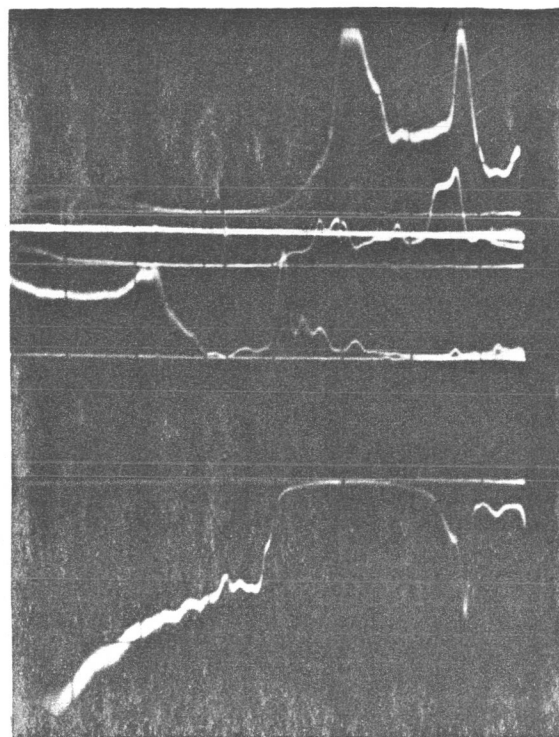
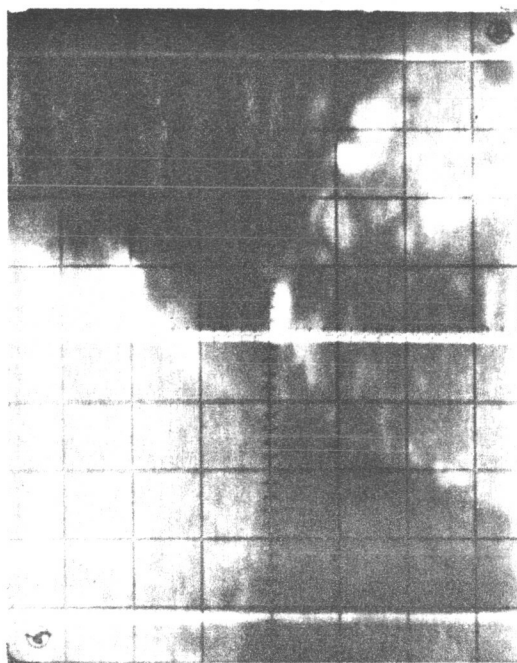


Figure IV-10 Work Function Map and Cross Scan for  
Thermionic Scanner, Composite Emitter

$$T/T_R = 2.67$$



$$T/T_R = 2.55$$

$$T_R = 420^\circ\text{K}$$

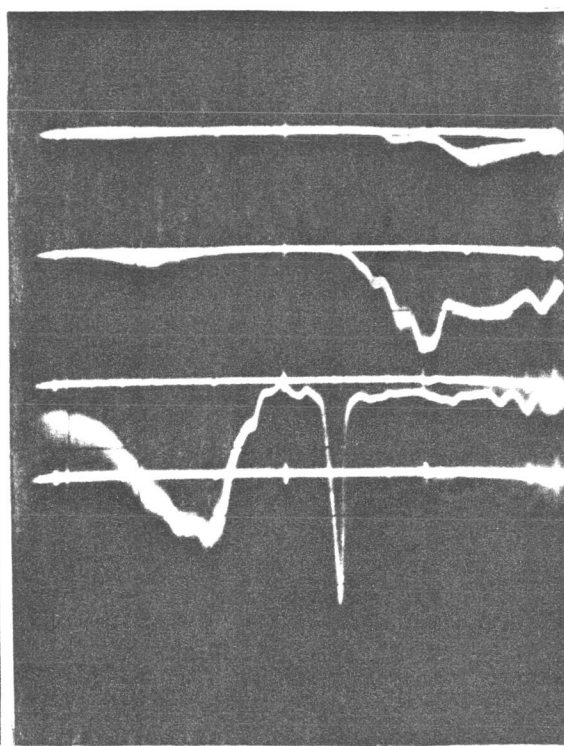
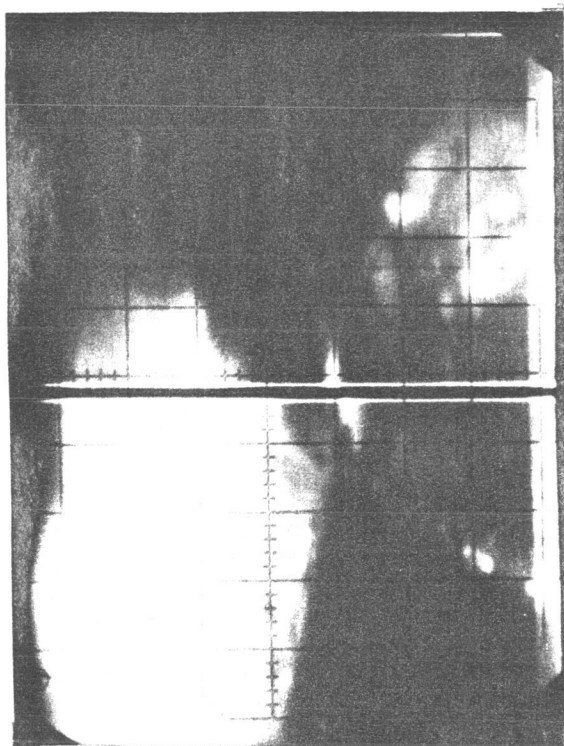
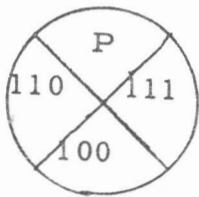
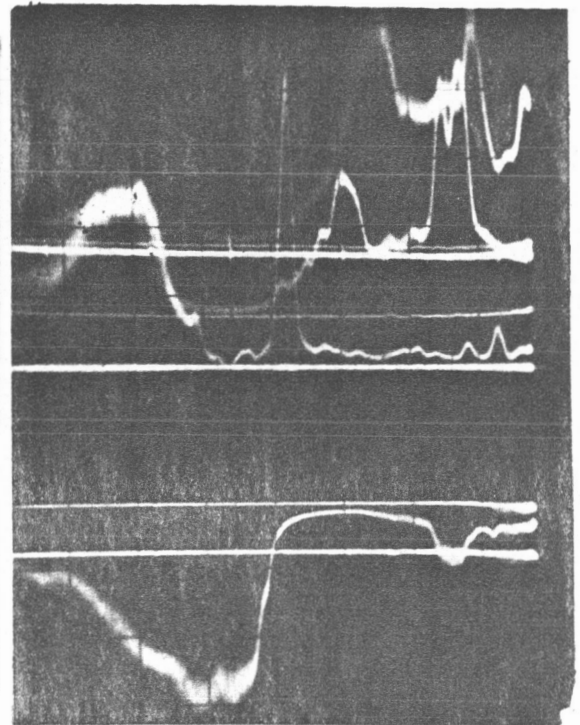
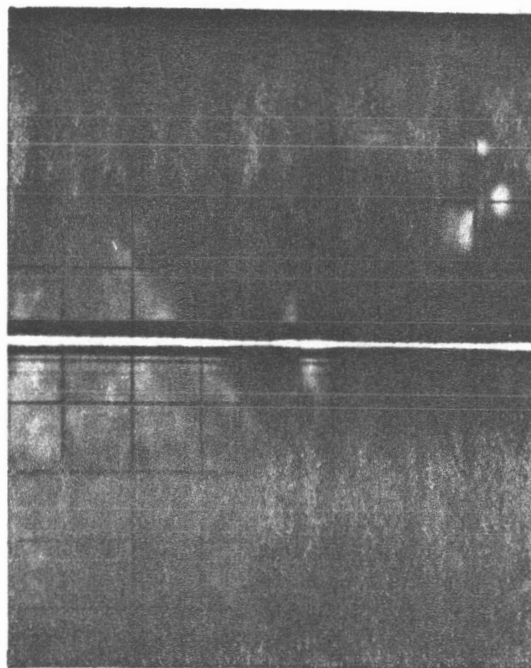


Figure IV-11. Work Function Map and Cross Scan For Thermionic Scanner. Composite Emitter

$$T/T_R = 2.49$$

64-R-1-90



$$T/T_R = 2.37$$

$$T_R = 420^\circ \text{K}$$

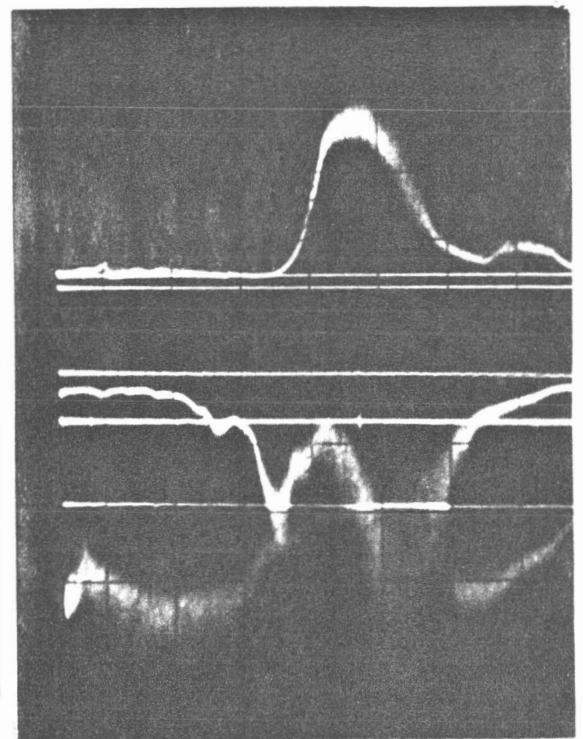


Figure IV-12. Work Function Map and Cross Scan For  
Thermionic Scanner. Composite Emitter

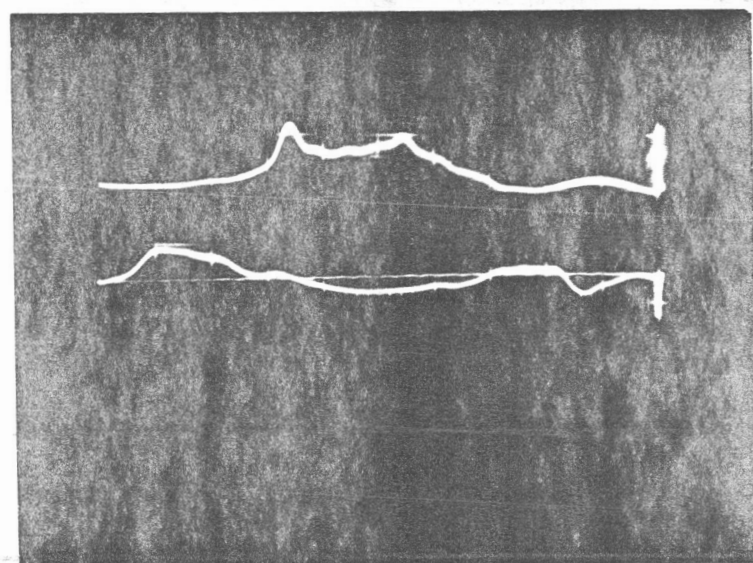
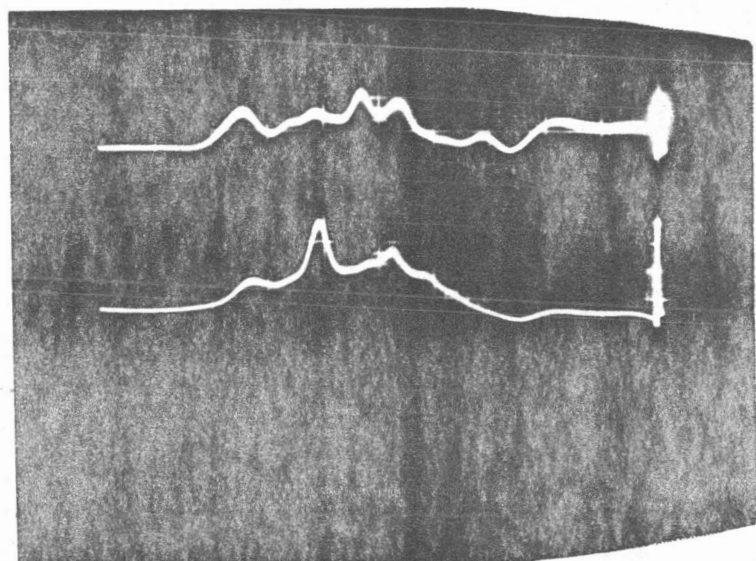
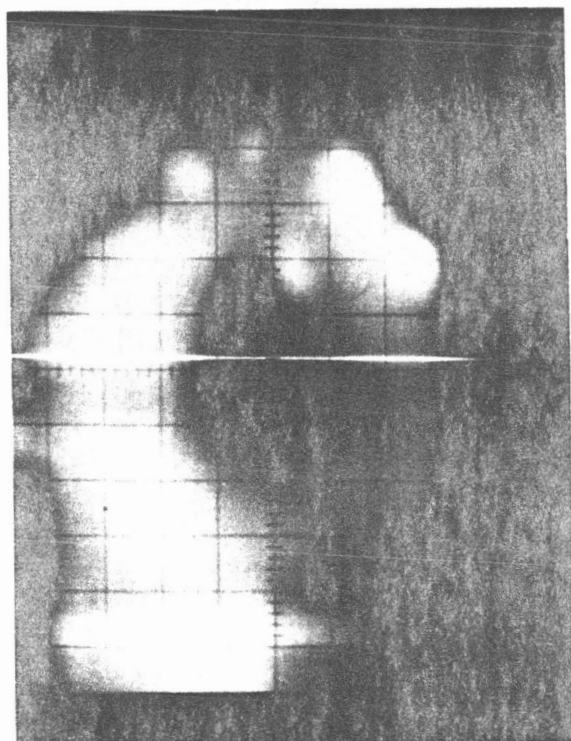


Figure IV-13. Work Function Map and Cross Scan for Thermionic Scanner. Single Crystal  $\langle 110 \rangle$  Tungsten Emitter.



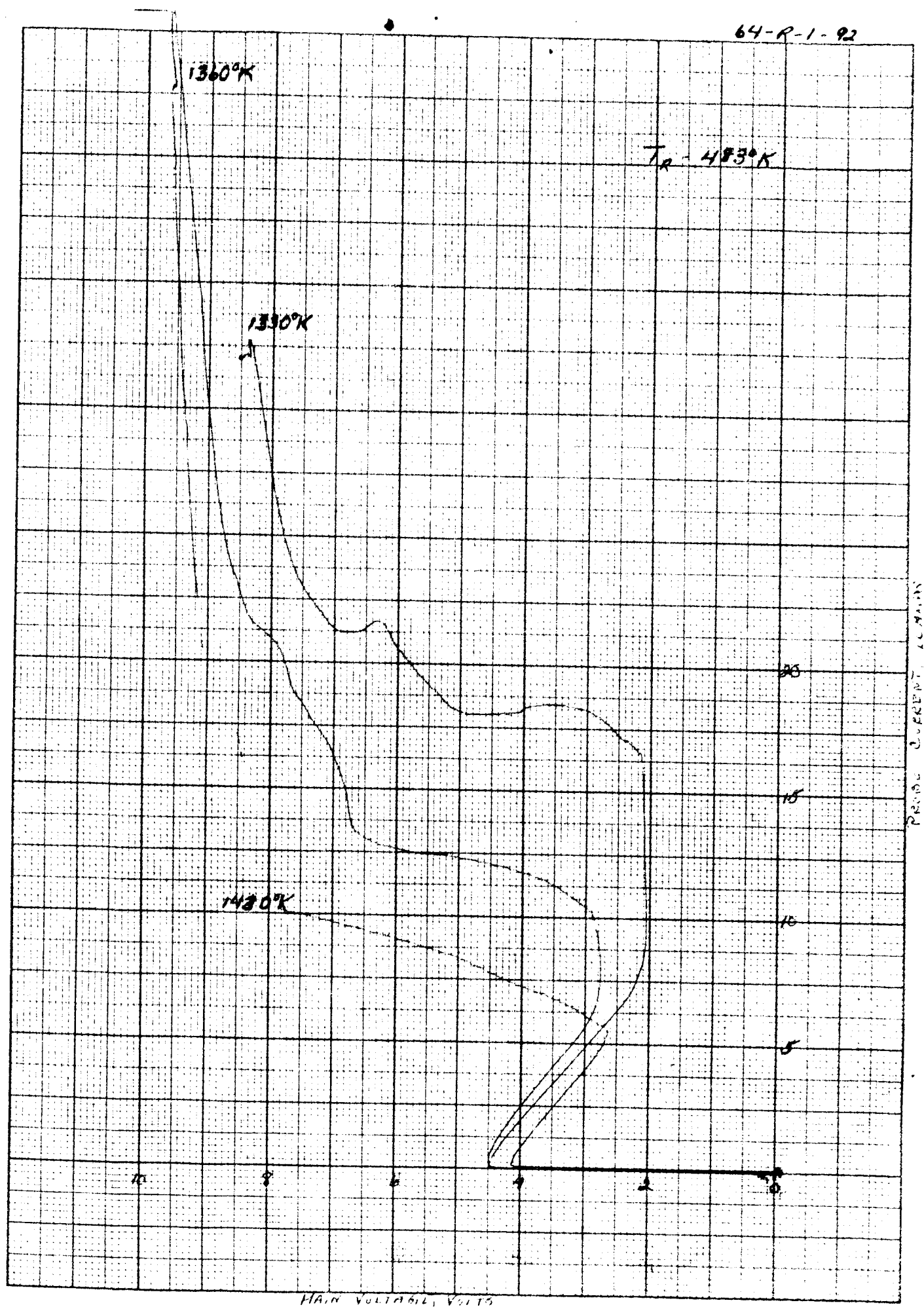


FIG. 12-14a PROBE CURRENT CHARACTERISTICS

64-R-1-93

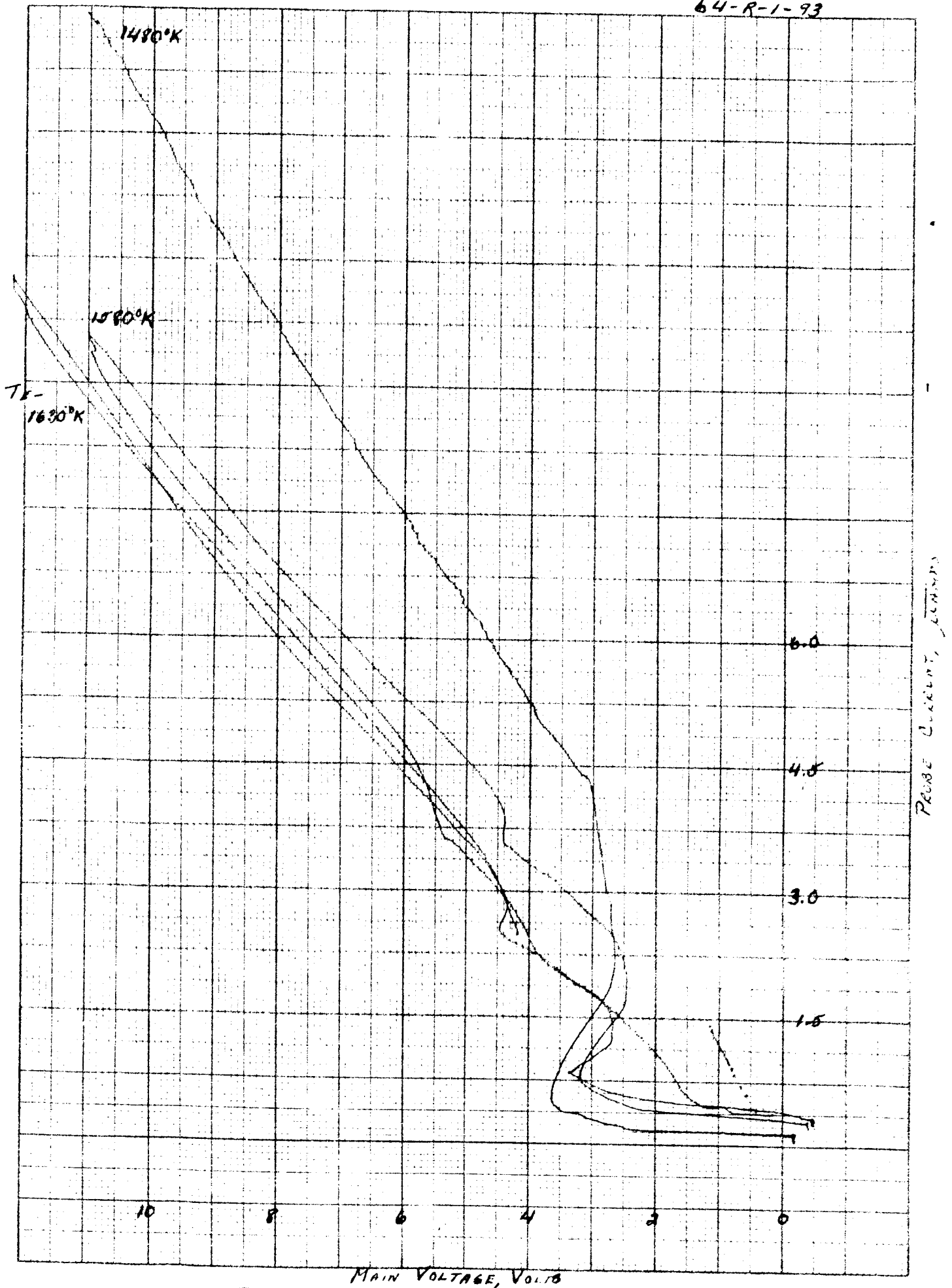


Fig. II-14b PROBE CURRENT CHARACTERISTICS



## CHAPTER V

### CONVERTER STUDIES

#### A. GENERAL

The fundamental purpose of the scanning experiments and of the metallurgical work is the determination of correlations between theory, surface preparation techniques, covered work function and converter performance. The converter performance may, therefore, be considered the acid test of all that has gone before.

This chapter describes two types of converter tests. In one type the average covered-surface work function was determined in the converter and compared with the point-by-point values obtained in the scanner. The correlation is found to be excellent. The converter performance was then determined, and it was shown that surfaces with the same measured value of covered work function give the same performance. Thus the consistency of the results obtained from the various experiments performed under this program has been clearly established.

#### B. THE TEST VEHICLE

The type of test vehicle used in this program has been extensively employed at Thermo Electron for research work in the past. The electrodes are of plane parallel geometry, and the design allows considerable variation of the important parameters. The fact that the emitters had to be scanned prior to their use in the converter dictated a change in the emitter assembly. Other than that, the design was not altered. Figure V-1 is a cross-sectional view of the test vehicle and its supporting structure. The emitter (1) is a flat disc,  $3 \text{ cm}^2$  in area, composed of a tungsten face brazed on a tantalum backing. On the backside of





this emitter sandwich a cavity (7) is located and serves as the point in which the emitter temperature is measured with an optical pyrometer. The emitter is supported by a thin tantalum tube (2) which also serves as the electrical connection to the emitter. The other end of this tube is joined to the emitter support (3). A radiator (4) helps dissipate the heat conducted by the tantalum sleeve supporting the emitter. Part No. 5 is a flange joining the emitter assembly to the collector assembly and retains the getter (6). Parts Nos. 1 through 7 constitute the emitter assembly which is common to the scanning devices and the converters used in this program. The molybdenum collector (8) is joined to the seal assembly (9) and the collector support (12). The envelope of the converter is completed by part No. 11, which is welded to the emitter flange (5). The two flexible flanges of this seal allow part No. 11 to move with respect to the collector (8), and thus the spacing between emitter and collector can be fixed by adjusting the relative position of parts Nos. 11 and 8. Part No. 12 is attached to a heating coil (13) which is joined by three copper legs (14) to a water cooling coil (15). The amount of heat injected by the heating coil determines the temperature of the collector face, since this temperature is a function of the balance of the heat injected by the heater and removed by the water-cooling coil. A copper tube (16) joins the cesium reservoir (17) to the main converter. The temperature of the cesium reservoir is also determined by a balance between the heat injected by a resistance heater (18) and removed by a cooling strap (19). This method of temperature control allows the cesium reservoir and collector temperatures to be varied over wide limits.

### C. INSTRUMENTATION

All performance data was obtained by dynamic testing; that is, the output characteristic of the converter was traced at 60 cycles and recorded at a slower



rate. Figure V-2 is a schematic diagram of the instrumentation used for this purpose. Basically, the function of this circuit is to apply a 60-cycle alternating voltage to the converter terminals. This is done by the variable transformers A and B, which are connected through isolation transformers (A and B) in series across the converter terminals. A shunt ( $R_2$ ) is provided for the measurement of the currents circulated.

The reason for the use of two variable transformers, as well as the various diodes shown in the circuit, becomes apparent once the problem of tracing a converter characteristic is discussed. Figure V-4 is a typical converter characteristic. A loadline determined by the shunt resistance and the resistance of the leads of the circuit is also shown on this same figure. The intercept of this loadline and the converter characteristic will determine the voltage at the converter terminals when no external source of voltage is incorporated in the circuit. In other words, this is the voltage which would be measured if the converter is operating and no power is supplied to the variable transformers shown in Figure V-2. The use of the two variable transformers allows tracing any portion of the converter characteristic to the left or to the right of this zero-voltage point. How this is accomplished can be described by referring to Figure V-3, which plots the voltage generated across points 1 and 2 of Figure V-2 against time.  $V_A$  is the voltage generated by variable transformer A. It is a half-wave rectified ac voltage. The voltage generated by variable transformer B is a continuous ac voltage of a much smaller amplitude. The sum of the two voltages is shown as  $V_{A+B}$  in Figure V-3. The zero in Figure V-3 corresponds to the 0 voltage shown in Figure V-4. Now, depending on the setting of the two variable transformers, the region of the current-voltage curve traced to the left or to the right of the "0" position can be increased or decreased. The current is measured across shunt  $R_2$ . The voltage is measured



directly by voltage taps located on the converter itself. These two signals are fed into a sampler, the function of which is to scan the repetitive trace of the characteristic of the converter at a rate much slower than the 60 cycles. The output of this sampler is fed to an X-Y plotter that produces a permanent record of the characteristic of the converter.

#### D. PERFORMANCE TESTING

All converter performance data were obtained in the form of families of current-voltage curves. Such a family is shown in Figure V-5. It is obtained by setting the emitter temperature, the collector temperature, and spacing at a fixed value. The cesium reservoir temperature is varied, and individual current-voltage curves are recorded at  $10^\circ$  intervals of cesium reservoir temperature variation. It will be noted that any two individual current-voltage curves cross each other at a certain voltage. Moreover, for any given voltage, the maximum current is exhibited by one particular I-V curve. This behavior makes it possible to define the locus of maximum performance for this family of current-voltage curves, which is a curve tangent to each current-voltage curve contained in the family and is shown as a dotted line in Figure V-5. This envelope is the least ambiguous quantity that can be used in comparing performance among different converters and for the same converters at different times. It is far better than comparing individual voltage curves, since their shape is extremely sensitive to cesium reservoir temperatures, and an error of a few degrees can completely change the character of the current-voltage curve. Throughout the program envelopes have been used for comparing the data from different converters as well as checking the reproducibility of the same converter.

Four converters were built and tested in this program. The first converter which was extensively tested used a polycrystalline tungsten emitter which had



been treated in such a way as to assure that it had reached a stable terminal condition. The process as well as the means of determining that it has reached such a condition are described in Chapter VI. This converter was tested extensively in a parametric sense, and the results are shown in Figures V-6 through V-30. The data is presented in the form of families of current-voltage curves taken at four different emitter temperatures and seven spacing settings with the cesium pressure varying over the range of interest for power production. The performance throughout the range is considerably superior to the performance of the polycrystalline tungsten emitter recorded in an earlier program at Thermo Electron.\* The previous polycrystalline emitter had undergone no special treatment other than outgassing prior to the performance mapping.

Of the remaining three converters built in the program, one employed a polycrystalline emitter and two single-crystal emitters. Those converters were used primarily for work function measurement, and their performance was documented to a minor degree. However, it was checked at a sufficient number of sets of conditions so that any difference between their performance and the performance of the first converter would be detected. The performance of all devices was the same within experimental error.

Figures V-6 to V-30 provide accurate documentation of the performance of tungsten emitters over the emitter temperature range covered. However, because of the large amount of information contained, it is difficult to recognize trends in the data when presented in this form. To facilitate referring to these data for both analytical and hardware design purposes, the optimum performance of the emitter has been summarized in the following manner.

---

\* Annual Technical Summary Report for the Thermionic Emitter Materials Research Program (1 July 1961 through 30 June 1962), Contract NONR-3563(00), by S. S. Kitrilakis, M. E. Meeker and N. S. Rasor, Thermo Electron Report No. 2-63, prepared for Office of Naval Research, Power Branch, Dept. of the Navy, Washington 25, D. C.



The envelopes of all the current-voltage families at a certain emitter temperature have been superimposed in one figure. Such a figure is shown for the  $T_E = 1850$  case in Figure V-31. It will be observed that these envelopes cross each other just as the individual current-voltage curves did within a given family. Moreover, envelopes at larger spacings exhibit higher currents for higher voltages, while the reverse is true for envelopes at smaller spacings. One exception to this behavior is the minimum-spacing envelope, which always exhibits maximum performance at voltages greater than a certain value. This is due to the fact that that portion of the envelope results from unignited mode data. Since this mode, in the region of the operation we are considering, is electron space charge limited, the closest spacings will result in the highest currents.

A curve can be drawn in Figure V-31 tangent to the envelopes corresponding to individual spacings. This curve is the locus of maximum performance once cesium pressure and spacing have been fully optimized. It represents the maximum obtainable performance for the particular emitter temperature. Such loci have been constructed for all the emitter temperatures tested and are shown in Figure V-32. This is the summary performance for the emitter over the corrected temperature range,  $1630^\circ \text{K}$  to  $1950^\circ \text{K}$ . The power corresponding to this current-voltage plot is shown in Figure V-33. This figure shows the maximum power at any given voltage for a fixed emitter temperature and it represents the best attainable. The power-versus-voltage curves in Figure V-33 have gone through the maximum for the two lower emitter temperatures, while the highest emitter temperatures show no maximum. The reason for this behavior becomes apparent upon inspection of Figure V-32. The current densities in this graph are limited to  $40 \text{ amperes per cm}^2$ , which is the maximum that the instrumentation will handle, corresponding to a total current of 120 amperes. At this current value the power curves have not reached a maximum for the  $1850^\circ$  and  $1950^\circ \text{K}$  cases.



Figures V-34, -35, and -36 are runs taken with the single-crystal tungsten emitter exposing the  $\langle 110 \rangle$  plane. Comparison of these runs to the corresponding runs of the polycrystalline emitter will reveal that the performance is quite similar. This behavior was exhibited throughout the range wherever such families were taken. A second polycrystalline tungsten emitter converter was performance-tested prior to the initiation of extensive work function measurements. The results are shown in Figures V-37 to V-41 and are found to coincide with the performance of the first polycrystalline tungsten converter documented in Figures V-6 to V-30.

#### E. WORK FUNCTION MEASUREMENTS

The scanning experiments discussed elsewhere in this report measure the work function of emitter surfaces on a point-by-point basis. Those results, however, have to be compared with performance data, and a relationship between the two has to be established before the scanning results can be of value to the analysis of the conversion process. This link between the scanning experiments and the converter performance is furnished by averaged work function measurements conducted in the converters themselves.

The experimental procedure used for the determination of emitter and collector work function is relatively simple, and consists of obtaining current-voltage curves in a region of operation where transport effects are minimized. In the absence of transport effects the saturation of the emitter can be clearly defined at low voltages, while at voltages near open circuit the shape of the current-voltage curve is determined by the collection barrier and therefore follows the Boltzmann curve. Figure V-42 is a typical current-voltage curve which can be used to determine both emitter and collector work function. This curve is obtained under conditions of ion richness at the emitter which is



confirmed by the fact that the saturation current rises exponentially as the cesium reservoir temperature is increased and follows the Rasor plots of work function versus  $T/T_R$ , i. e.

$$\left. \frac{\partial \ln J_S}{\partial T_R} \right|_{T_E} = C T_R.$$

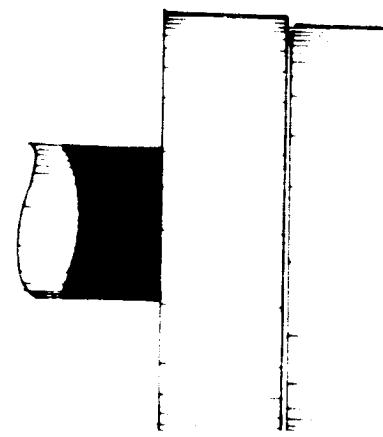
This means that the current is limited by the emitter work function, and no electron space charge barrier exists in front of the emitter. The emitter work function, then, can be determined by simply substituting the emitter temperature and the saturation current in the Richardson equation. This computation was performed on a number of current-voltage curves, and the results have been plotted in Figure V-44 in the form of work function versus the ratio of emitter temperature to reservoir temperature. The correlation appears to be quite good, and the bare work function line with which these results correlate is in the vicinity of 4.7 to 4.8 ev. The circles in Figure V-44 are points obtained from the polycrystalline tungsten emitter, and the triangles have been obtained from the single-crystal tungsten emitter. There appears to be no difference between the two, further confirming the result obtained in the performance tests where the output of the two devices was virtually identical. Further reference to these results has been made in the scanner section, where point-by-point measurements on emitter surfaces, both single-crystal and polycrystalline, have been correlated in a similar manner and are found to be in good agreement with these results.

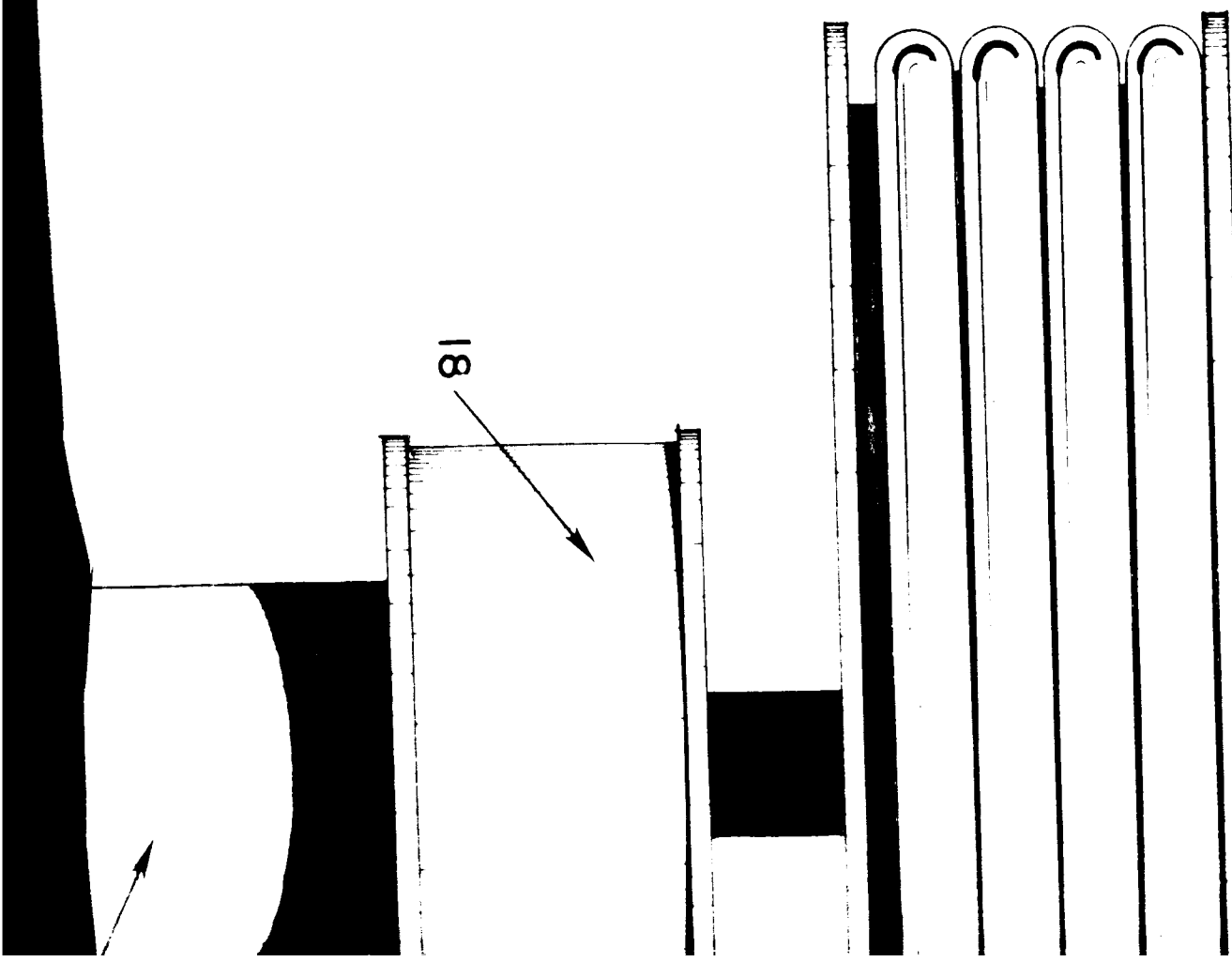
To determine collector work function, the following procedure has to be followed: Inspection of Figure V-42 shows that the current is dropping exponentially as the open-circuit voltage is approached. As the voltage is

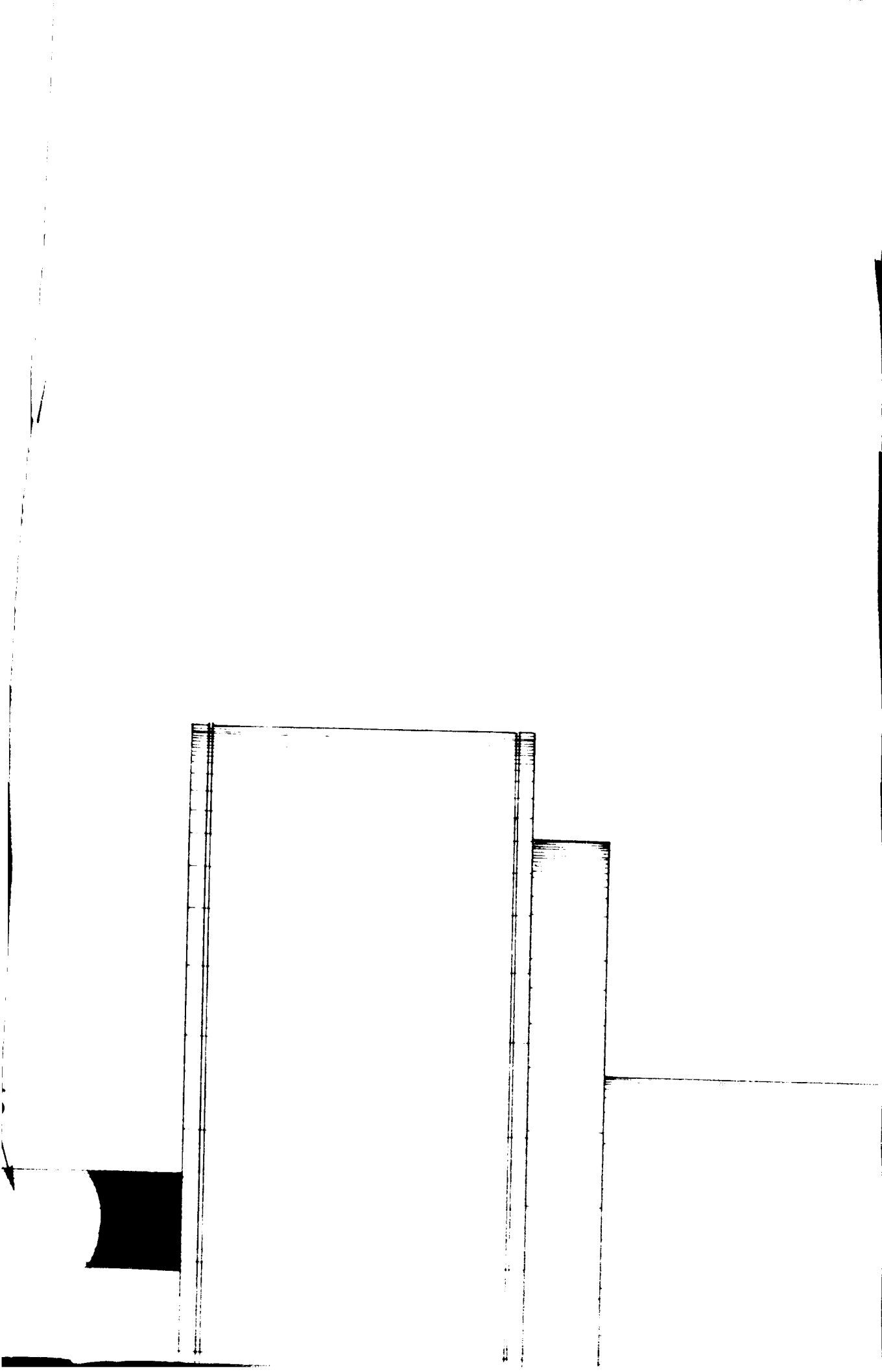


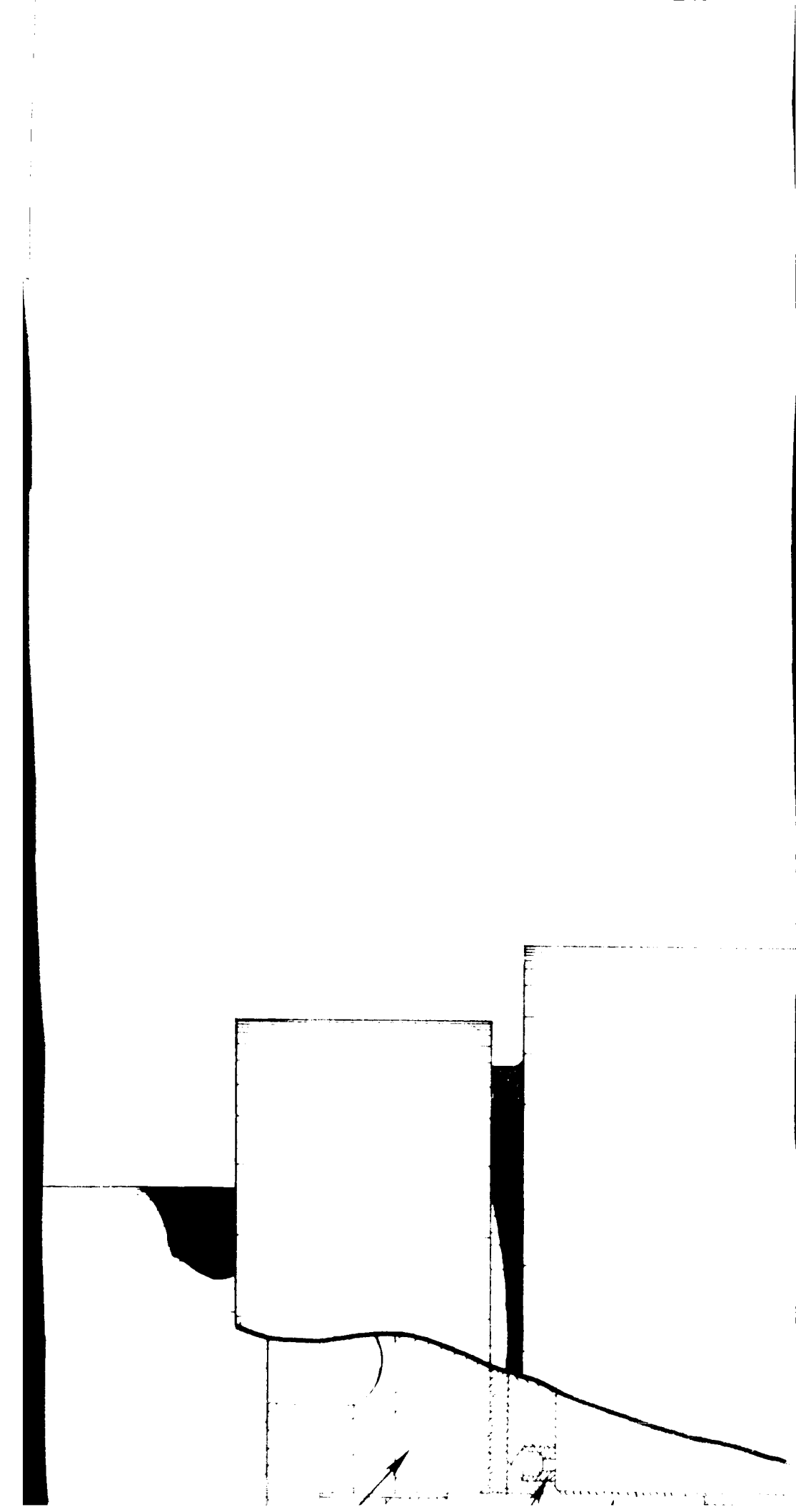
increased beyond the open-circuit voltage, the current reverses direction, and a saturation value is reached. This back current can be ion current, back emission from the collector, or leakage across the insulator separating emitter and collector. Whichever of these three possibilities may be the right one, the back current will in effect be subtracted from the forward current. A true measure, therefore, of the forward current will consist of the sum of the actual value of forward current plus the value of back current observed. This is accomplished by measuring current from the dotted line, which is the asymptote of the saturation value of the back current. This value of current can now be used to construct a logarithmic plot of current versus voltage, which is shown in Figure V-43. Figure V-43 approximates the idealized current-voltage characteristic in that it consists of two straight lines intersecting each other and exhibits a slight rounding off near the point of intersection. The horizontal line is indicative of the saturated emission, and the sloping line is the Boltzmann line associated with the emitter temperature and the barrier of collector work function plus output voltage. Any combination of current and voltage values along the Boltzmann line can be used to compute collector work function. To illustrate, at 1.65 v output voltage the output current density is  $15 \text{ ma/cm}^2$ . Substituting this current density value and the emitter temperature value of  $1725^\circ \text{K}$  in the Richardson equation, we find that the barrier limiting the current at that point is 3.55 ev. This barrier is composed of the collector work function and the output voltage. Subtracting the output voltage of 1.65 ev, we obtain the value of 1.9 ev for the collector work function. Figure V-45 is a plot of many such measurements against the ratio of collector temperature to cesium reservoir temperature.











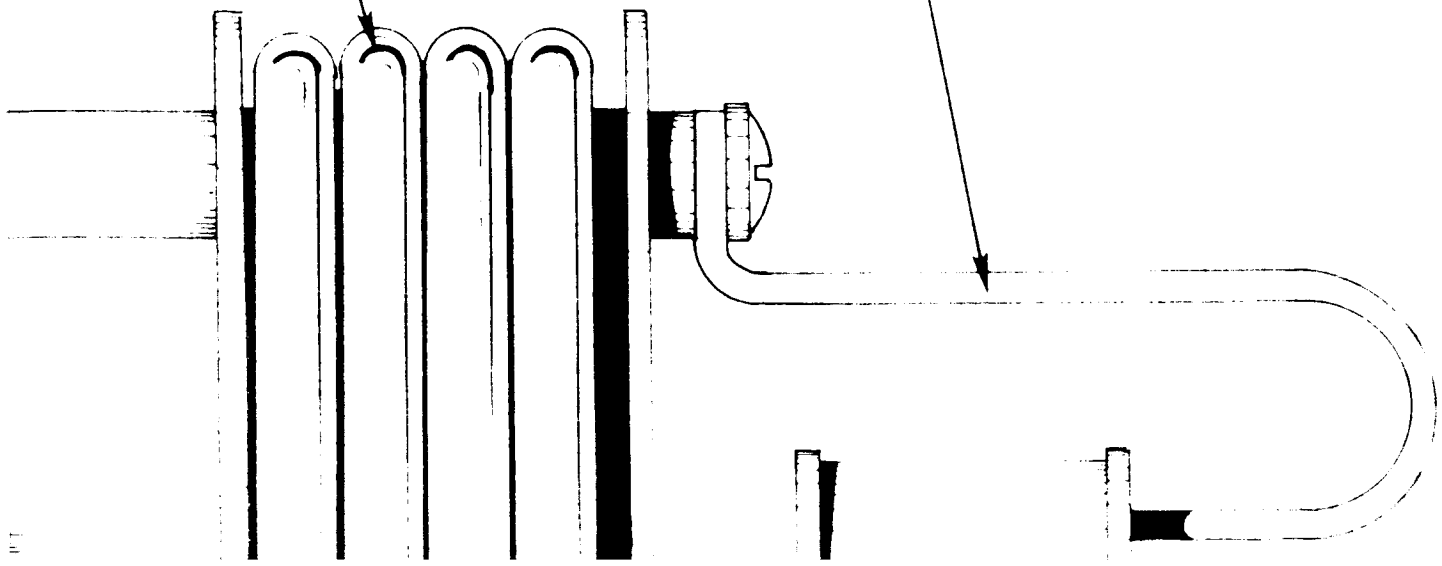


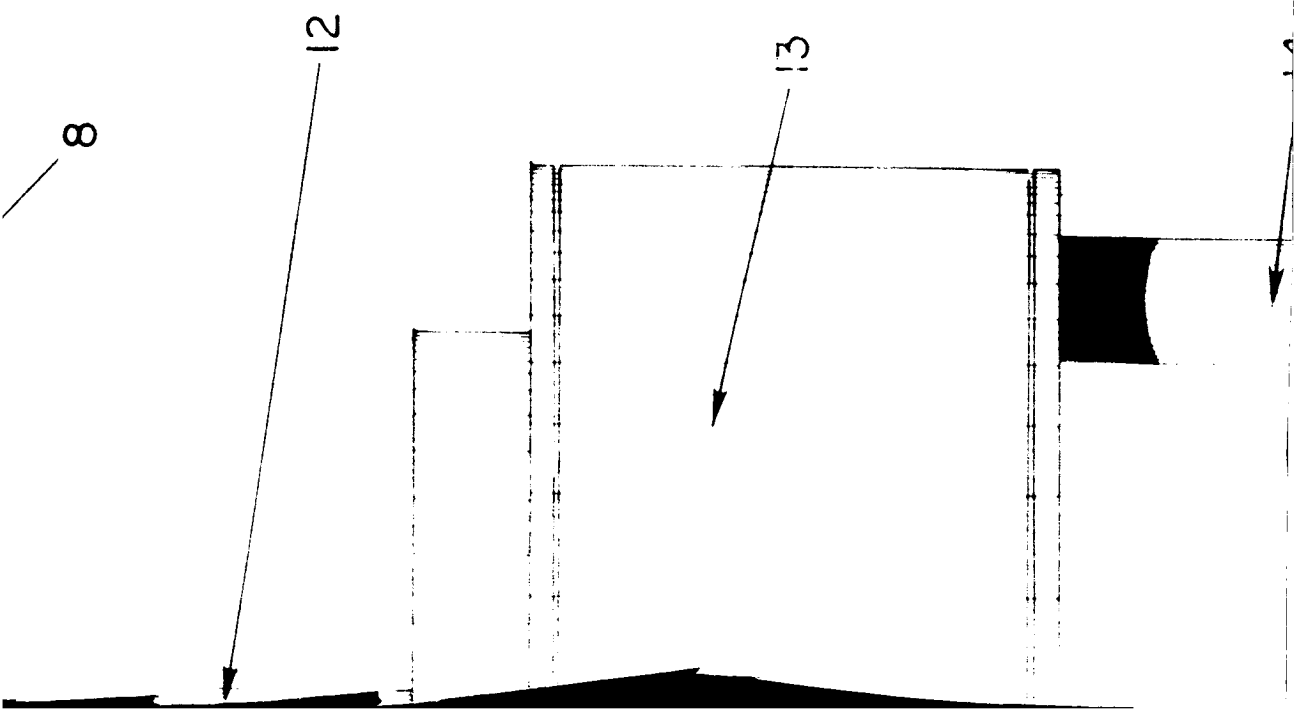


14

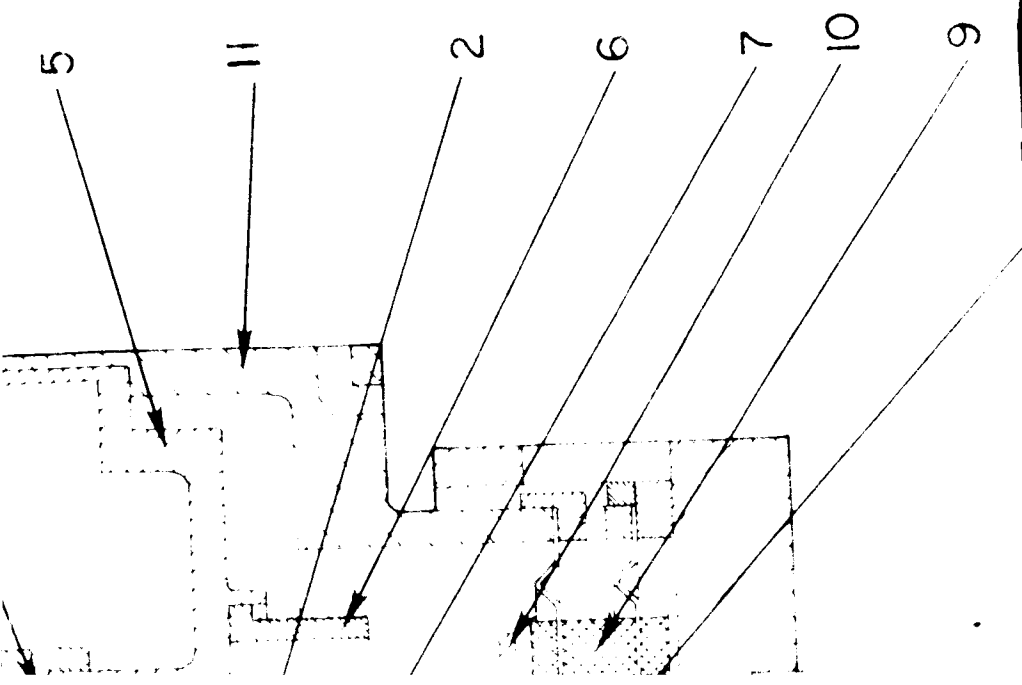
15

19









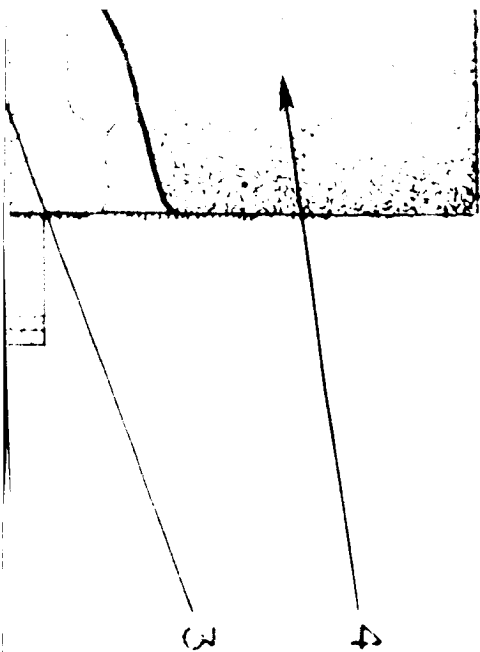


Figure V-1 Cross Section of  
Test Vehicle

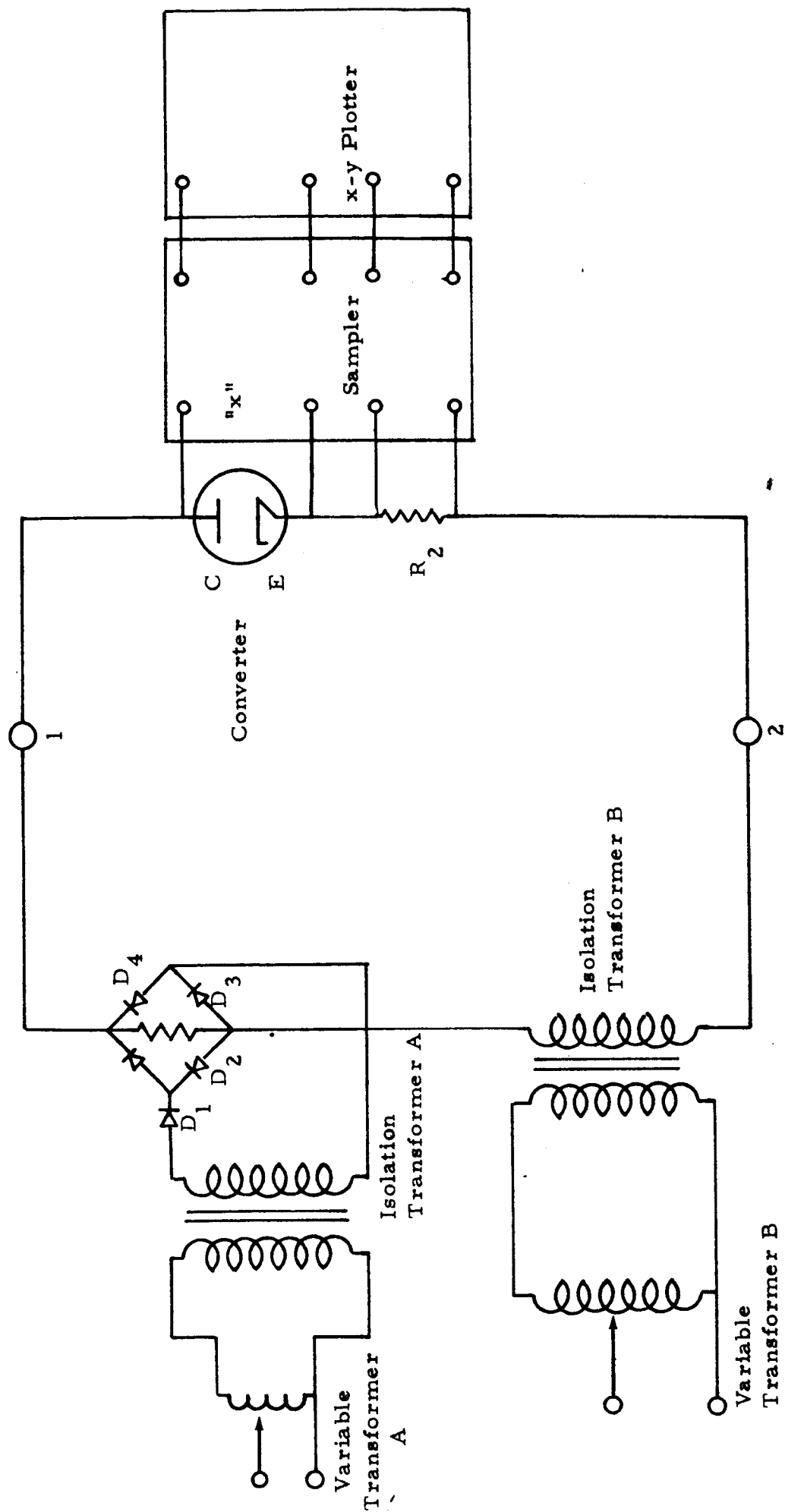


Figure V-2  
Dynamic Test Circuit Diagram

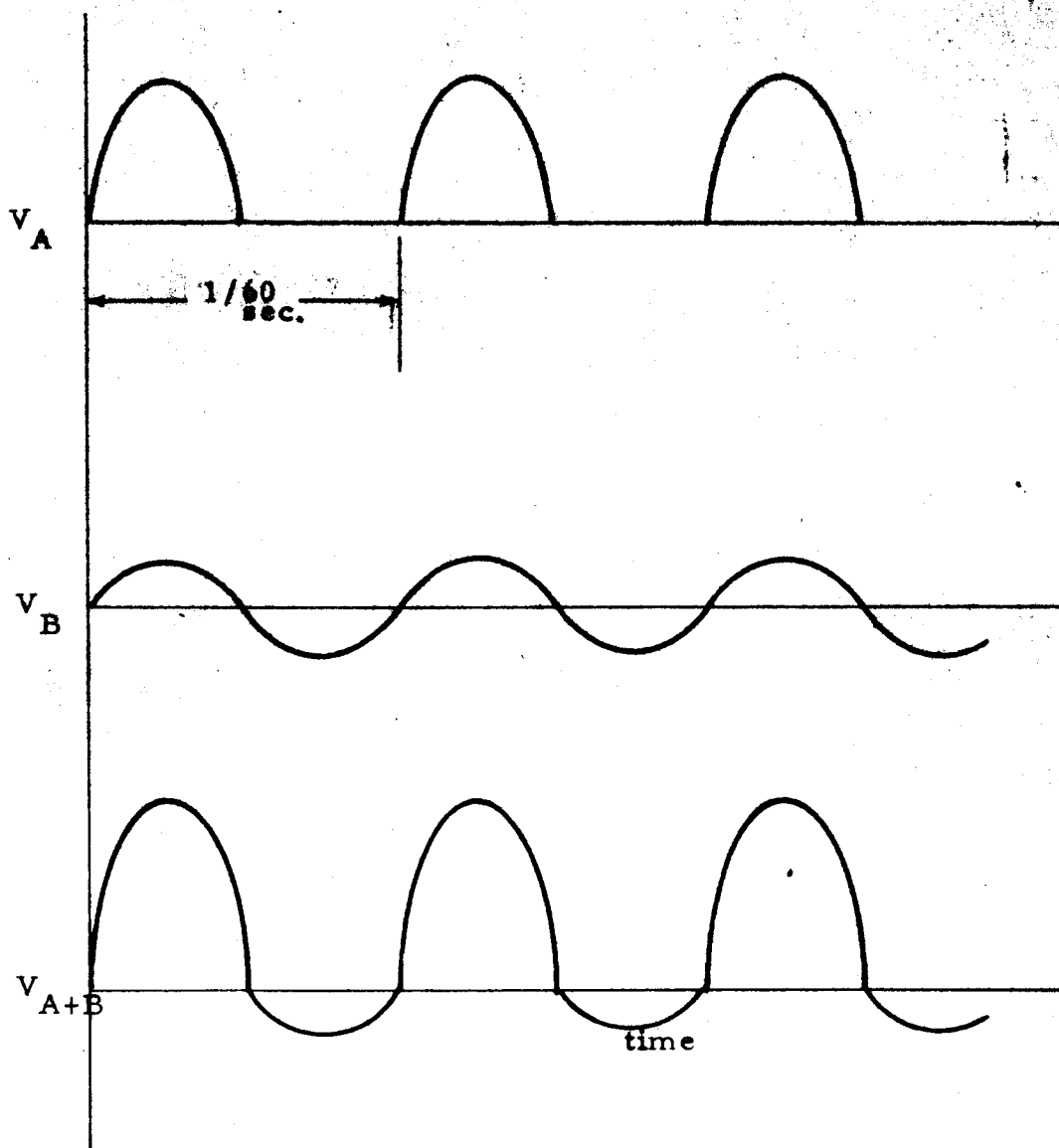


Figure V-3. Applied Voltage in Dynamic Testing

64-R-1-4

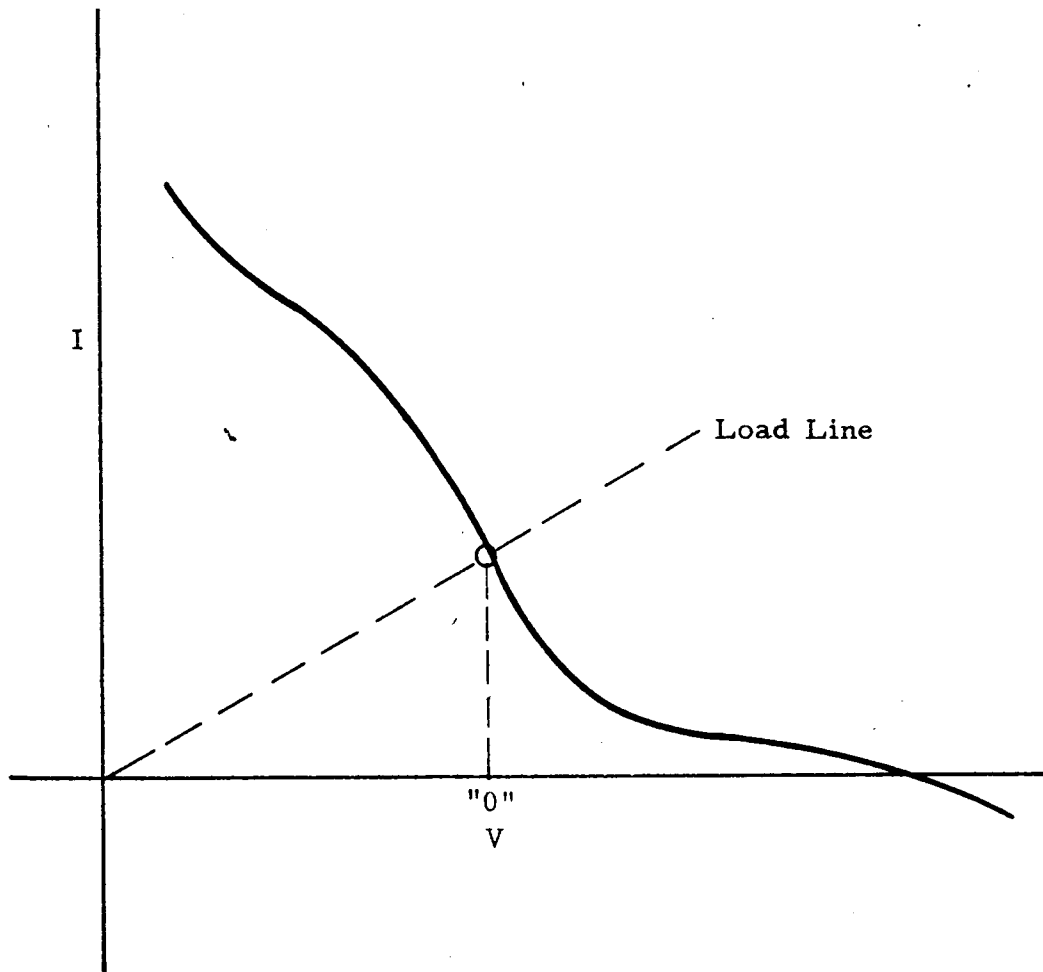
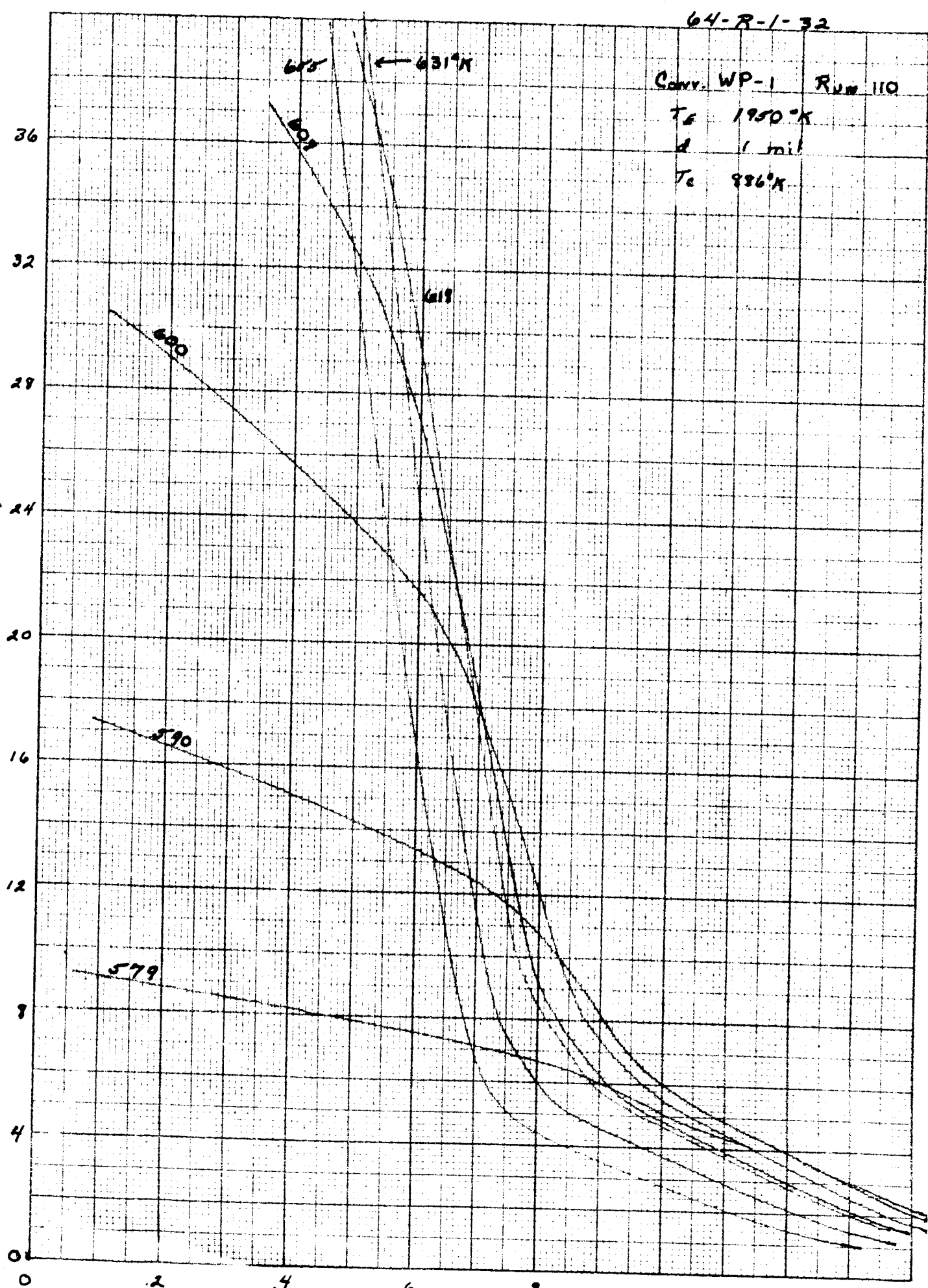


Figure V-4  
I-V Curve-Load-Line Intercept

CURRENT DENSITY, AMPS/CM<sup>2</sup>



OUTPUT VOLTAGE, VOLTS

FIG II-5. TYPICAL FAMILY OF I-V CURVES

64-R-1-33

Conv. WP-1 RvK 120

$T_e$  1640°K

$d$  min.

$T_c$  900°K

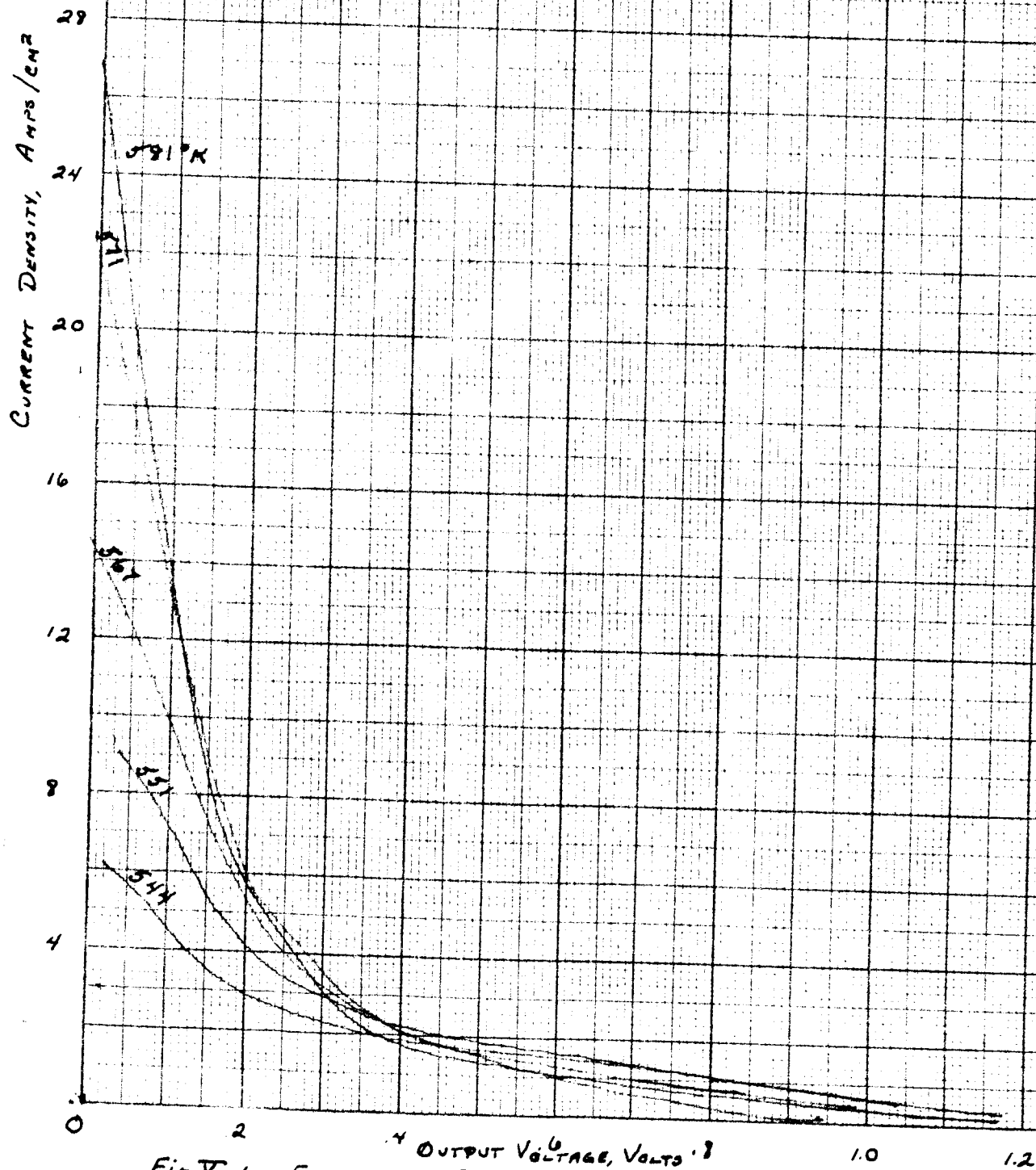


Fig. V-6. FAMILY OF I-V CURVES

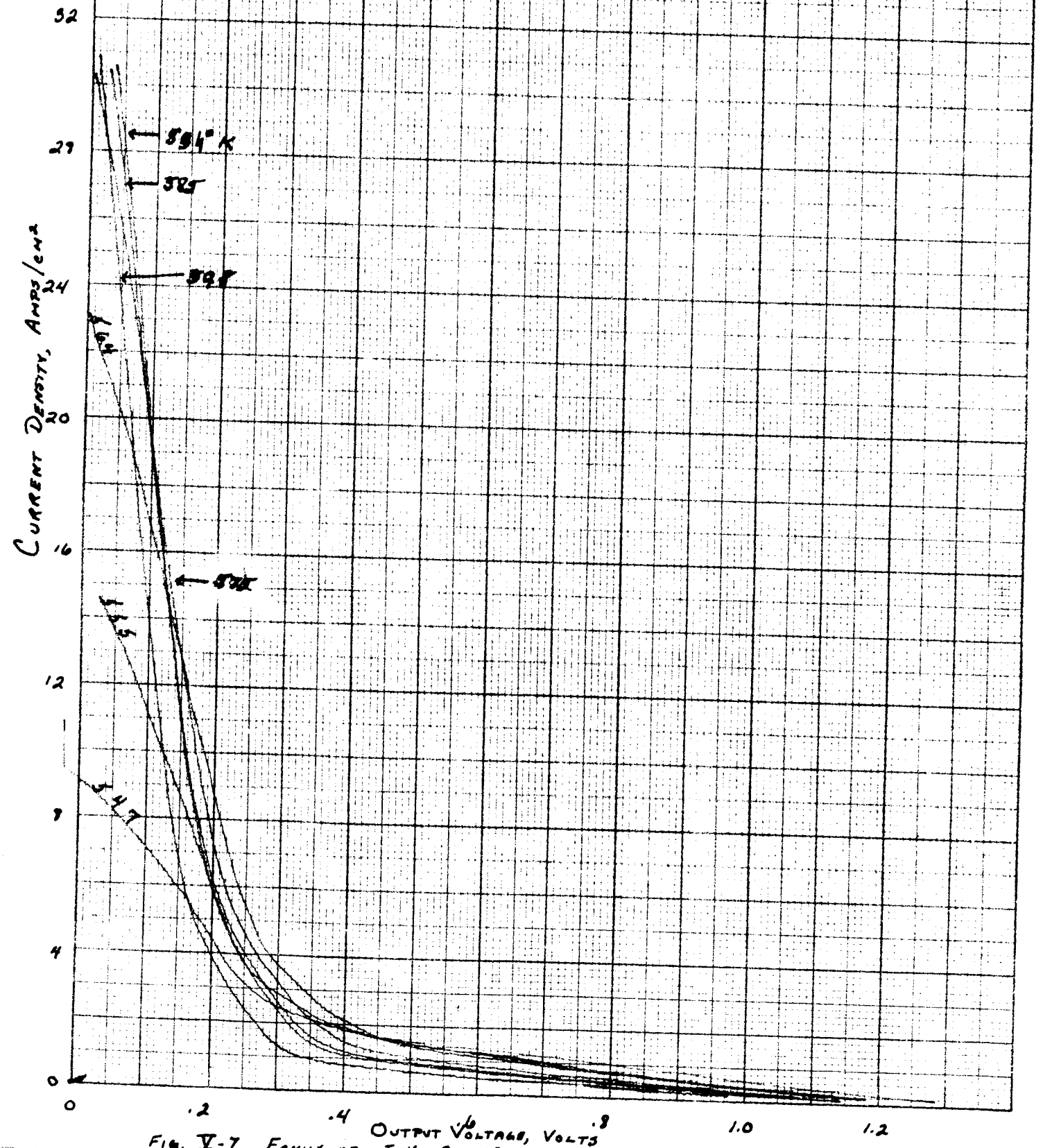
64-R-1-34

CONV. WP-1 RUN 121

$T_e$  1640°K

$d$  1 mil

$T_a$  313°K





64-R-1-25

Conn. WP-1 Run 122

$T_a$  1640°K

$d$  3 mil

$T_c$  902°K

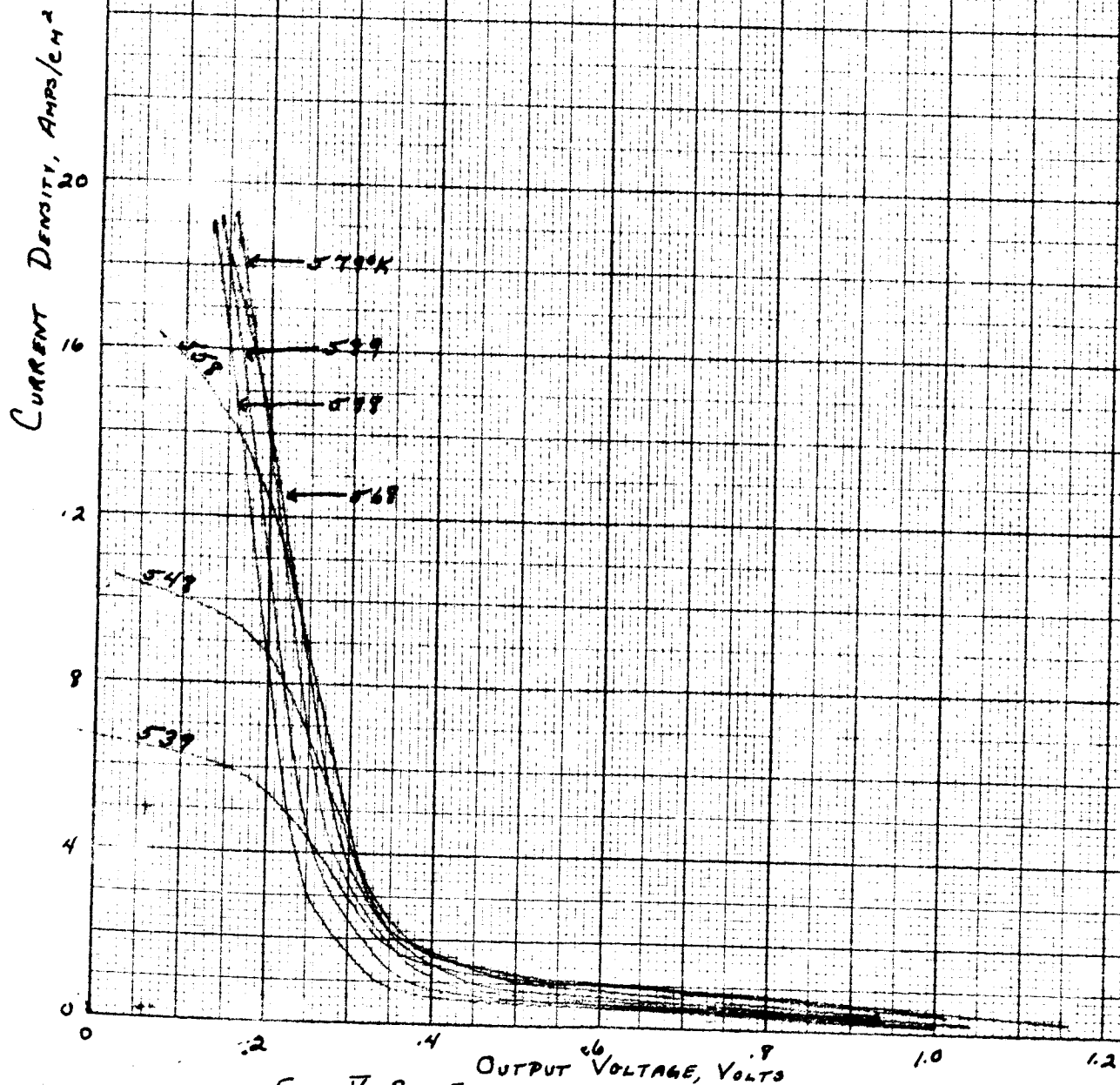


FIG. V-8. FAMILY OF I-V CURVES

64-R-1-36

Conv. WP-1 RUN 123

$T_a$  1640°K

$d$  6 mil

$T_c$  819°K

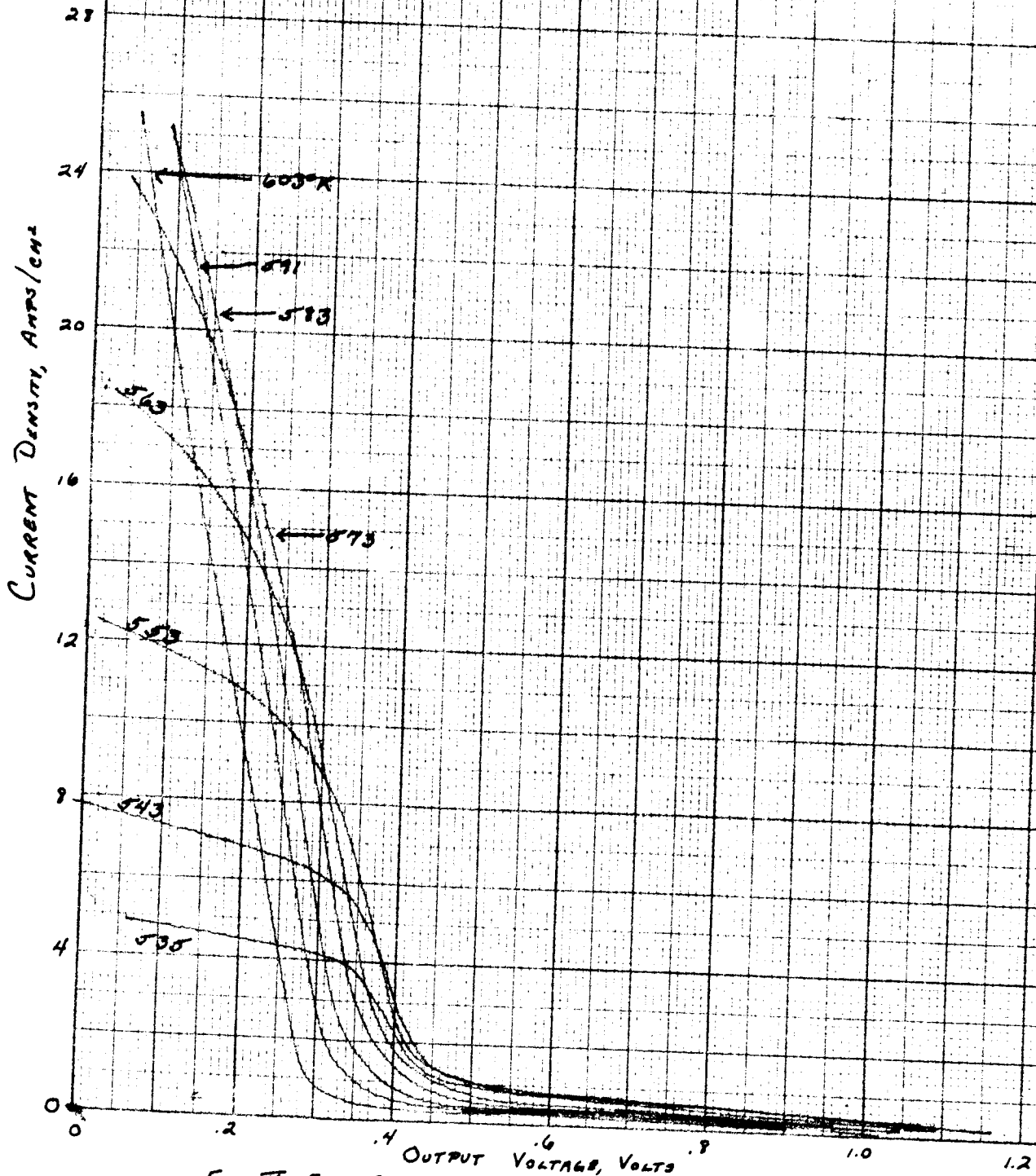


FIG. 5-9. FAMILY OF I-V CURVES

64-R-1-37

CONV. WP-1 RUN 124

$T_s$  1640°K

$d$  10 mil

$T_a$  785°K

CURRENT DENSITY, AMPS/CM<sup>2</sup>

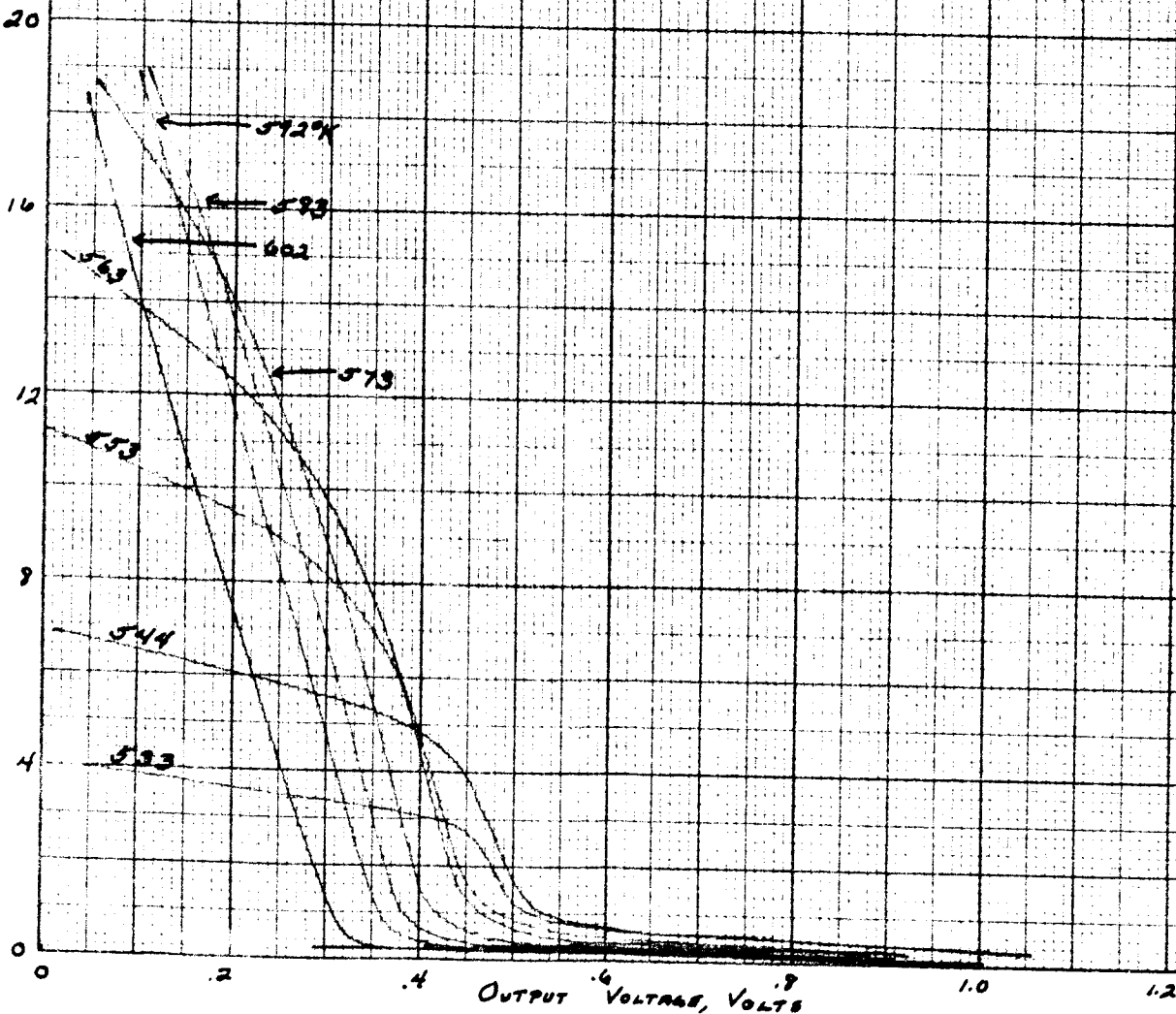


FIG. I-10 FAMILY OF I-V CURVES

64-R-1-38

CONV. WP-1 Rev 125

$T_c$  1640°K

$d$  15 mil

$T_a$  780°K

Current Density, Amps/cm<sup>2</sup>

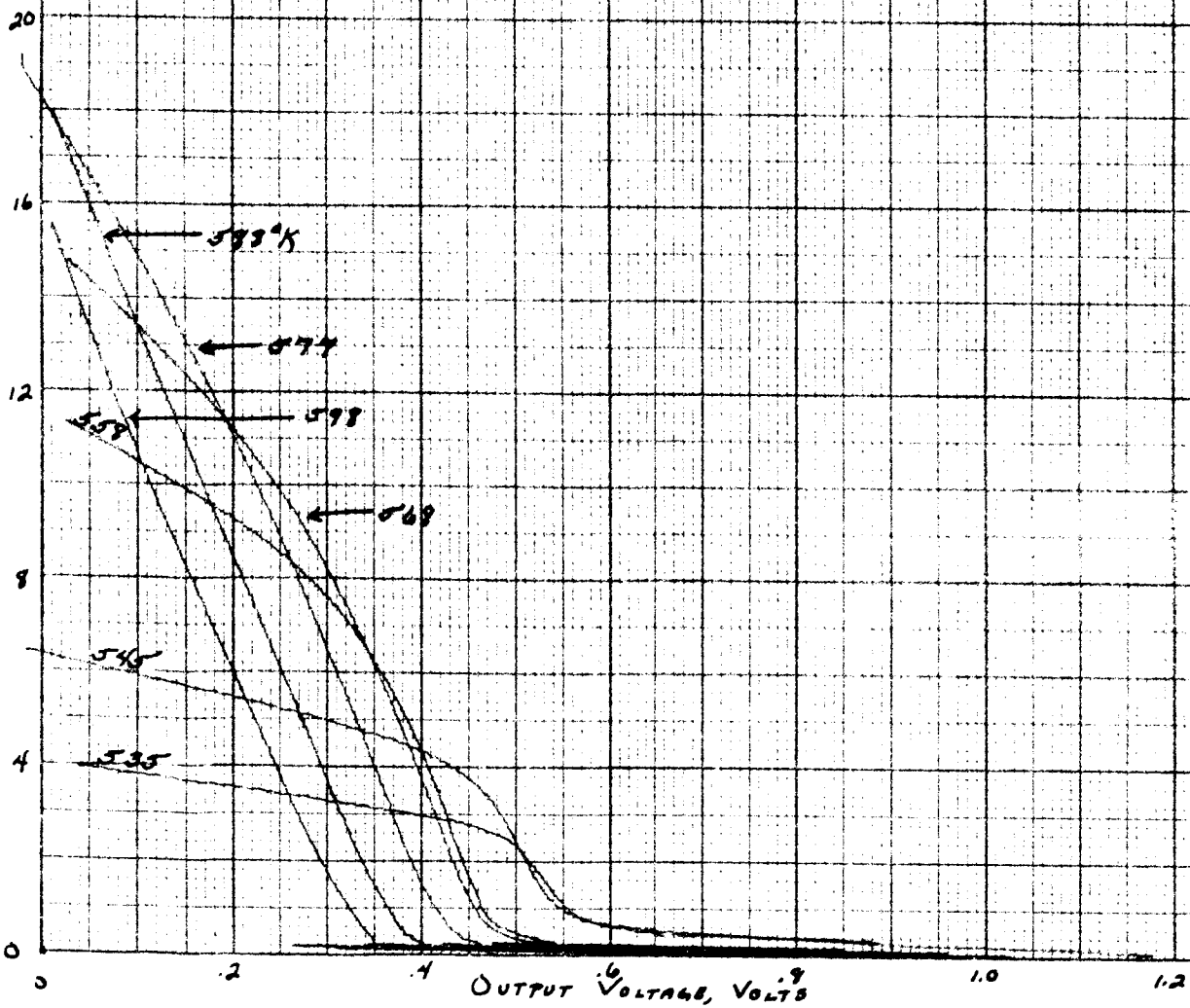


FIG. II-11. FAMILY OF I-V CURVES

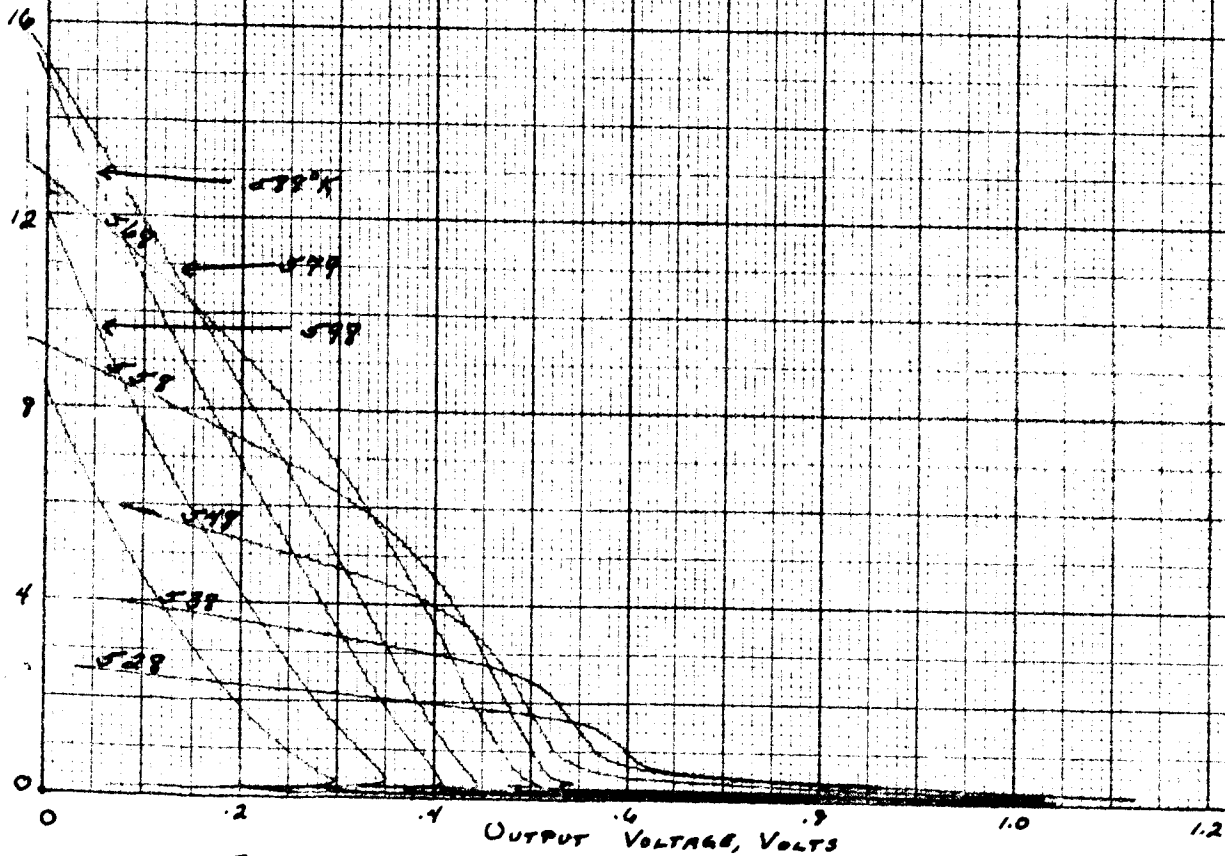
Conv. WP-1 Run 126

$T_s$  1640°K

$d$  20 mil

$T_c$  78.0°K

CURRENT DENSITY, AMPS/CM<sup>2</sup>



CONV. WP-1 REV 113

$T_E - 1740^\circ K$

$\delta$  min.

$T_0 - 868^\circ K$

CURRENT DENSITY, AMP/CM<sup>2</sup>

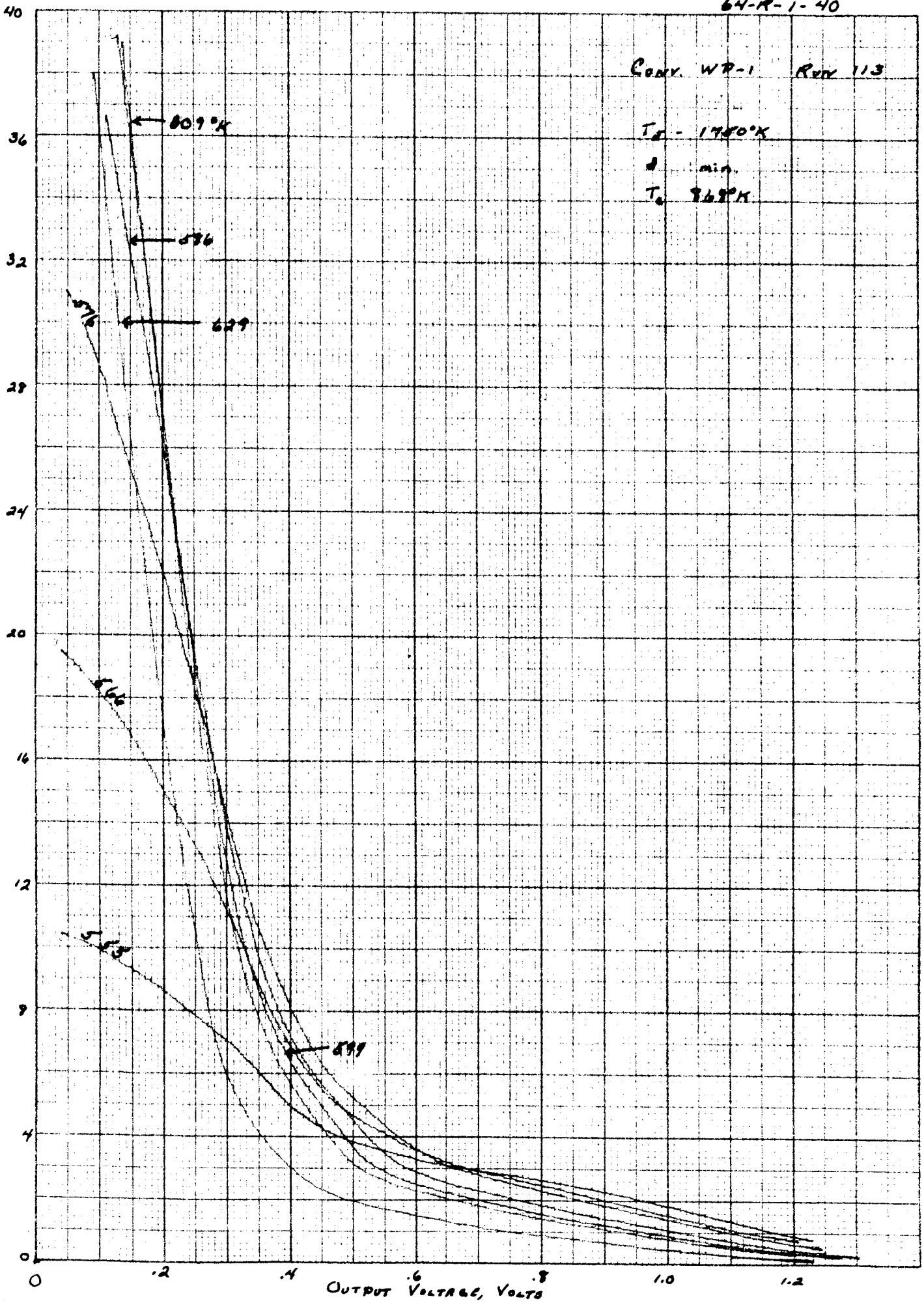


Fig. I-13. FAMILY OF I-V CURVES



RECEIVED RESEARCH

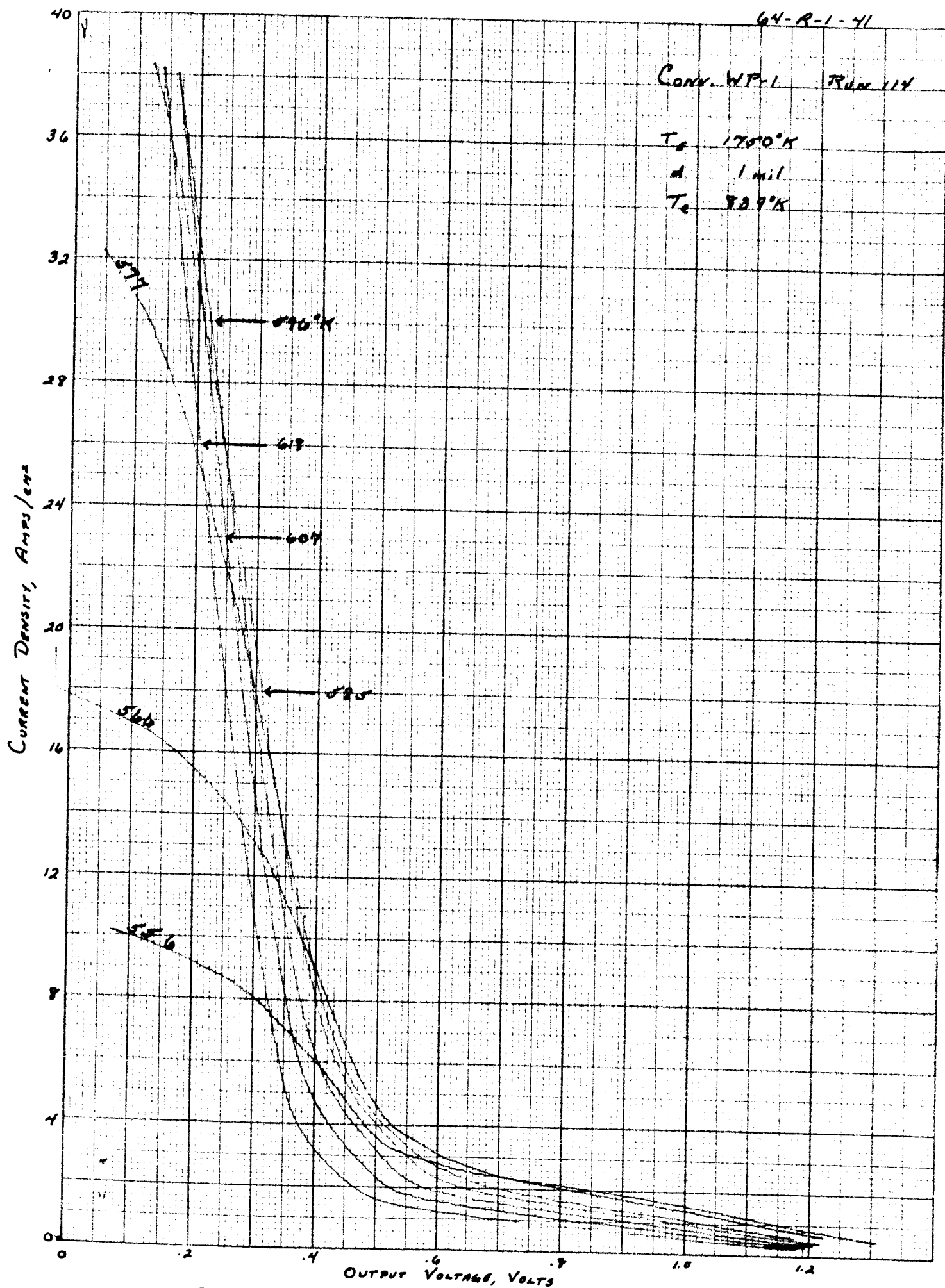


FIG. X-14 FAMILY OF I-V CURVES

64-R-1-42

Conv. WP-1 RUN 115

$T_s$  1750°K

$d$  3mil

$T_c$  847°K

CURRENT DENSITY, AMPS/CM<sup>2</sup>

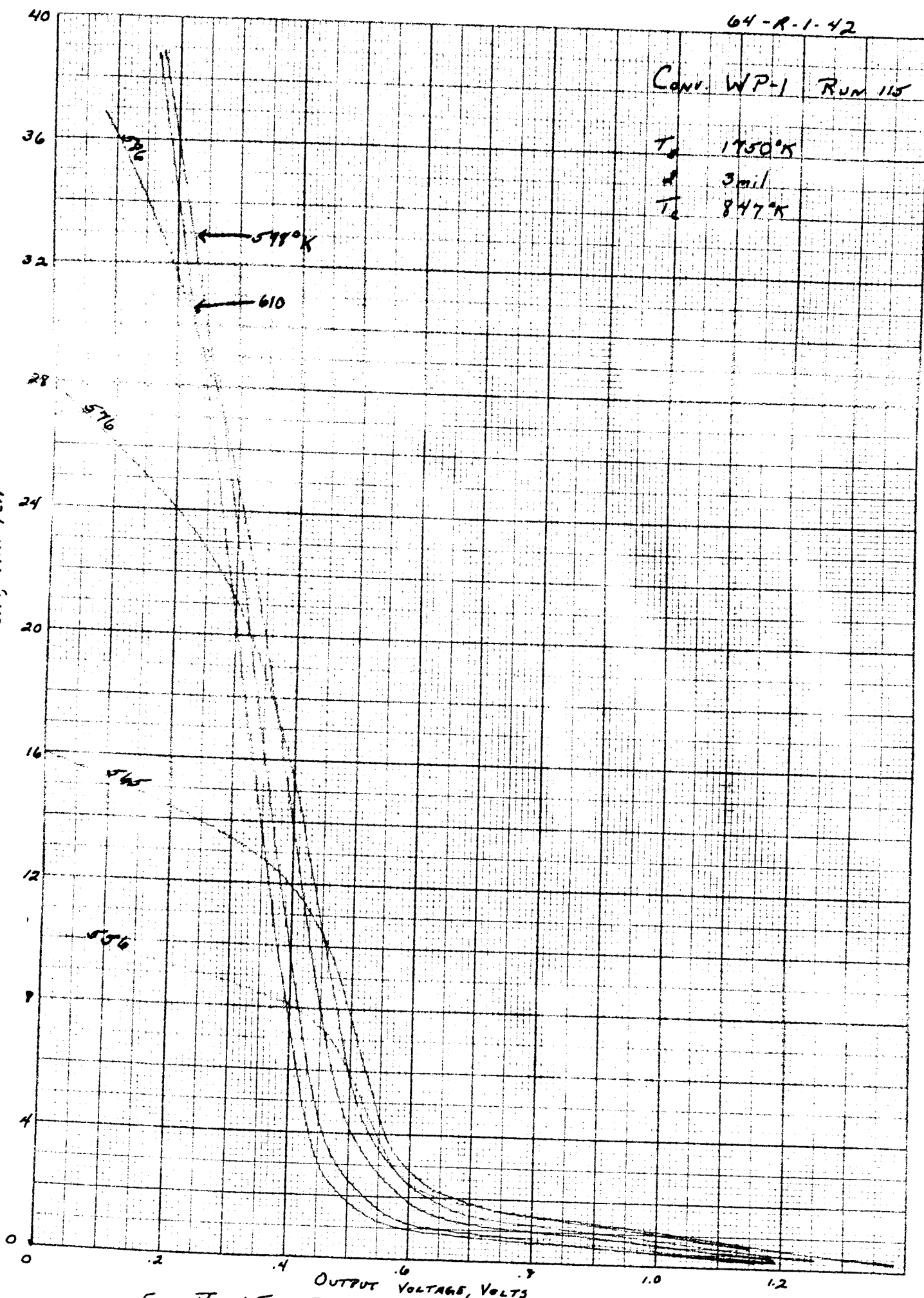


FIG. V-15 FAMILY OF I-V CURVES



64-R-1-43

Conv. WP-1 Run 116

$T_c$  1750°K

$d$  6 mil

$T_c$  840°K

CURRENT DENSITY, AMPS/CM<sup>2</sup>

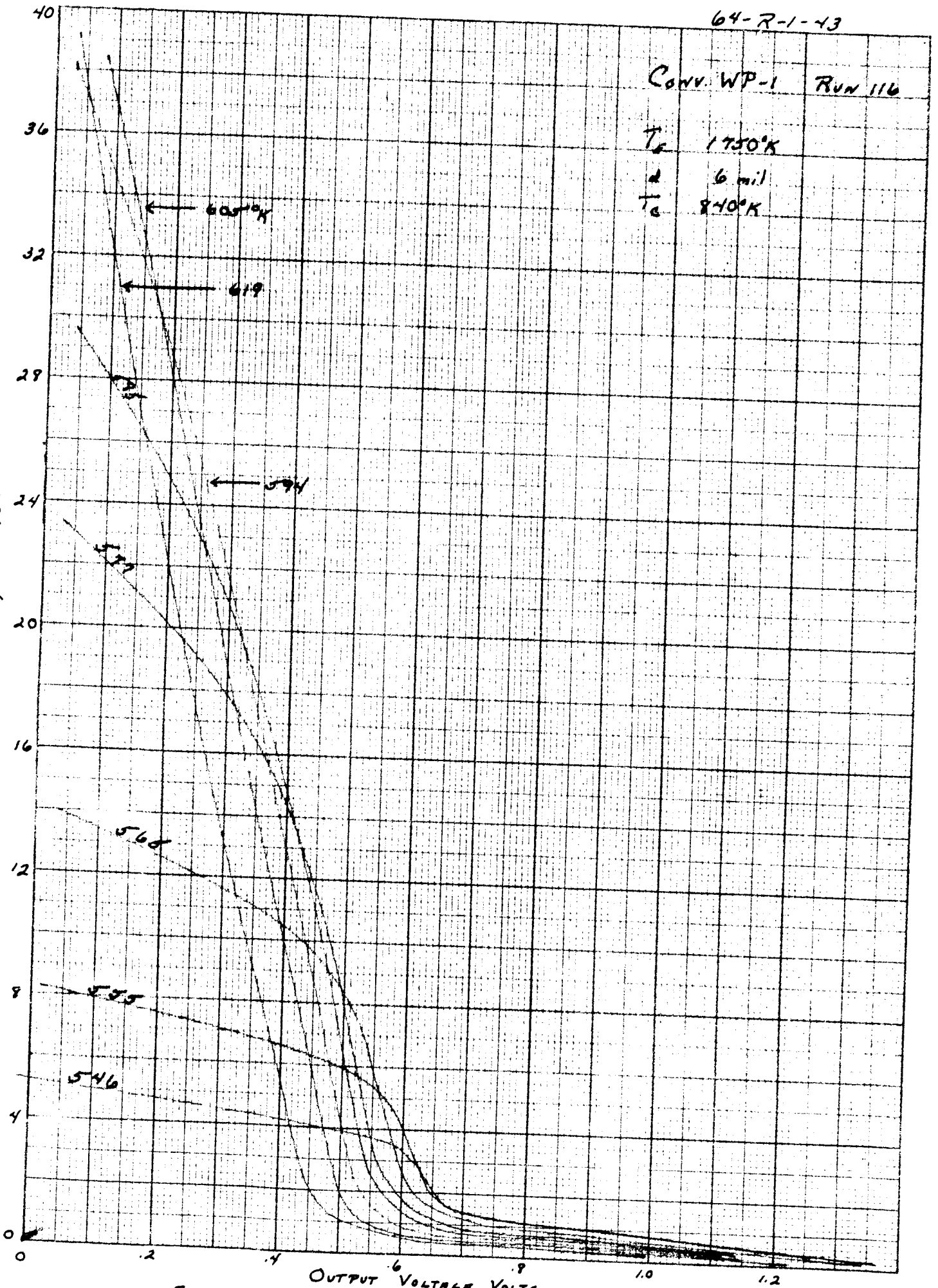


Fig. V-16 FAMILY OF I-V CURVES

64-R-1-44

CANY WP-1 RUN 117

$T_s$  1750°K

$d$  10 mil

$T_a$  975°K

CURRENT DENSITY, AMPS/CM<sup>2</sup>

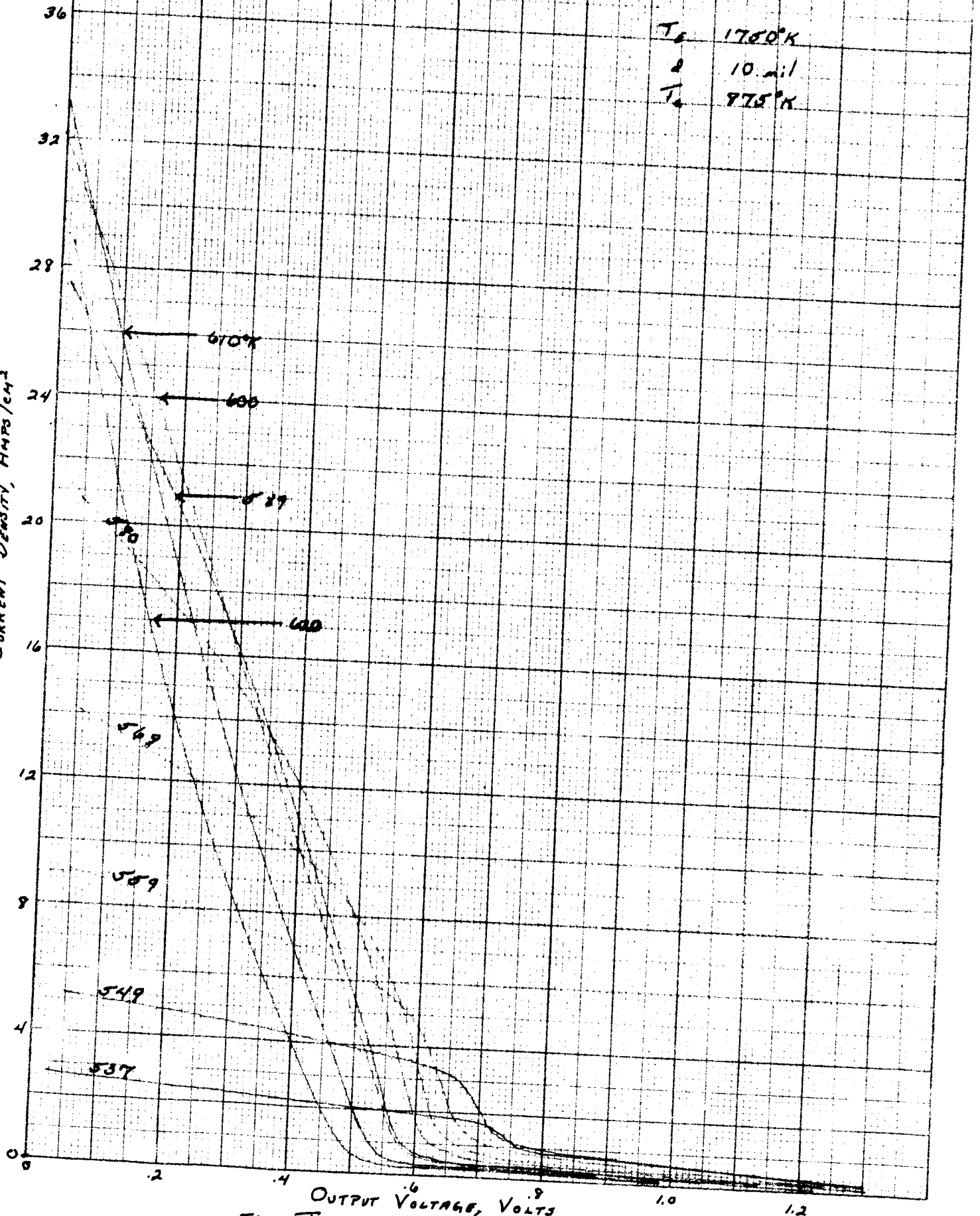


FIG. V-17 FAMILY OF T-V

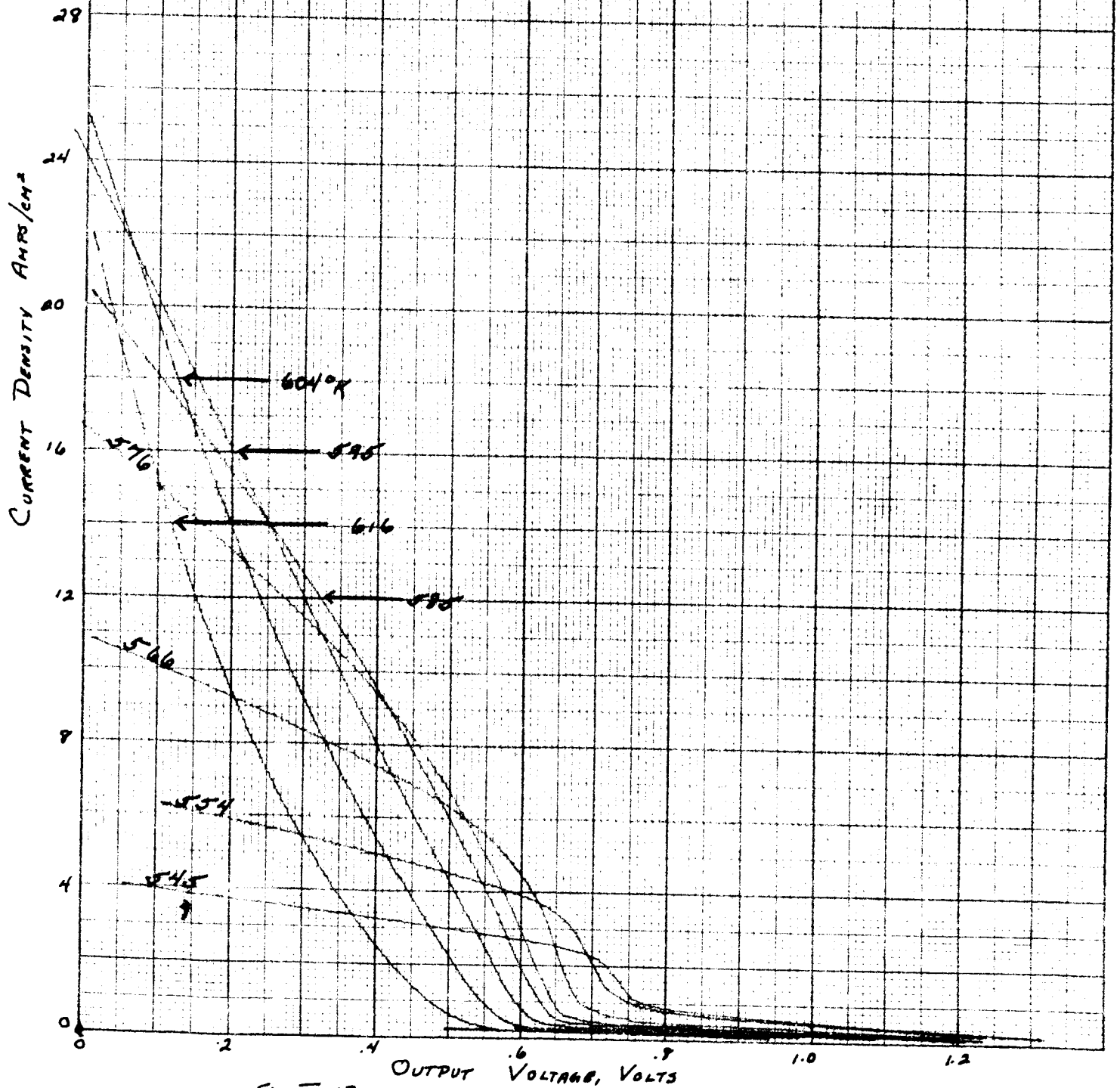
64-R-1-45

Conv. WP-1 RUN 118

$T_e$  1750°K

$d$  15 mil

$T_c$  841°K



64-R-1-46

CONV. WP-1 RUN 119

$T_s$  1750°K

$d$  20 mil

$T_c$  818°K

CURRENT DENSITY, AMPS/CM<sup>2</sup>

20

16

12

8

4

0

6110°K

595

571

545

567

540

OUTPUT VOLTAGE, VOLTS

FIG. I-19 FAMILY OF I-V CURVES

64-R-1-47

Conv. WP-1

RUN 102

$T_c$  1850°K

$d$  min

$T_c$  891°K

CURRENT DENSITY, AMPS/CM<sup>2</sup>

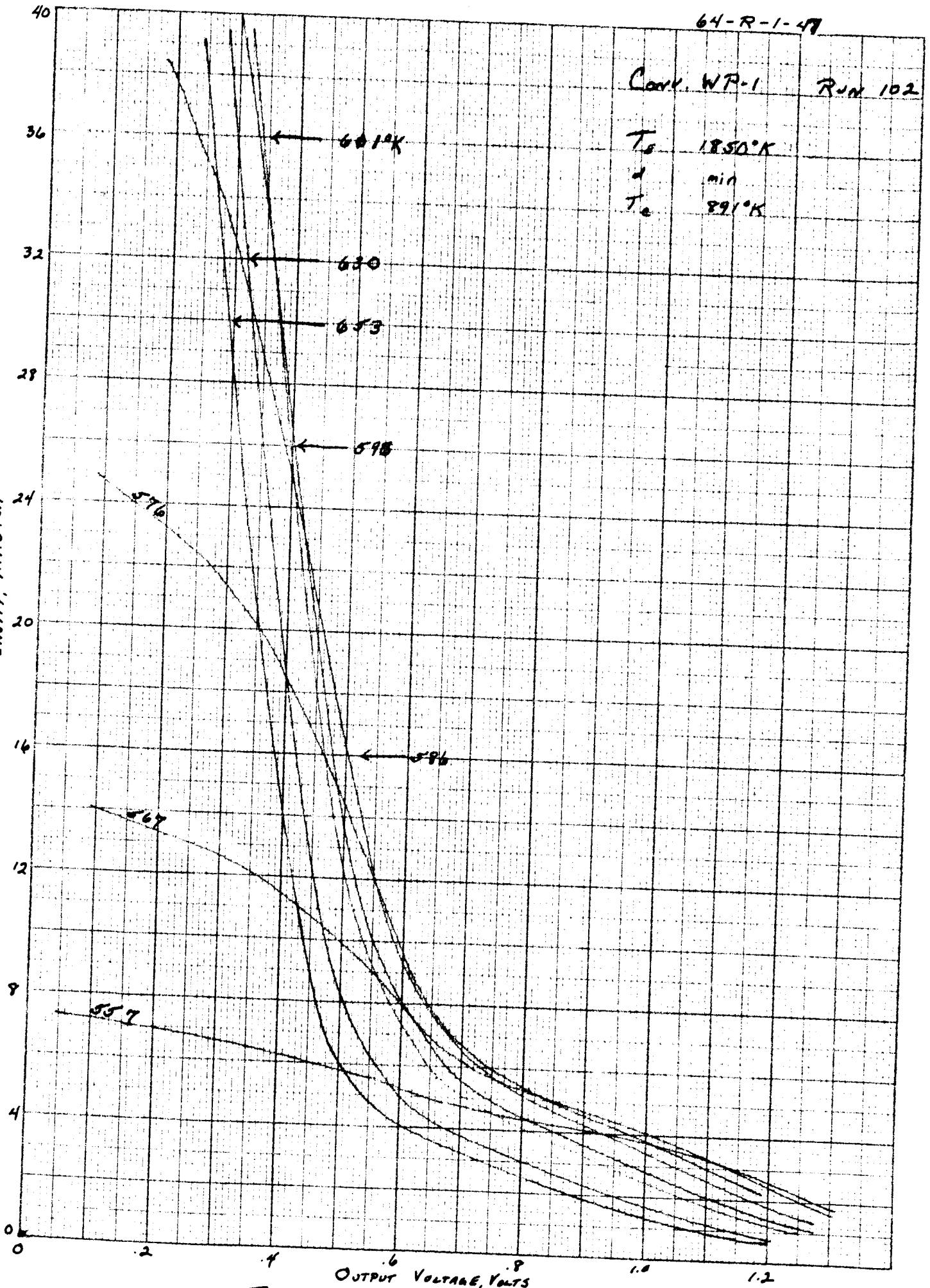


Fig. V-20. FAMILY OF I-V CURVES

64-R-1-48

Conv. WP-1

Run 103

$T_0$  1850°K

$d$  1 mil

$T_c$  269°K

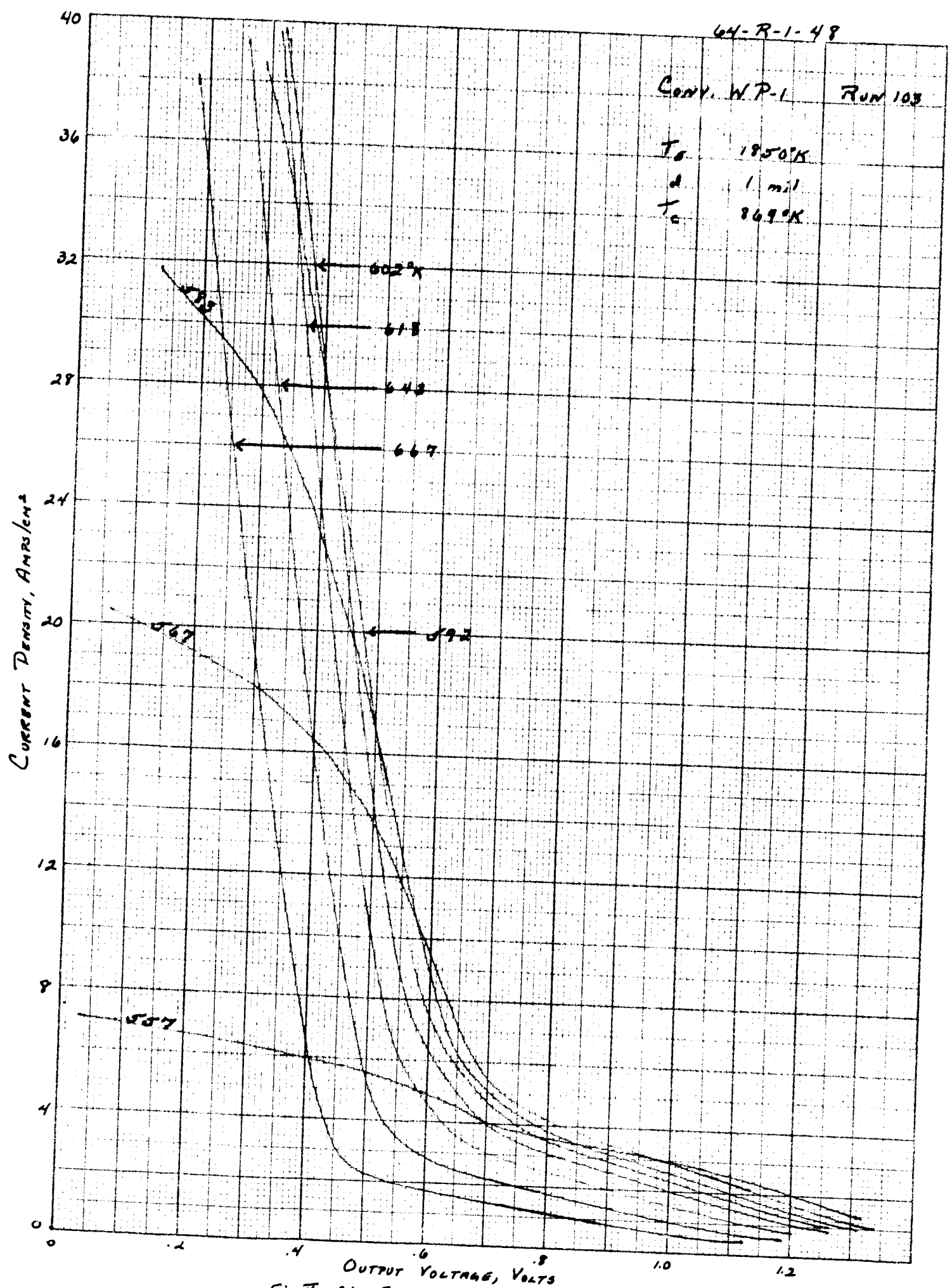


FIG. I-21 FAMILY OF I-V CURVES

64-R-1-49

CANY. WP-1 Run 104

$T_a$  1850°K

$d$  3 mil

$T_c$  864°K

Current Density, Amperes/cm<sup>2</sup>

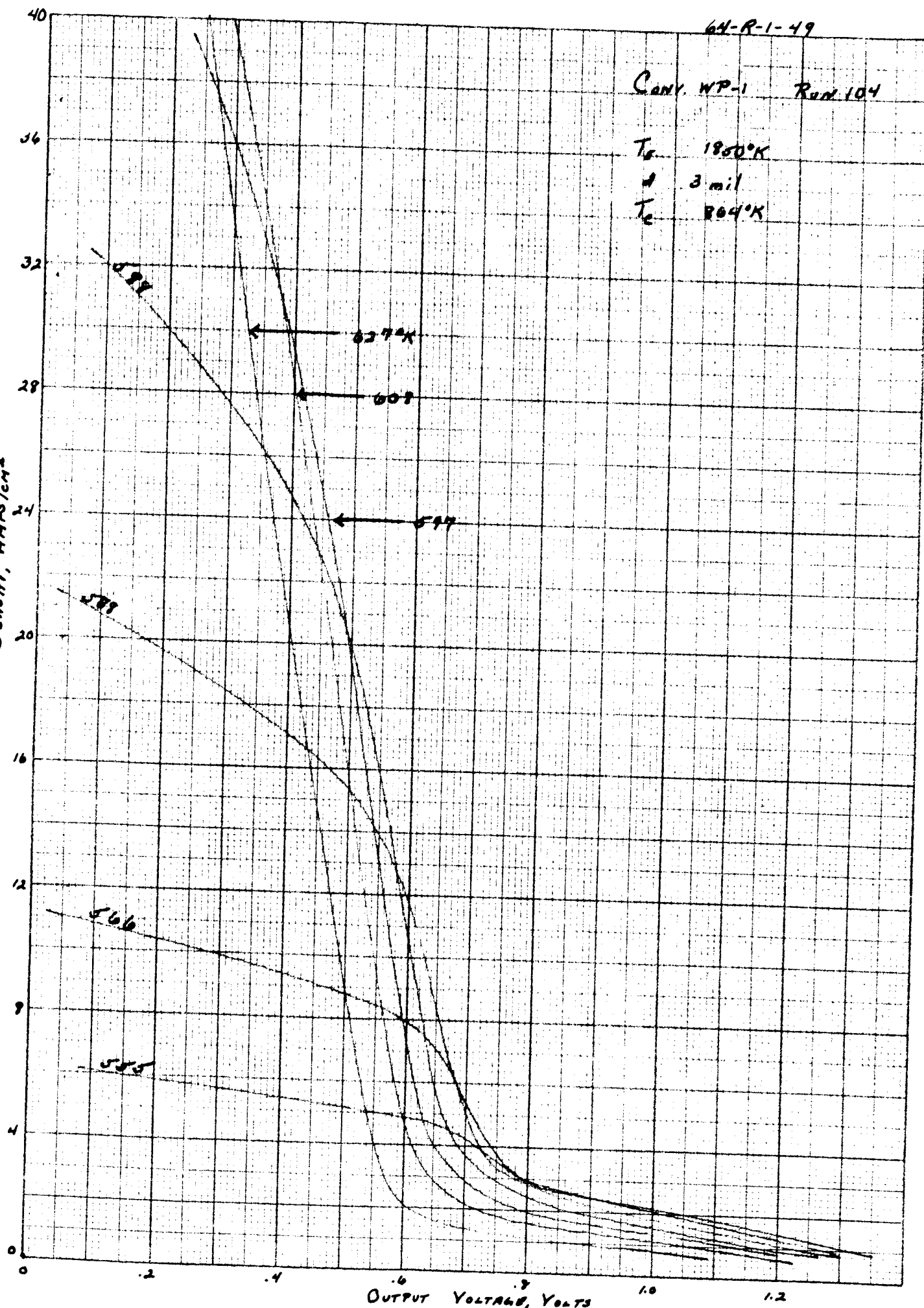


FIG. X-22 FAMILY OF I-V CURVES



64-R-1-50

Conv. WP-1 Run 105

$T_s$  1850°K  
 $d$  6 mils  
 $T_c$  982°K

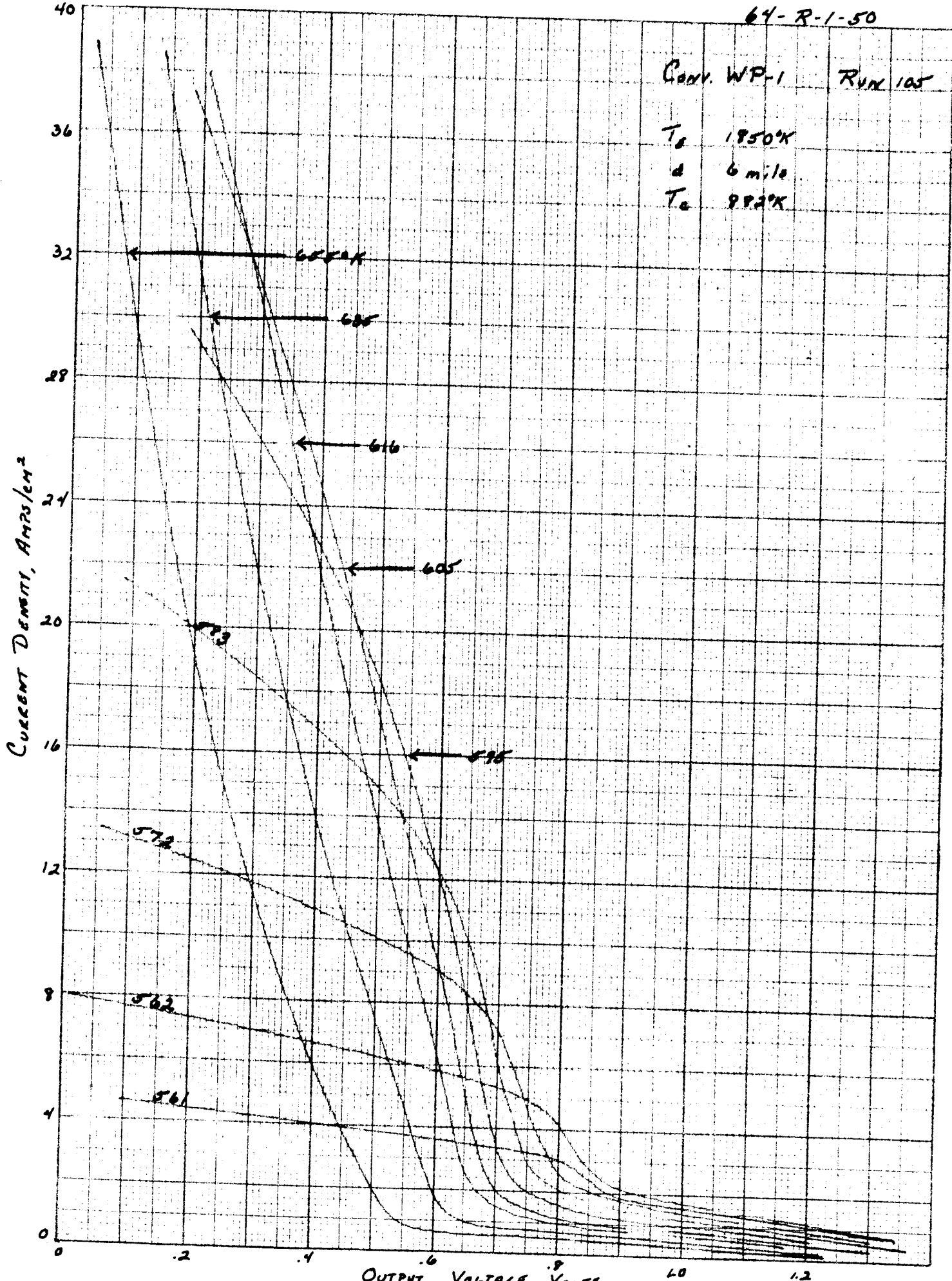
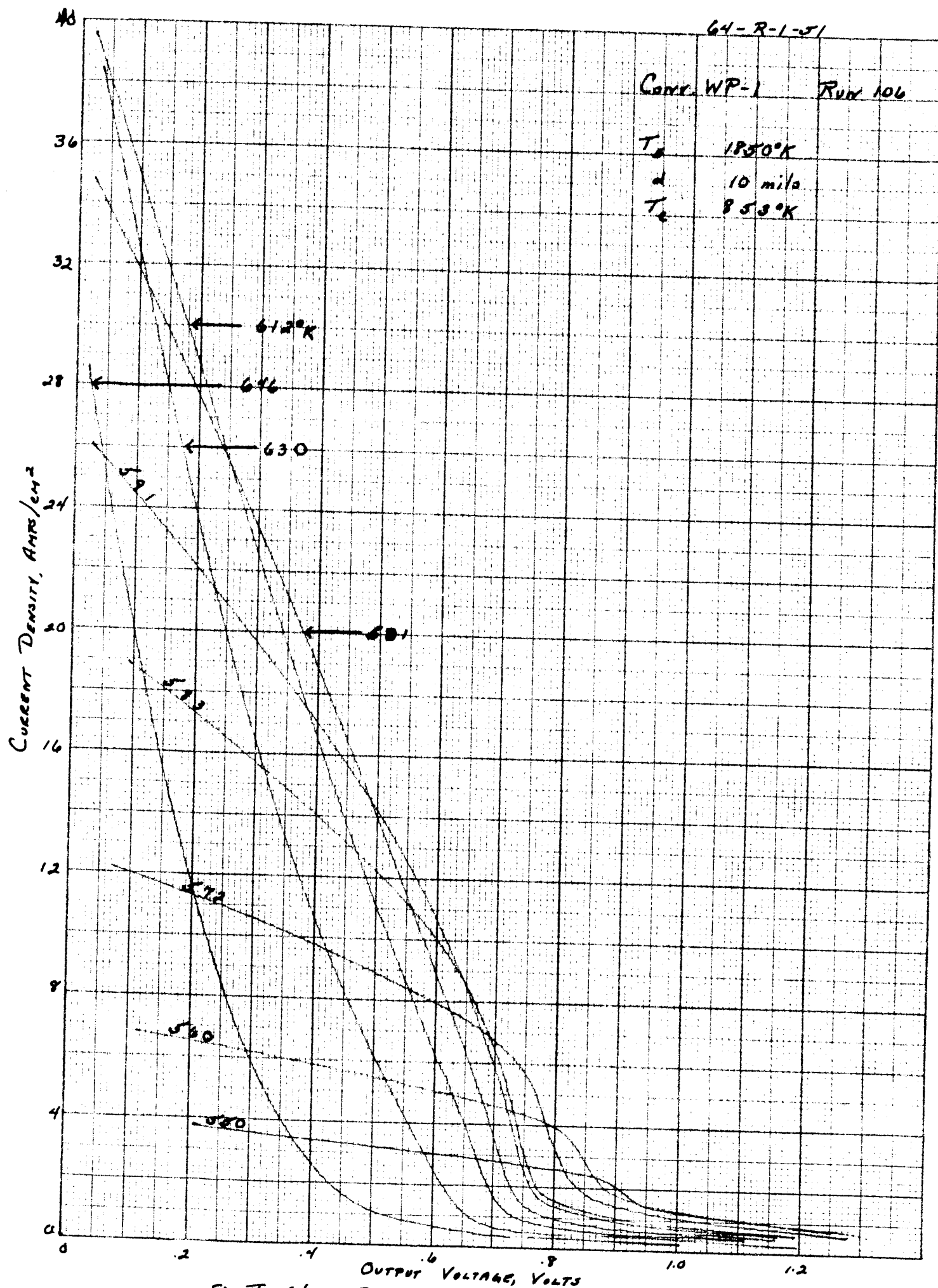


Fig. X-23 FAMILY OF I-V CURVES





64-R-1-52

CONT. WP-1

RUN 107

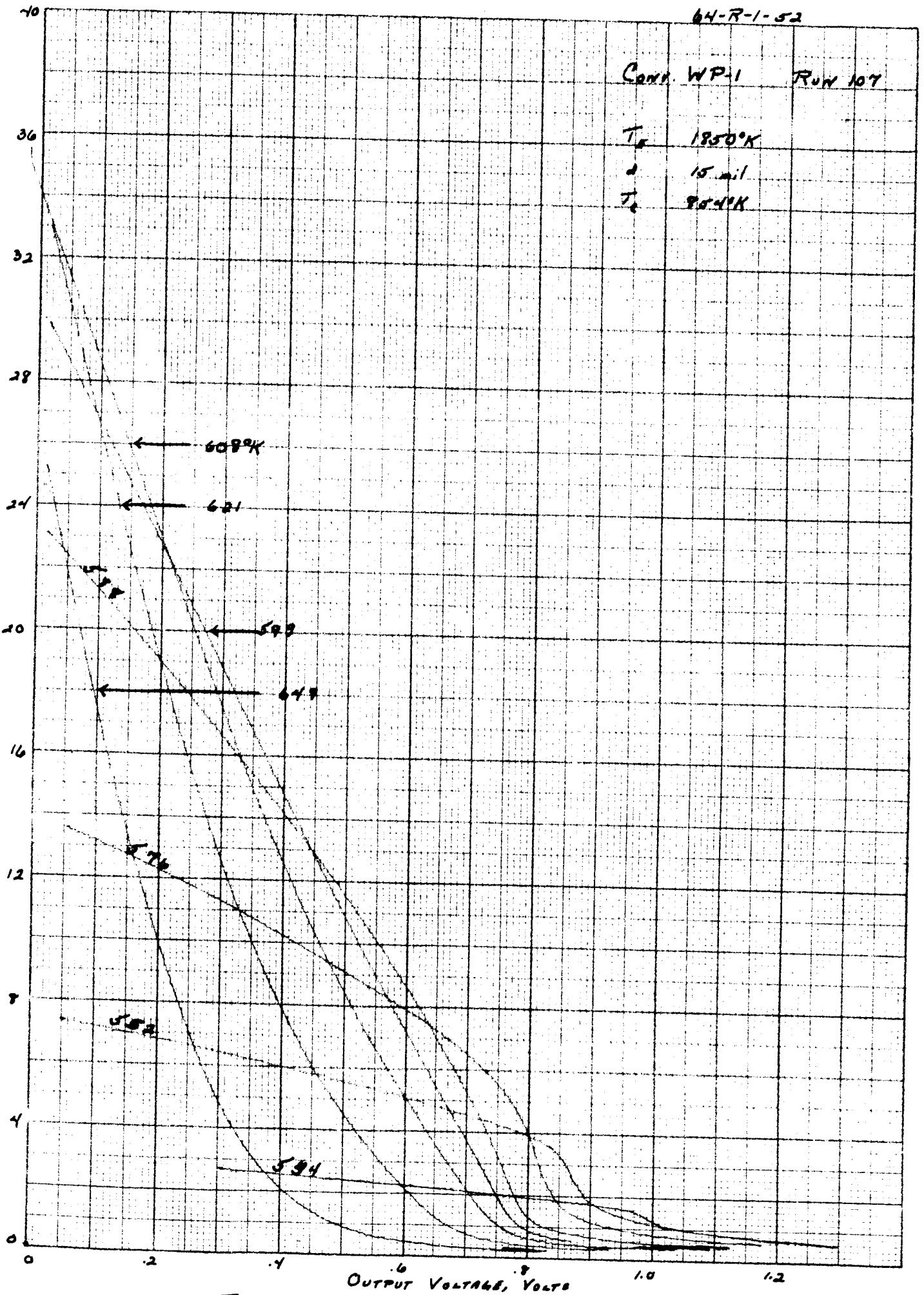
 $T_s$  1850°K $d$  15 mil $T_c$  954°KCURRENT DENSITY, AMPS/CM<sup>2</sup>

FIG. I-25 FAMILY OF I-V CURVES

64-R-1-53

Conv. WP-1

Run 108

$T_c$  1850°K

$d$  20 mil

$T_e$  866°K

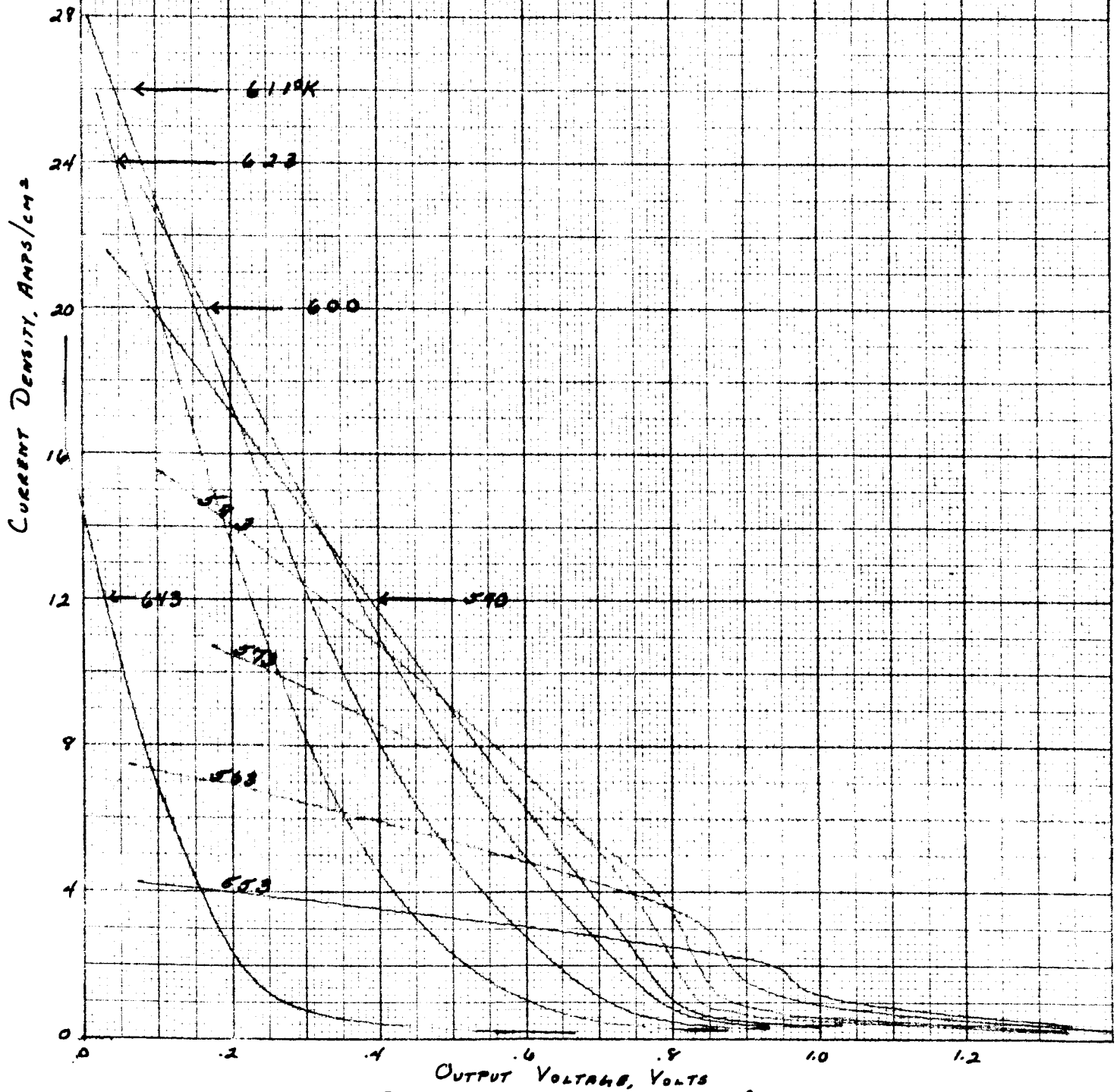


FIG. 26 FAMILY OF I-V CURVES

64-R-1-54

Conv. WP-1

Run 109

$T_e$  1950°K

$d$  min.

$T_a$  902°K

CURRENT DENSITY, AMPS/CM<sup>2</sup>

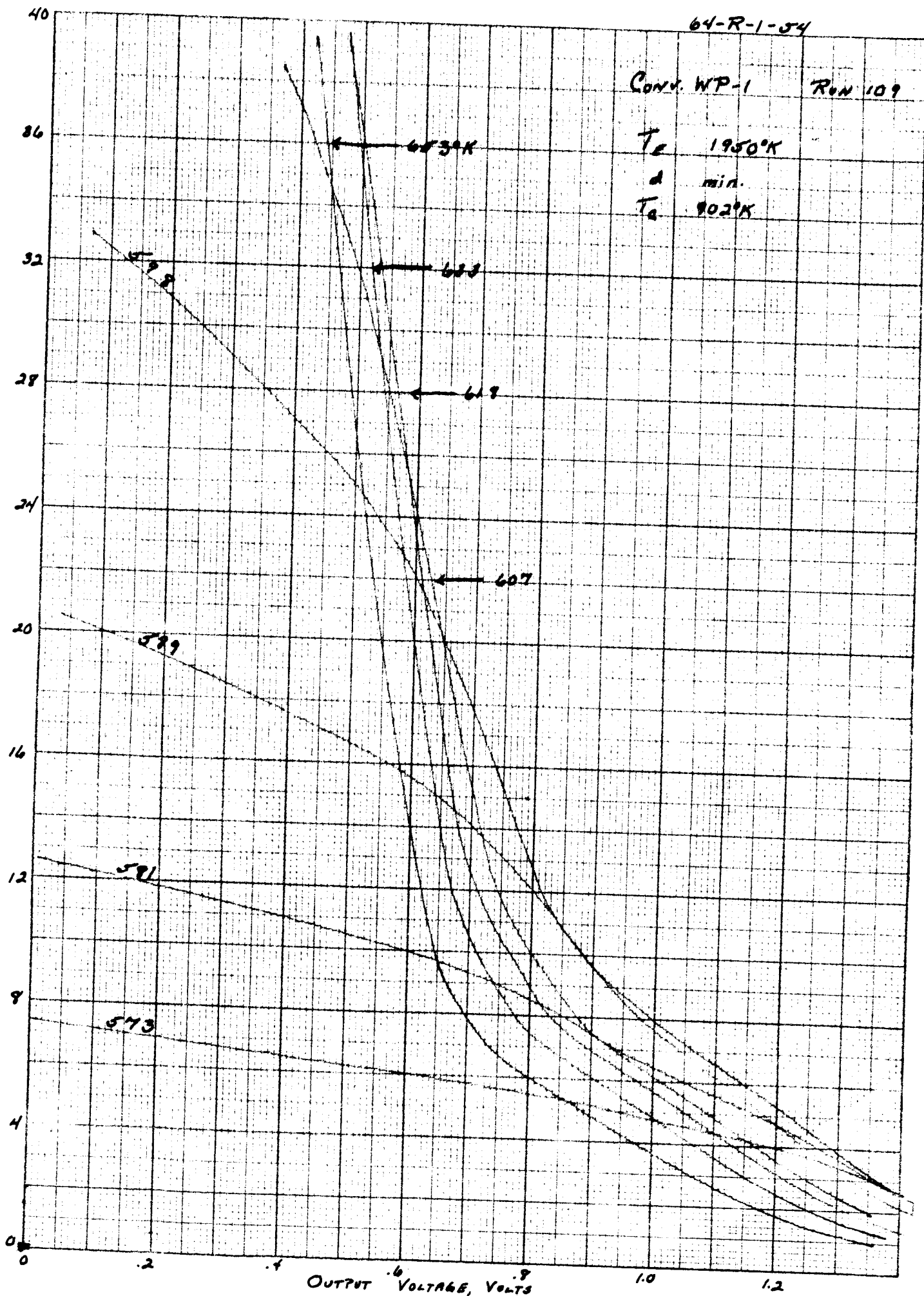


FIG. V-27 FAMILY OF I-V CURVES

64-R-1-32

Conv. WP-1 Run 110  
 $T_s$  1950°K  
 $d$  1 mil  
 $T_c$  886°K

CURRENT DENSITY, AMP/CM<sup>2</sup>

36

32

28

24

20

16

12

8

4

0

645

← 631°K

603

618

600

590

579

OUTPUT VOLTAGE, VOLTS

1.0

1.2

1.4

FIG. 7-28. FAMILY OF I-V CURVES

64-R-1-55

Conv. WP-1 Run III

$T_e = 1950^\circ K$

$\mu = 3 \text{ m.s.l}$

$T_c = 880^\circ K$

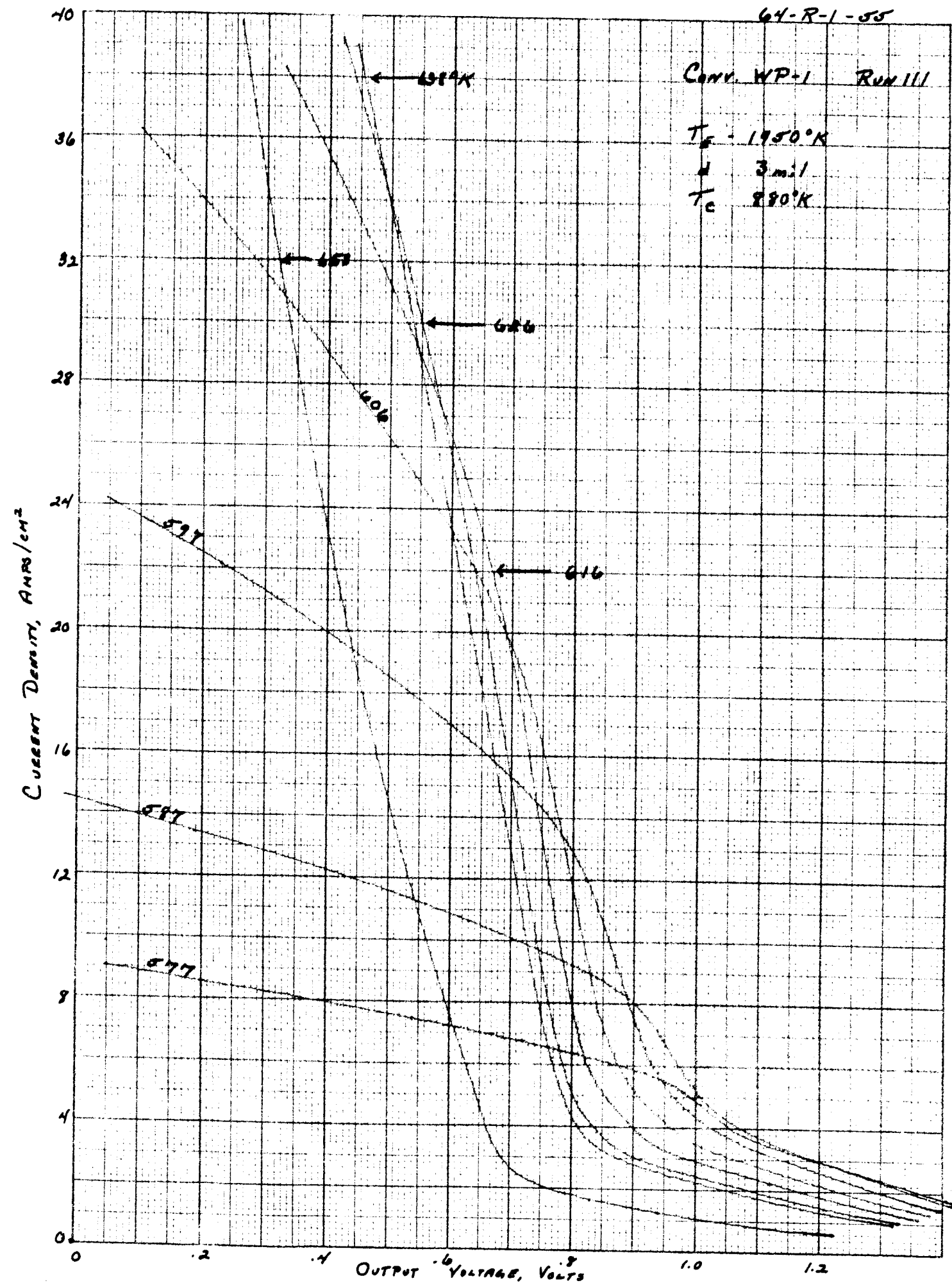


FIG II-29 FAMILY OF I-V CURVES

35-1073  
RECEIVED  
NOV 1954

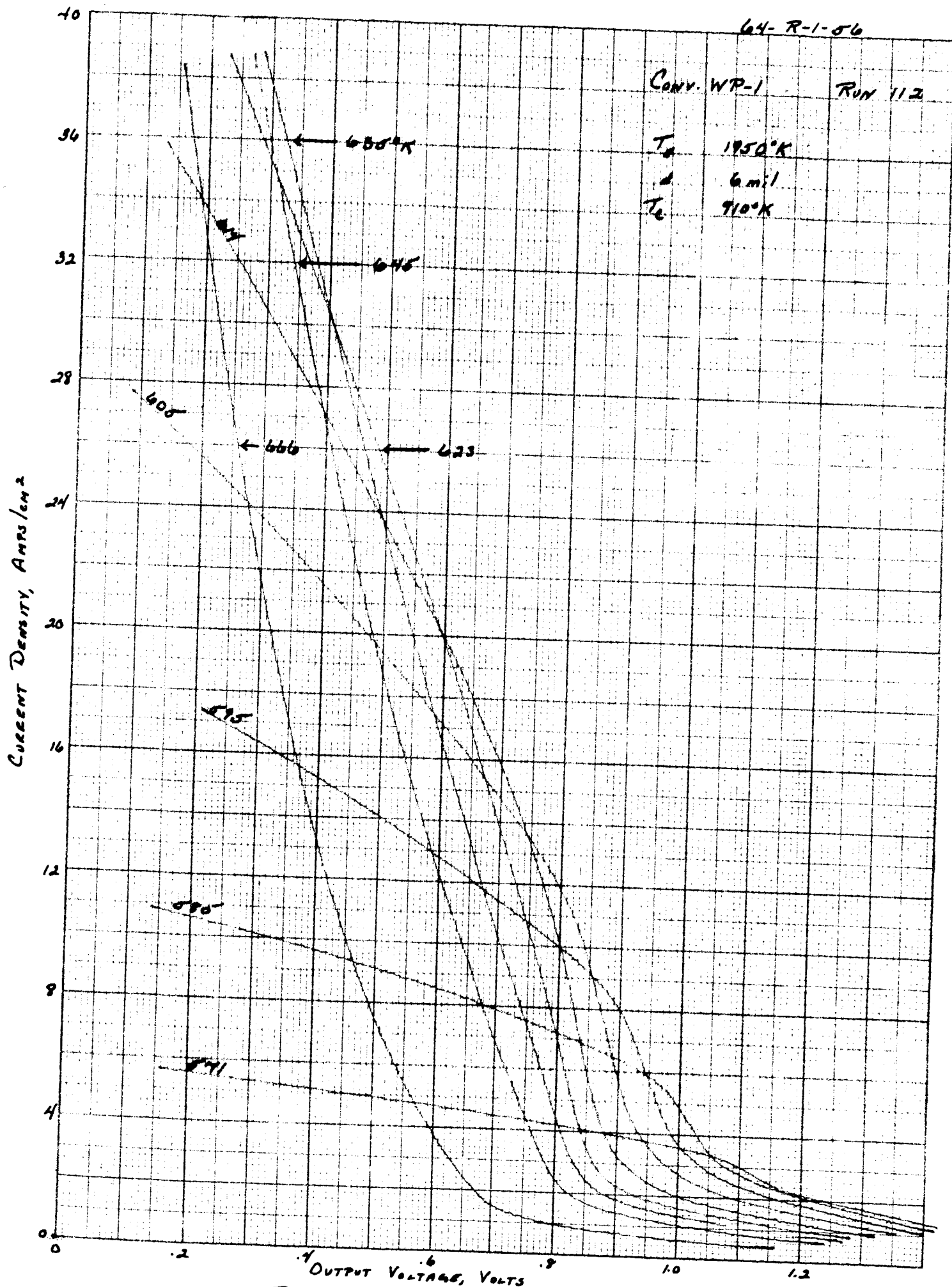


Fig. X-30. FAMILY OF I-V CURVES



64-R-1-57

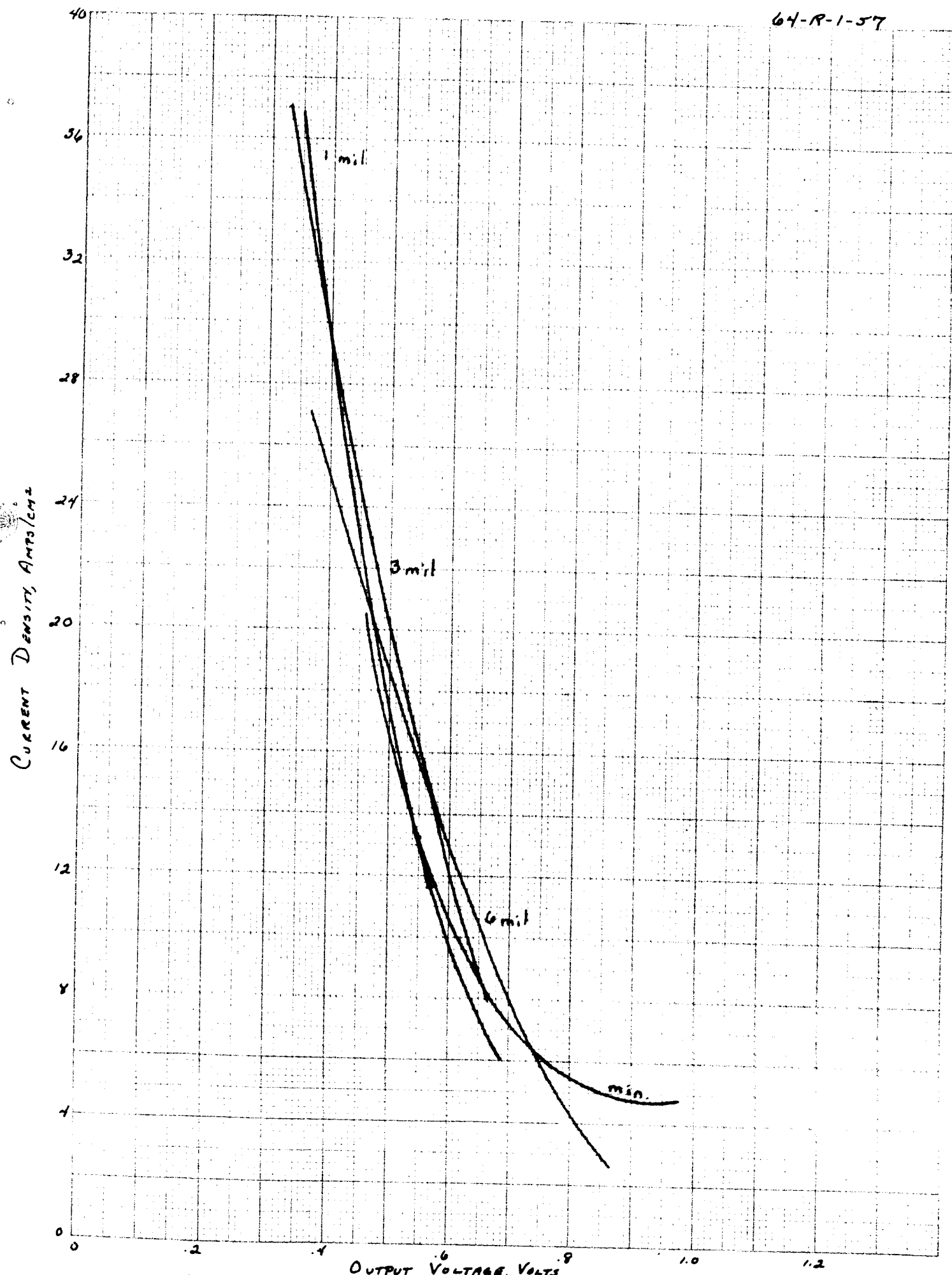
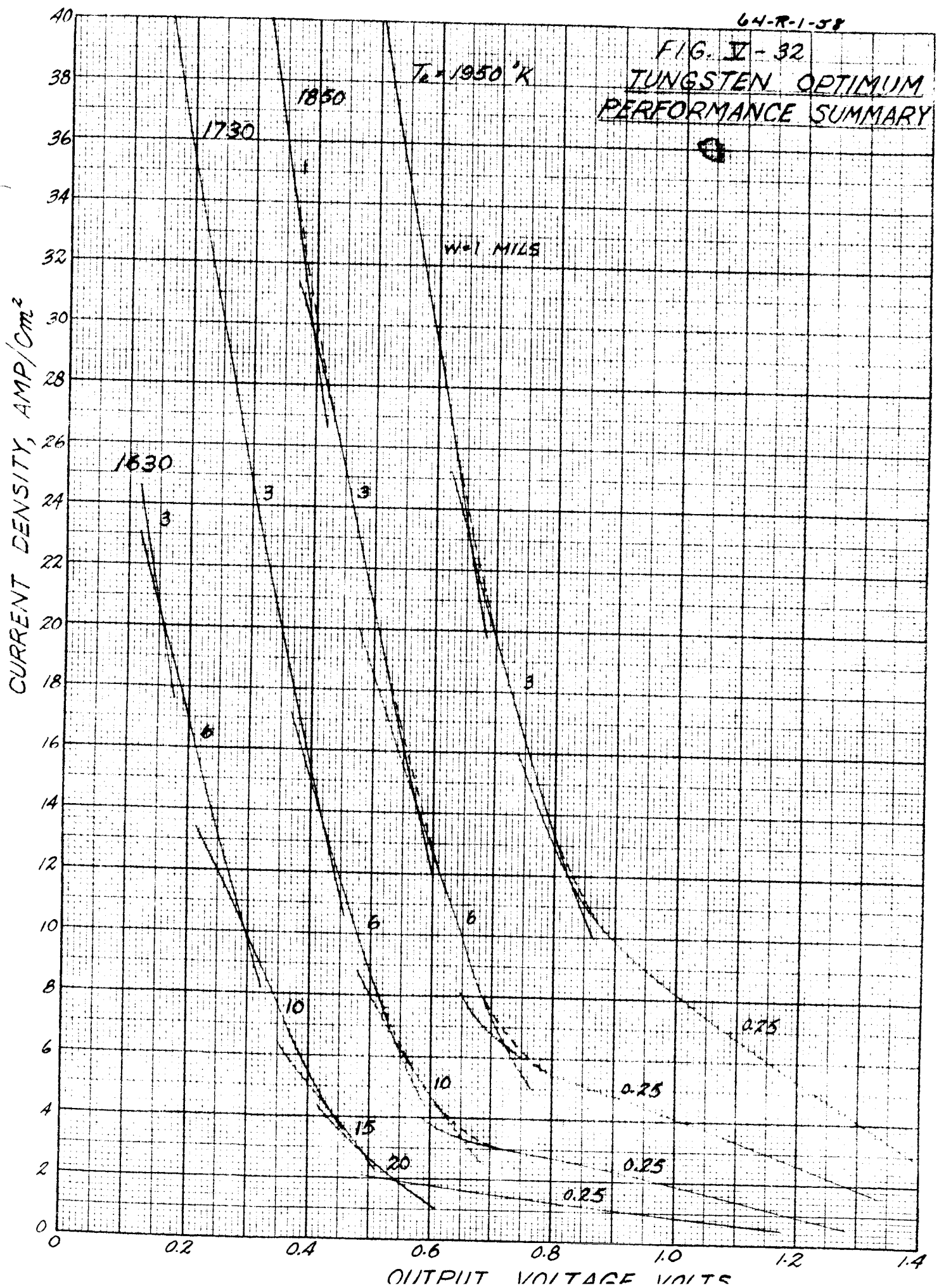


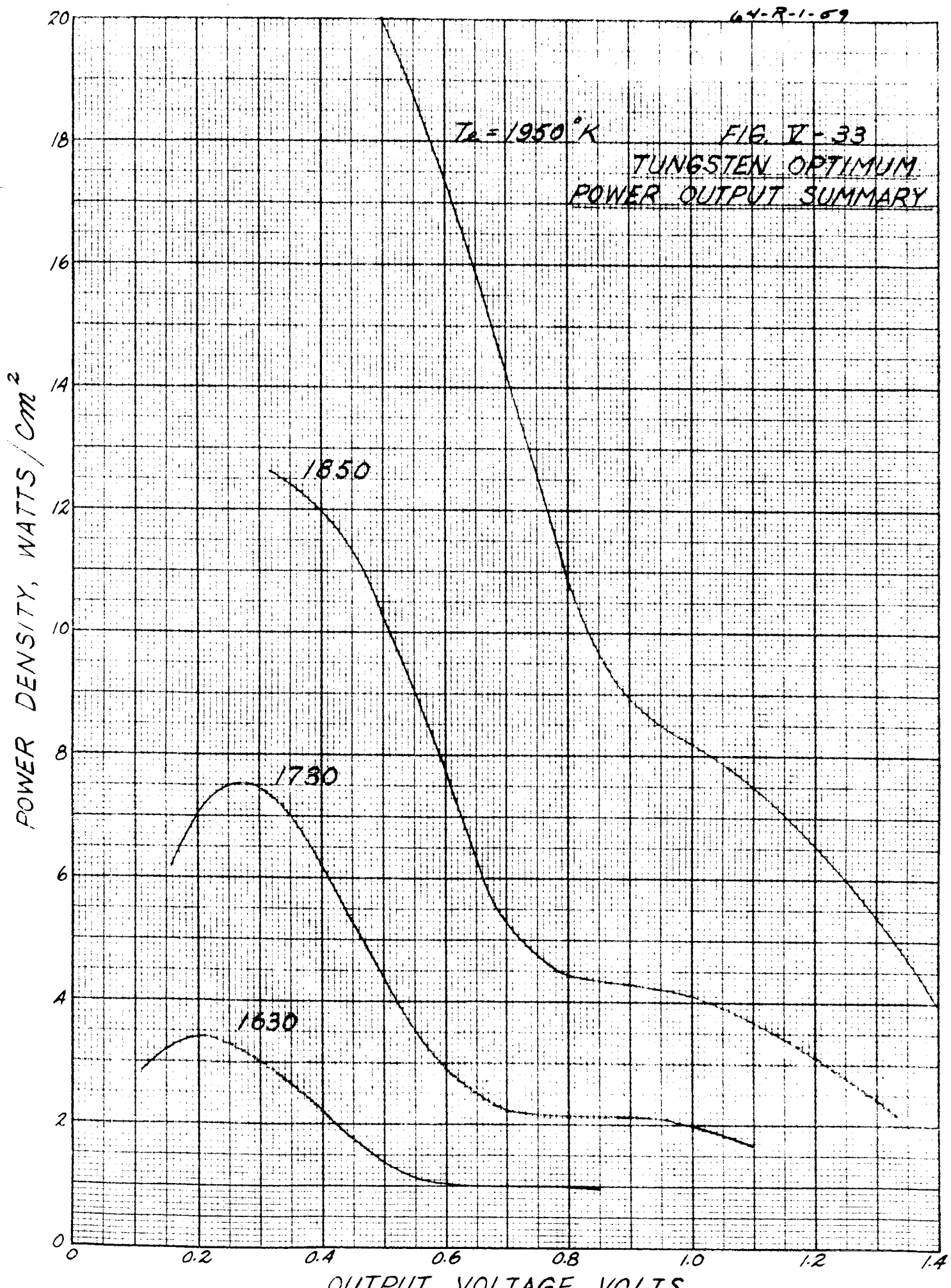
FIG. 5-21 ENVELOPE OF T. H. C. CURVES



64-R-1-58

FIG. V-32  
TUNGSTEN OPTIMUM  
PERFORMANCE SUMMARY





$T_e = 1950^{\circ}K$

FIG. IV-33

TUNGSTEN OPTIMUM  
POWER OUTPUT SUMMARY

1850

1730

1630

POWER DENSITY, WATTS/CM<sup>2</sup>

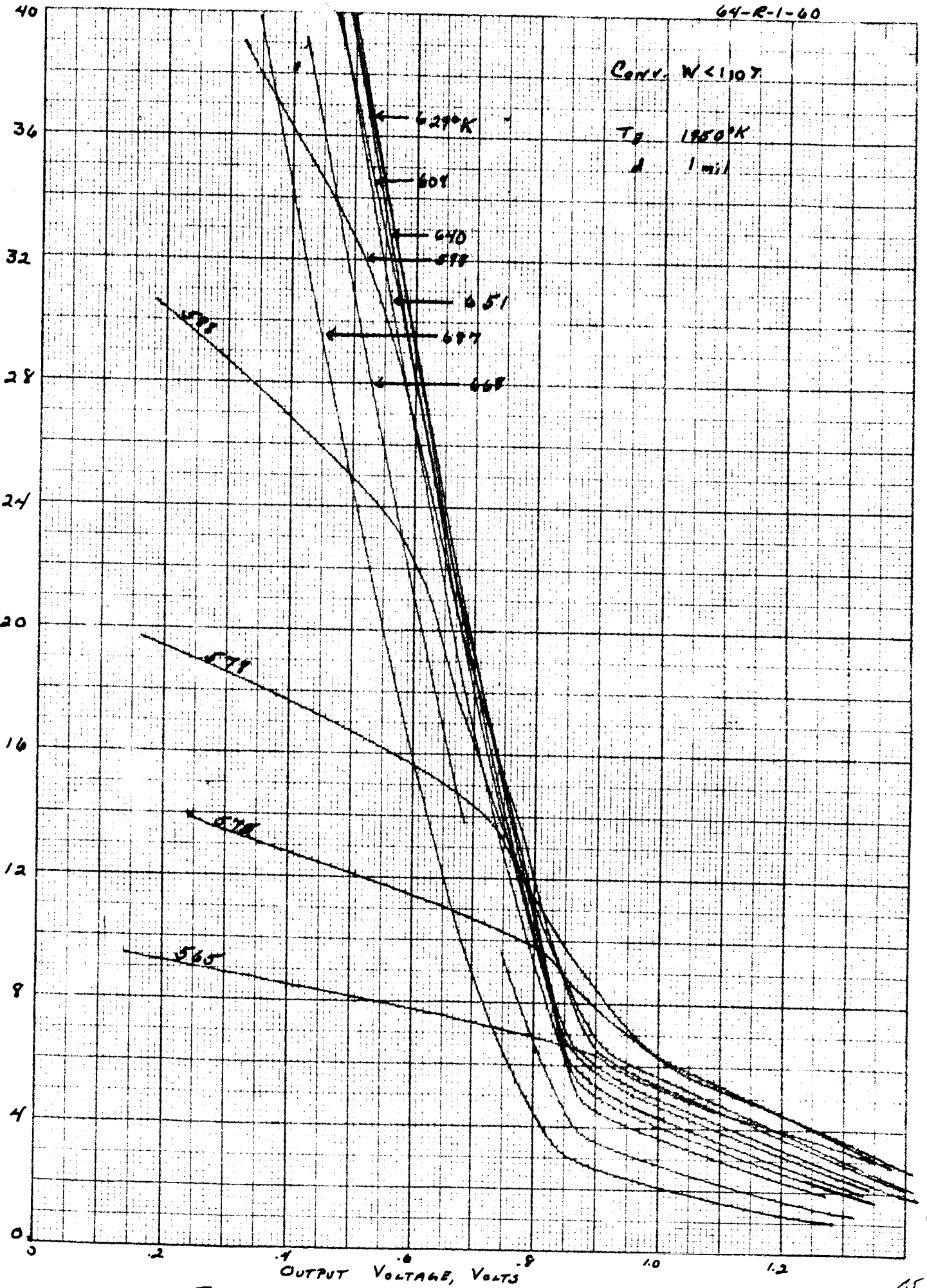
OUTPUT VOLTAGE VOLTS

Conv. W < 1107

$T_p$  1950°K

$d$  1 mil

Current Density, Amperes/cm<sup>2</sup>

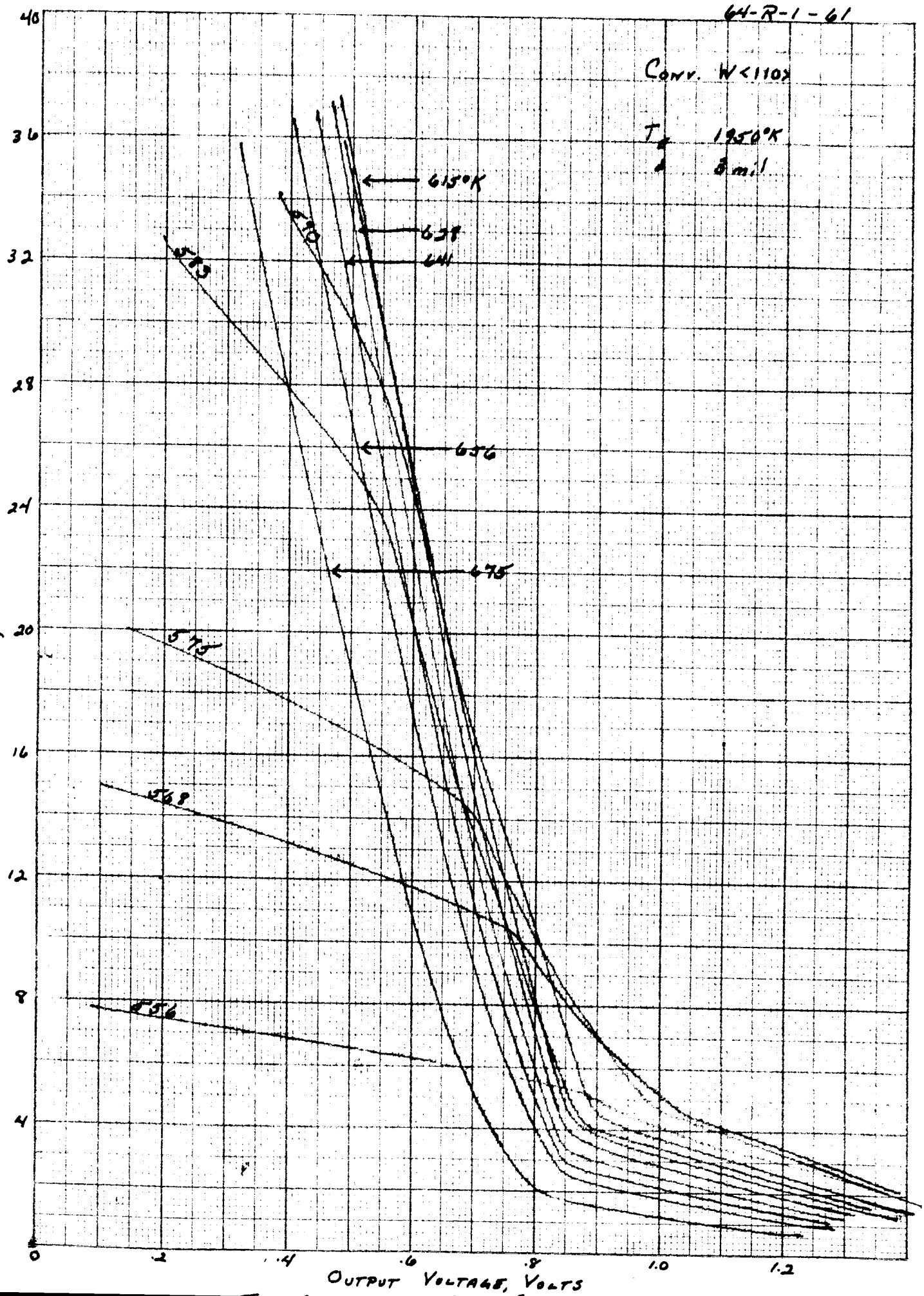


64-R-1-61

Conv. W < 110%

$T_c$  1950°K  
 $\delta$  8 mil

CURRENT DENSITY, AMPS/CM<sup>2</sup>



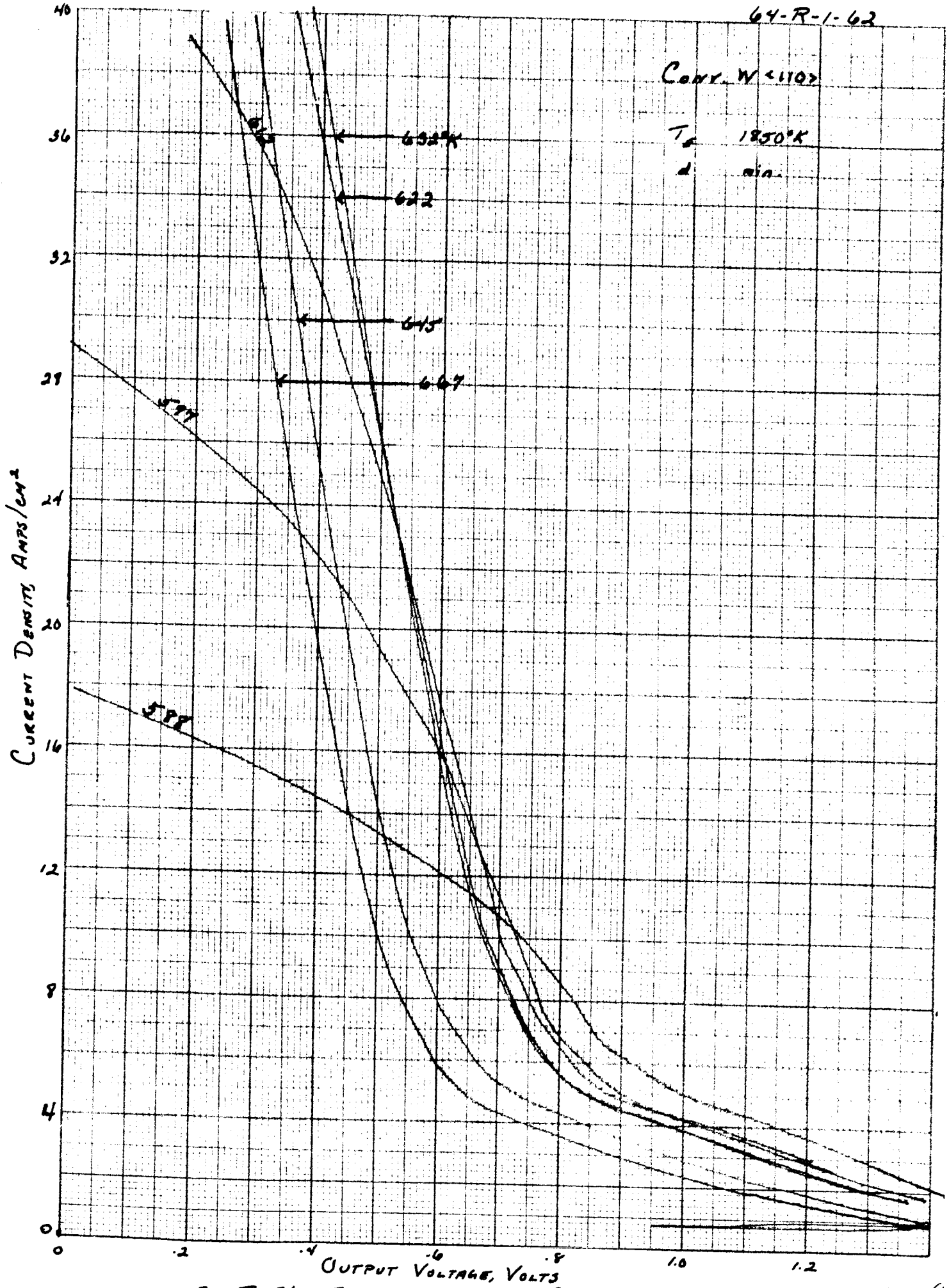
OUTPUT VOLTAGE, VOLTS

64-R-1-62

Conn. W <110>

$T_s$  1850°K

$d$  min.

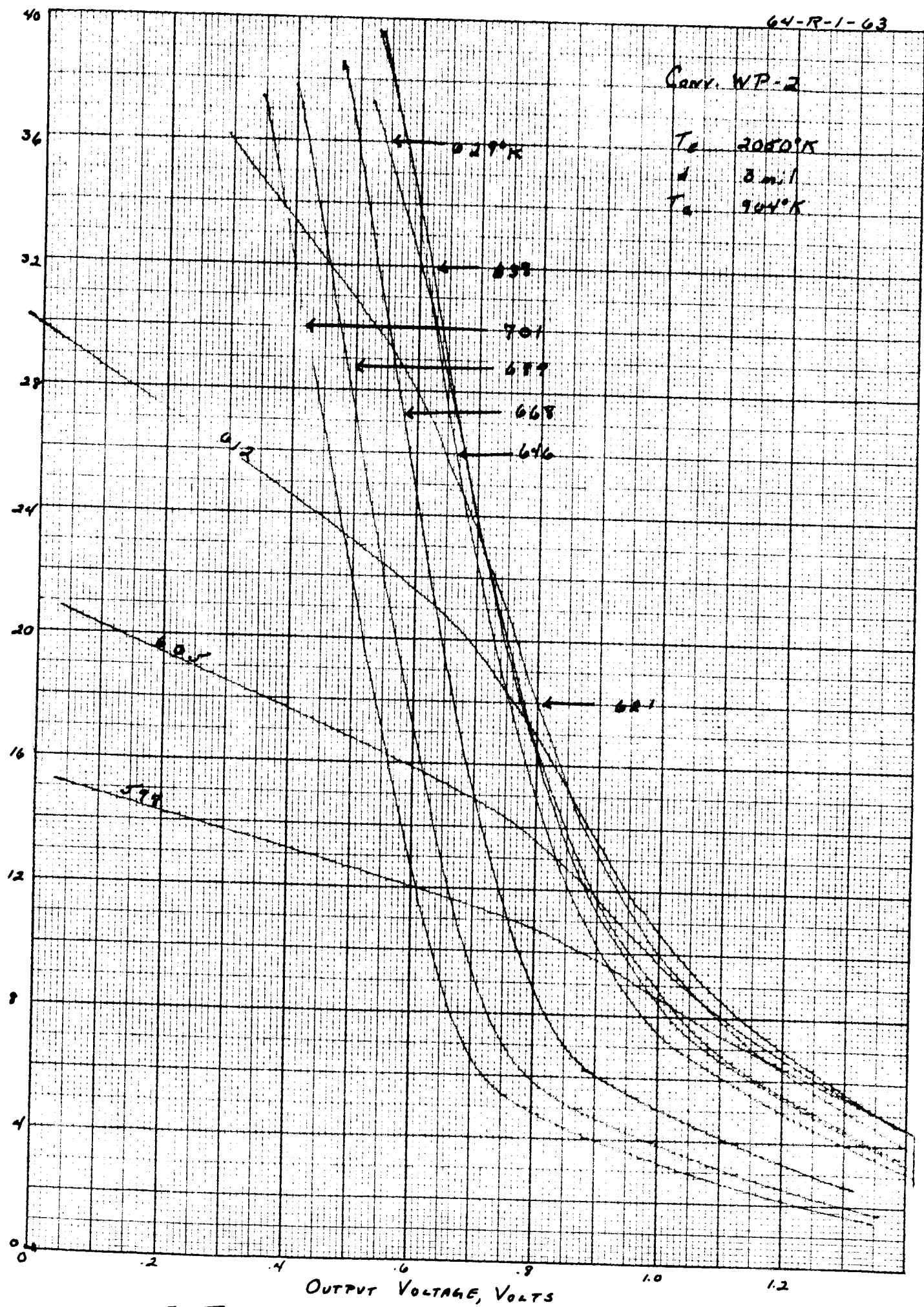


IN THE KEUFFEL & ESSER CO. PRINTING PLANT

Conv. WP-2

$T_c$  2080°K  
 $d$  8 mil  
 $T_a$  904°K

CURRENT DENSITY, AMPS/CM<sup>2</sup>



OUTPUT VOLTAGE, VOLTS



64-R-1-64

Conn. WP-2

$T_s$  1950°K  
 $d$  3 mil  
 $T_a$  716°K

Current Density, Amps/cm<sup>2</sup>

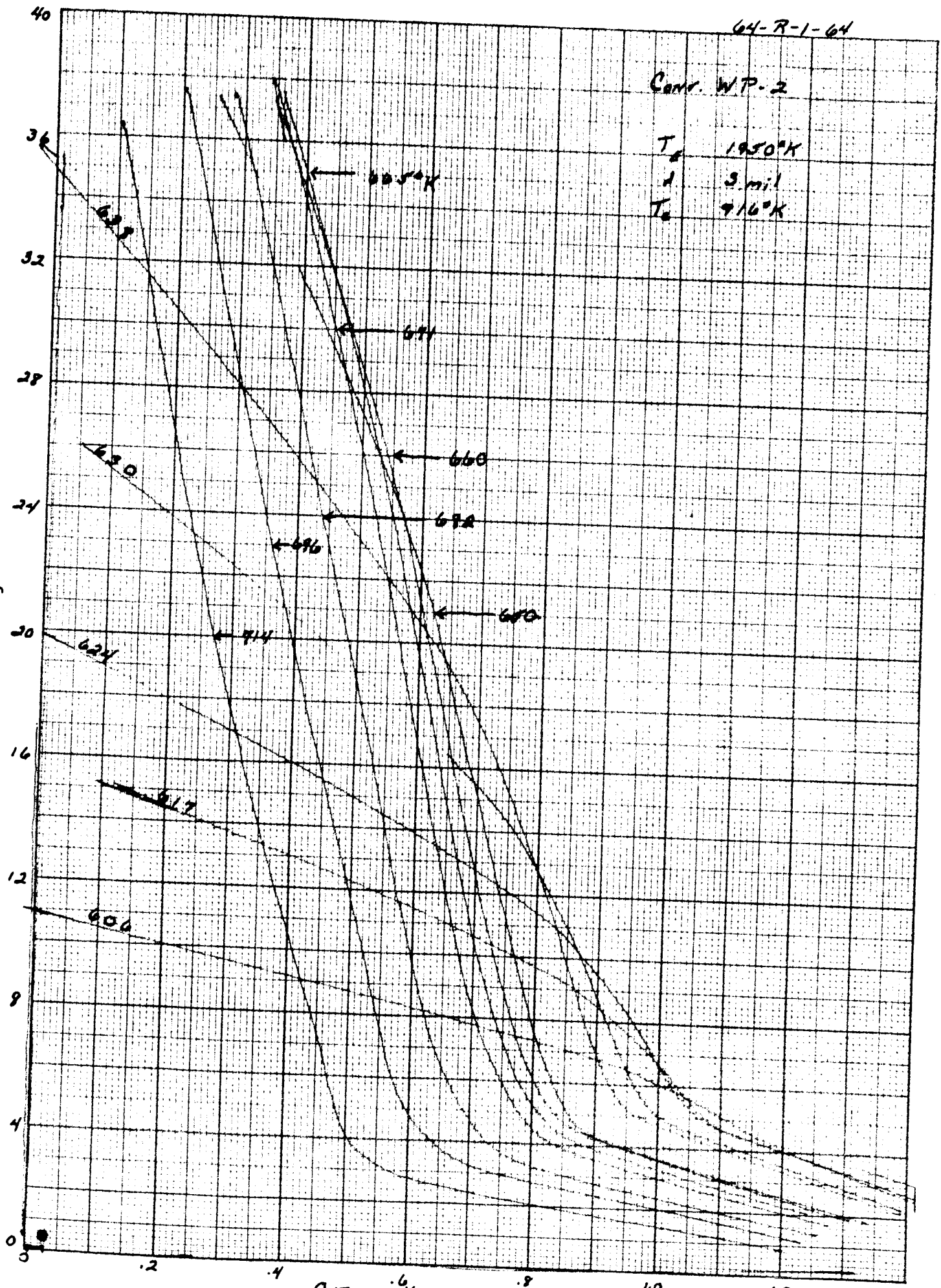


Fig. 1-20 F

359-1012G  
NEUFFEL & ESSER CO.  
MADE IN U.S.A.

64-R-1-65

Conv. WP-2

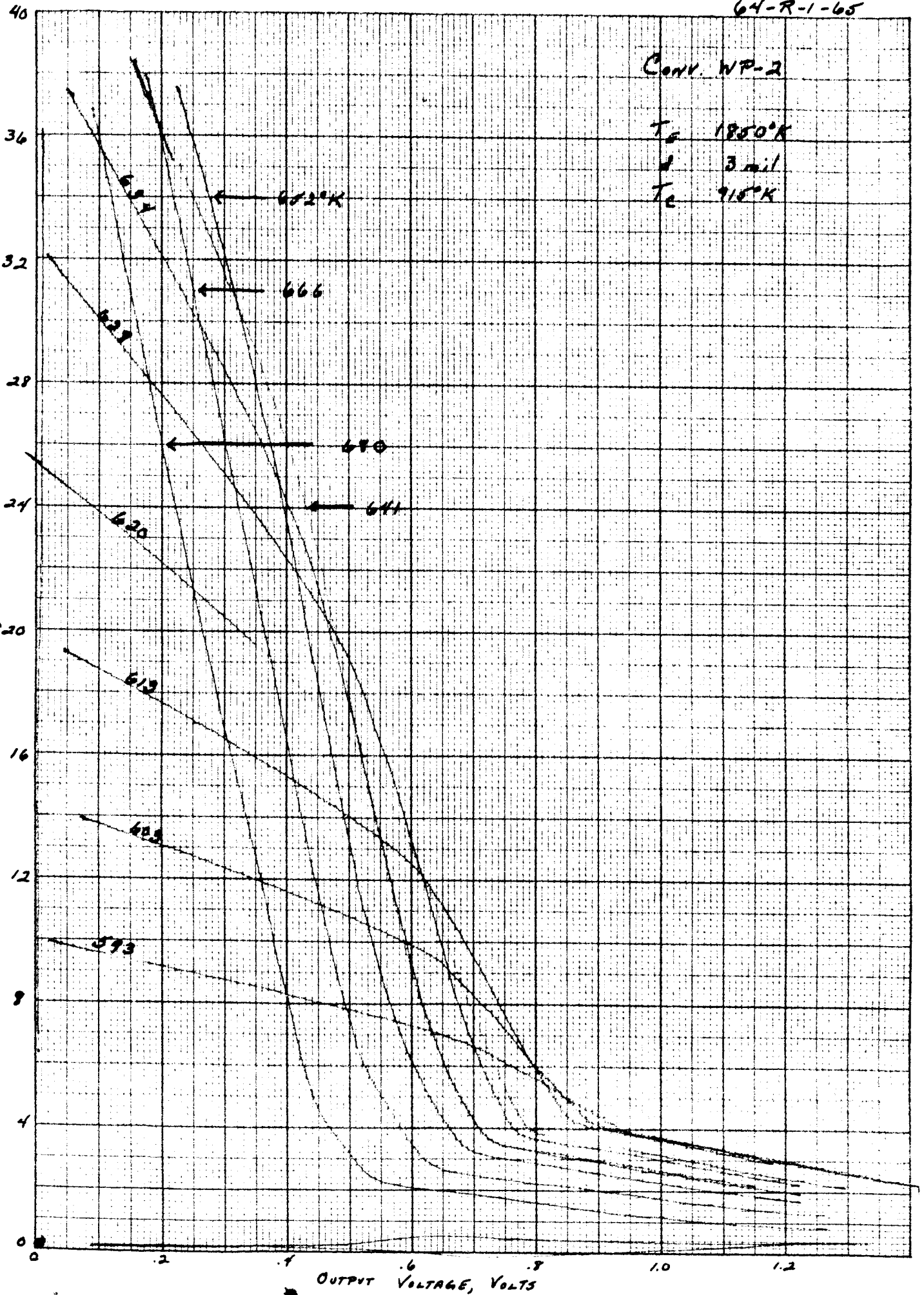
$T_c$  1850°K

$d$  3 mil

$T_c$  915°K

Current Density, Amps/cm<sup>2</sup>

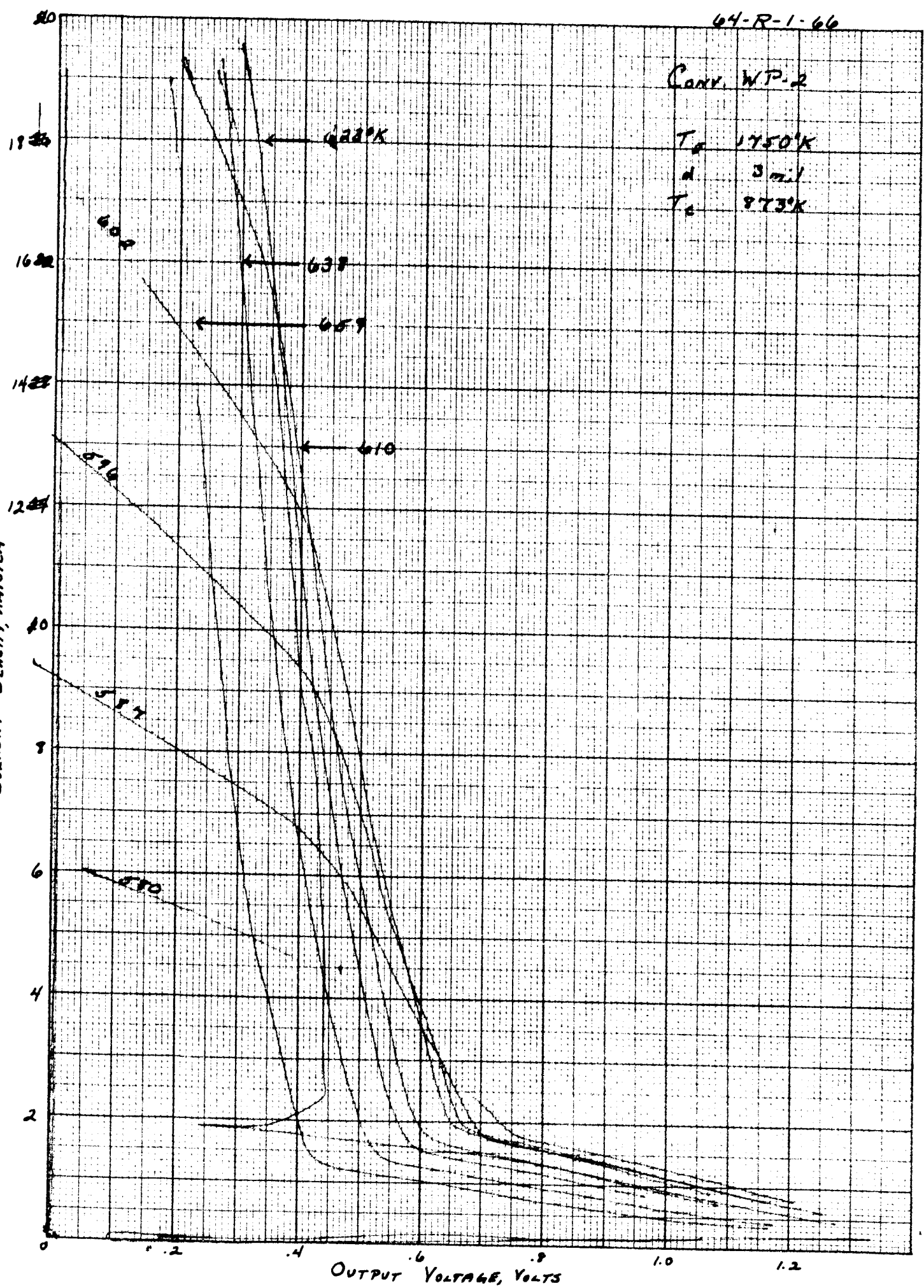
K&E 20X20 TO THE INCH 359,102 G  
KEUFFEL & ESSER CO. ROCHESTER, N.Y.





K&E 20X20 TO THE INCH 359-1017G KEUFFEL & ESSER CO. ALBANY, N.Y.

CURRENT DENSITY, AMP/CM<sup>2</sup>



64-R-1-66

Conv. WP-2

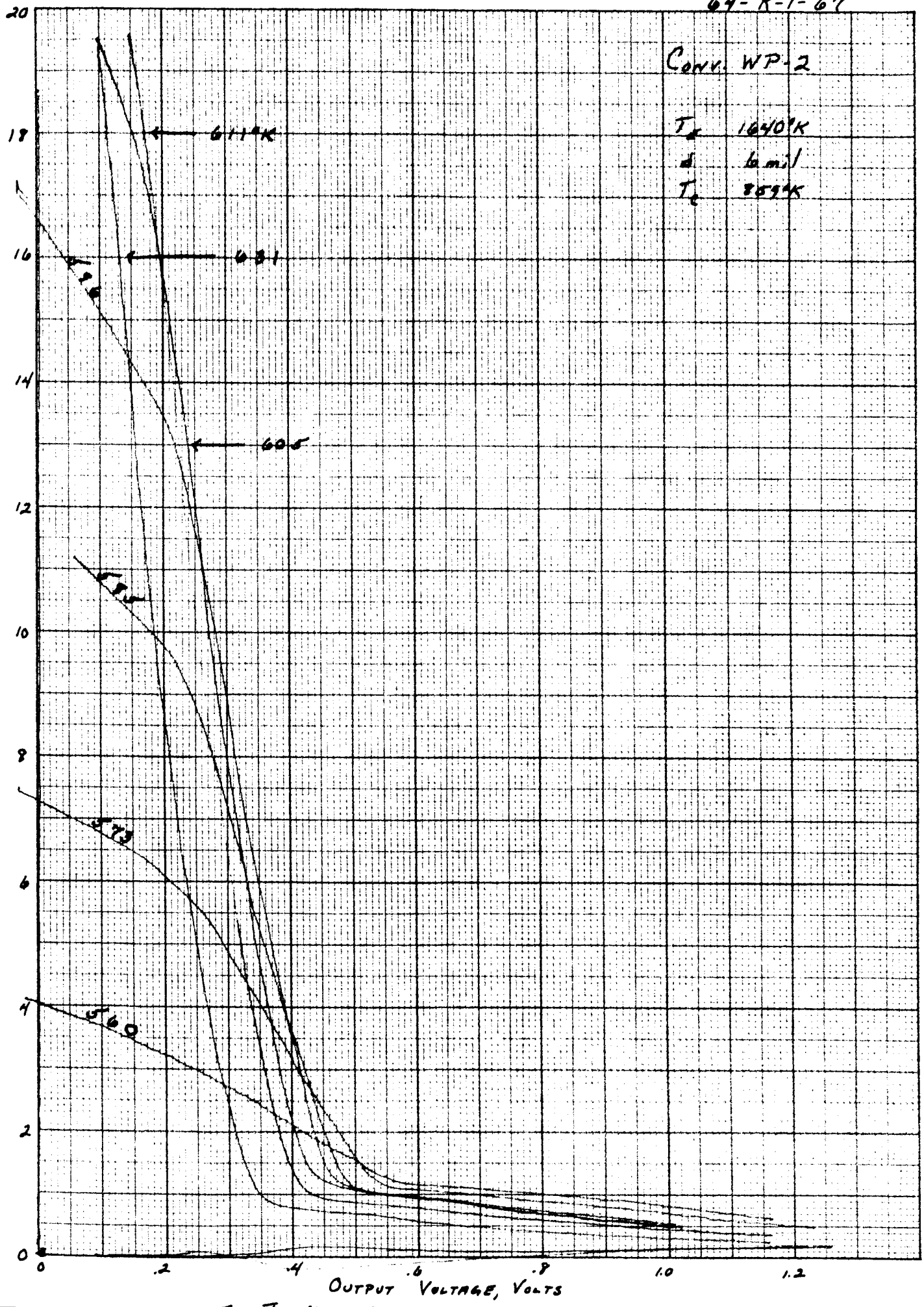
T<sub>e</sub> 1750°K

d 3 mil

T<sub>c</sub> 873°K

OUTPUT VOLTAGE, VOLTS

CURRENT DENSITY, AMPS/CM<sup>2</sup>



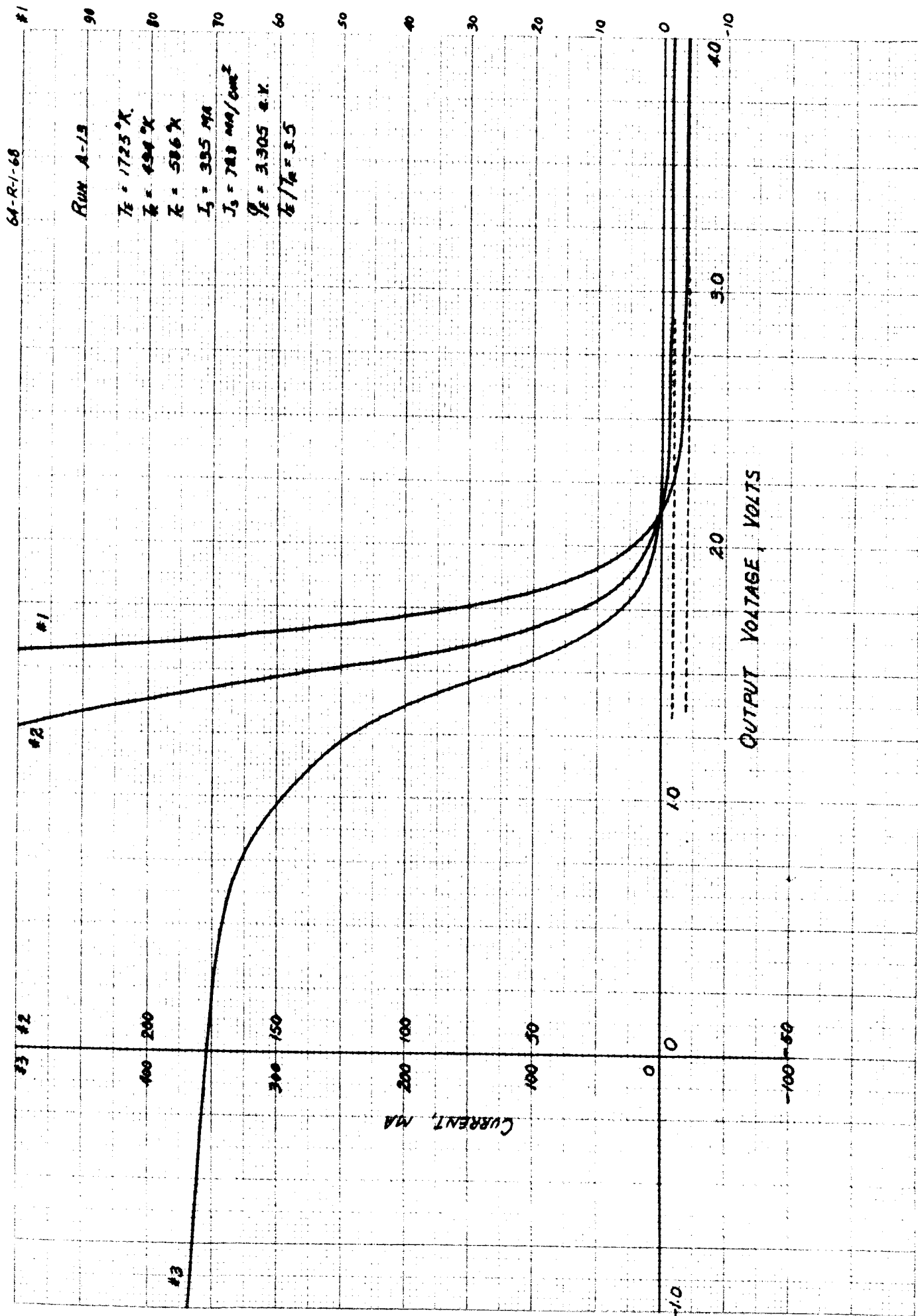
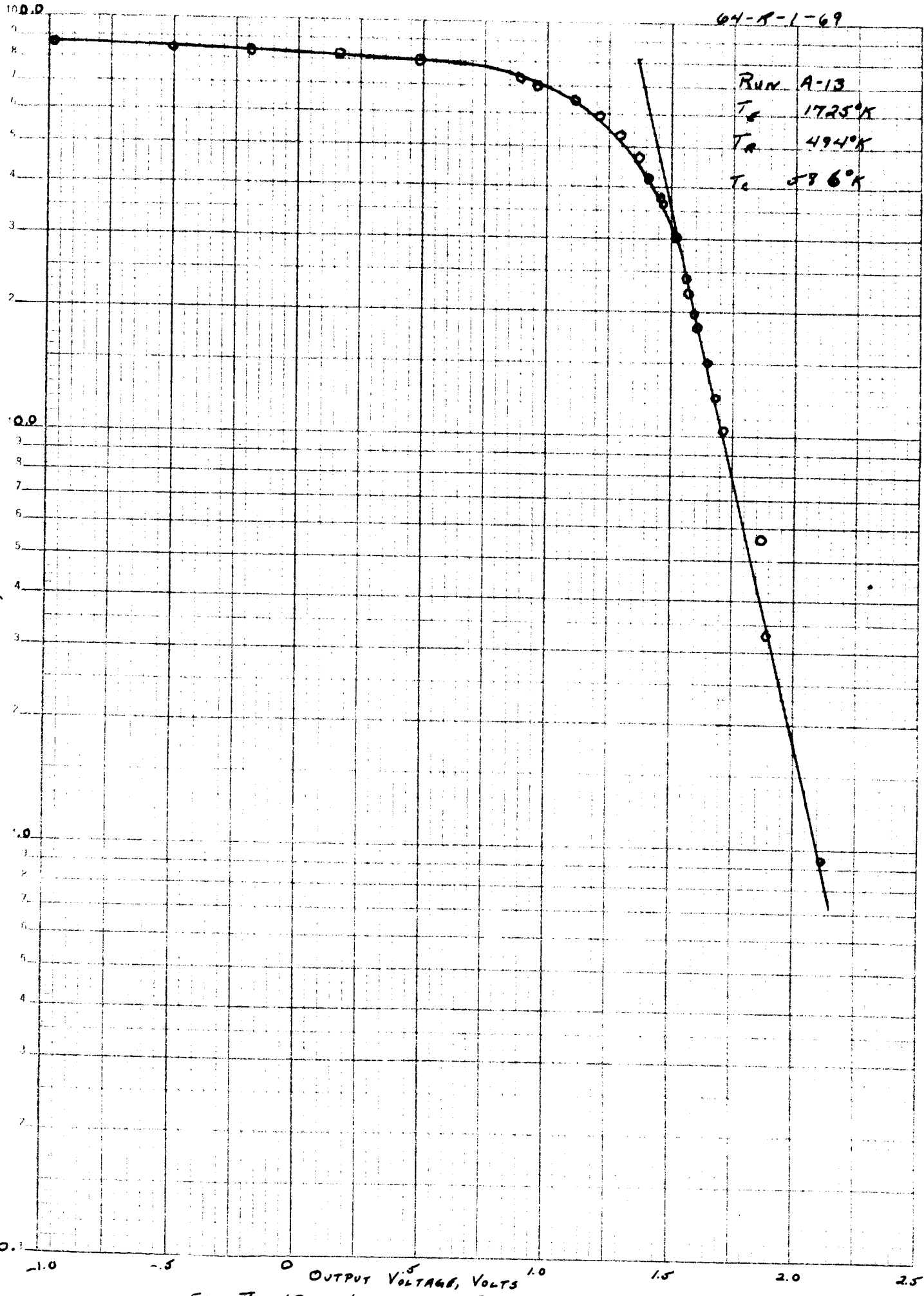
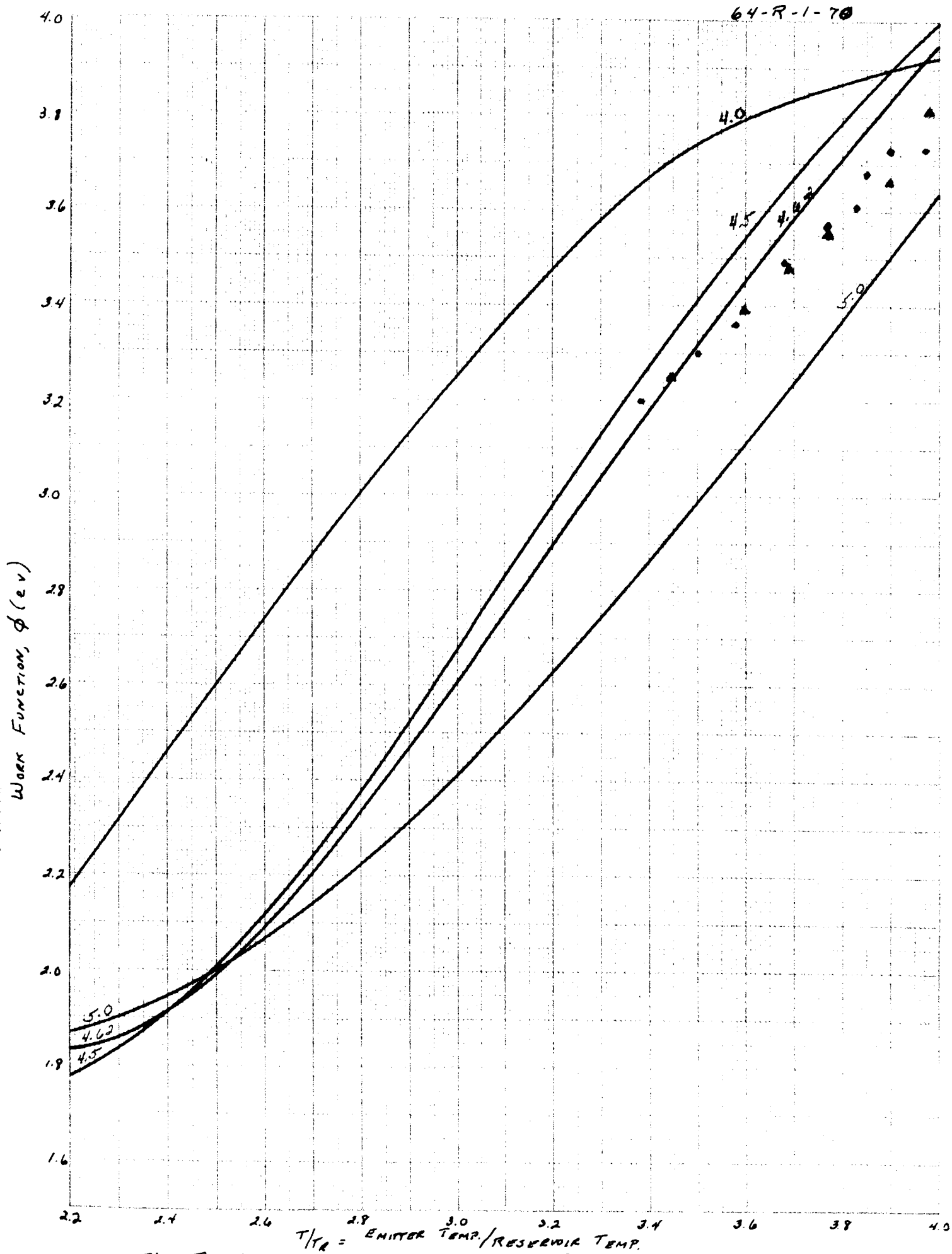


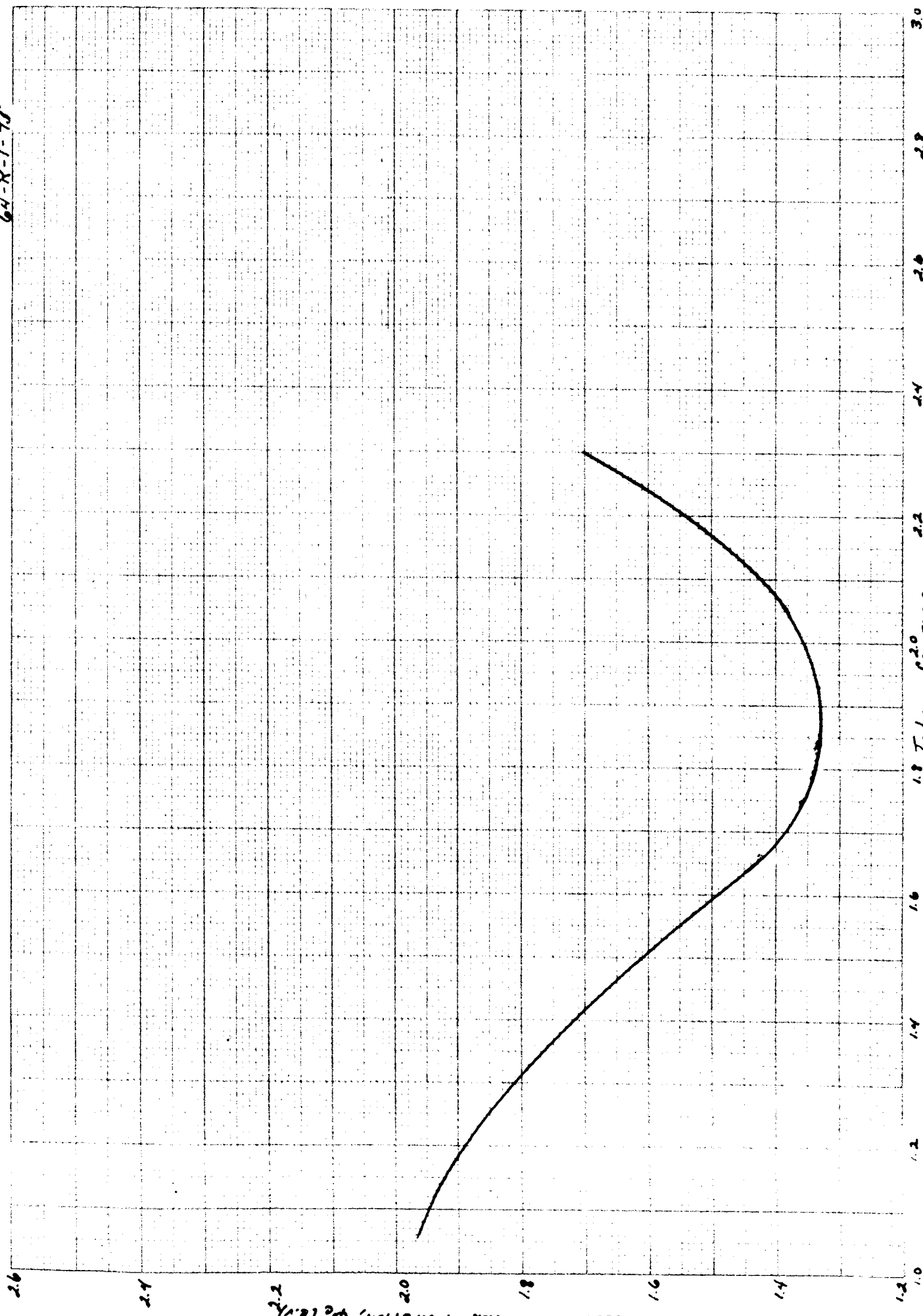
FIG II-42. TYPICAL I-V CURVE USED IN THE DETERMINATION OF  $\eta_E$  AND  $\eta_C$  LINEAR PLOT

CURRENT DENSITY, AMPS/CM<sup>2</sup>





64-R-1-7J



1.8  $T_c/T_R = \text{Collector Temp/Reservoir Temp}$   
 2.2  $T_c/T_R = \text{Collector Temp/Reservoir Temp}$   
 2.4  $T_c/T_R = \text{Collector Temp/Reservoir Temp}$   
 2.6  $T_c/T_R = \text{Collector Temp/Reservoir Temp}$   
 2.8  $T_c/T_R = \text{Collector Temp/Reservoir Temp}$   
 3.0  $T_c/T_R = \text{Collector Temp/Reservoir Temp}$   
 F. D. M. T. Collector Work Function Correlation



## CHAPTER VI

### METALLURGICAL STUDIES

#### A. GENERAL

This section of the work is intimately concerned with the energy of surfaces, and the following remarks are intended to illuminate the later part of the section. For a very complete discussion of this matter see "Metal Surfaces, Structure, Energetics, and Kinetics," Ed. Robertson & Gjostein, ASM 1963.

An ideally perfect cubic metal lattice is a regular array of charged atoms held in place by interatomic bonds. Consider breaking a crystal of such a metal along one of its simplest cube planes. This will produce two new free surfaces on which the interatomic bonds are unsatisfied. The surface energy of each new surface represents the energy of the unsatisfied bonds, and its value will depend on the interatomic bonding energy and the number of bonds broken per unit area of the surface.

Different planes through the crystal cut different numbers of bonds, in other words have different atomic densities.<sup>1</sup> So the surface energy, and also the work function, and some other physical properties, of a surface, will vary with its orientation with respect to the metal lattice.

Given a chance to equilibrate, the surface of a metal crystal will generally tend to a shape having minimum surface energy, but because the surface energy may vary with orientation (that is, be anisotropic), the equilibrium shape may be not part of a sphere but part of a polygon. See P. G. Shewmon<sup>2</sup> and Shewmon & Robertson.<sup>3</sup>

---

1. C. S. Barrett, Structure of Metals, p. 12, McGraw Hill, 1952.

2. P. G. Shewmon, Trans. AIME 227 400 (April 1963).

3. P. G. Shewmon & W. M. Robertson, Trans. AIME 224 804 (Aug. 1962).



Another factor that has to be taken into account in considering the tungsten surfaces under examination here is the presence of grain boundaries. Atoms in the bulk material have a minimum energy when arranged on the lattice points at the corners of a cube network. Atoms displaced from these positions have a higher energy. So the atoms comprising a grain boundary, being in non-equilibrium positions, have a higher energy than their neighbors in the bulk material. This is why etching attacks grain boundaries first. If two zones in the crystal have almost the same orientation, the atoms in the boundary between them will be only slightly displaced from equilibrium, and for larger mis-orientations the grain boundary atoms will be further displaced and have a higher energy. A more detailed analysis<sup>4</sup> leads to the expression  $E = \theta(A \log \theta)$  for the energy  $E$  per unit length of boundary as a function of a constant  $A$  (related to the strain energy at the centre of a dislocation) and the angular mis-orientation across the boundary,  $\theta$ . This curve rises with  $\theta$  over the range of angles less than  $\pi/2$  for which it is a good approximation.<sup>5</sup>

Now at temperatures at which these specimens were tested, atoms on the surface are relatively mobile. Mullins<sup>6</sup> has discussed the behavior of grain boundaries under conditions in which surface diffusion predominates over the evaporation/condensation mechanism for material transfer. He explains that the point where the grain boundary intersects the free surface tends to change shape in order that the grain boundary tension may equilibrate with the surface tension, and that the earliest alteration in shape produces sharp ridges that border each side of the boundary. These ridges then have an excess chemical

---

4. W. T. Read & W. Shockley, Phys. Rev. 78 275 (1950).

5. A. H. Cottrell, Theoretical Structural Metallurgy, pp. 89-97 (1953), St. Martin's Press, London.

6. W. W. Mullins, J. Appl. Phys. 28 333 (Mar. 1957).





potential over the neighboring material, caused by their small edge radius, and this chemical potential is the driving force for diffusion, which tends to flatten them. The flattening upsets the equilibrium groove angle, and forces the groove to deepen. Using certain assumptions, he shows that surface diffusion leads to the formation of a ridge above the original surface and remote from the boundary, which persists indefinitely with further heating. This treatment neglects anisotropy in surface energy, and concludes that surfaces close to a grain boundary are unstable with time. The enhanced chemical potential of the sharp edges of etch pits is responsible for the surface diffusion which changes the profile as indicated in Figure 34 of the Third Quarterly Report.

A further factor appears to be significant for low-energy boundaries; any deviation of the surface from its original plane is accompanied by an increase in surface area, and therefore in surface energy (again neglecting anisotropy), and so the tendency of a boundary to form a boundary groove is opposed by its tendency to minimize surface area. For this reason a low-energy boundary, initially visible, may disappear on heating. This is what seems to have happened on certain specimens in this work, where many of the boundaries are small-angle low-energy boundaries.

## B. EXPERIMENTAL RESULTS

Work on  $\text{Ag}^7$  and  $\text{Fe}^8$  has shown that facets may be developed by suitable firing, of a size clearly visible with an optical microscope. Except for the behavior of etch pit bottoms, mentioned in Chapter 3 of the Third Quarterly

---

7. G. E. Rhead, Aeta Met 11 1035 (Sept. 1963).

8. J. M. Blakeley & K. Mykura, Aeta Met 11 399 (May 1963).



Report, the experiments performed here have given no evidence for the preferential development of certain flat surfaces. Electron-micrographs of the surfaces of these specimens have been quite unrevealing, and have not contradicted the optical observations, but the techniques available to us leave room for improvement, and this should not be taken as the last word.

Evidence that otherwise undetected and invisible changes may be taking place comes from the considerable difference in performance between an old polycrystal tungsten diode built for ONR in 1962, and a more recent polycrystal tungsten diode made for this program in 1963. The latter diode was designed and the emitter prepared using special metallurgical techniques. It was felt to be desirable to have a performance as uniform as possible during the life of the diode, and since the condition of the surface was expected to change on heating, it was decided to try to achieve such changes before diode assembly rather than during operation. To this end, the emitter was fired in vacuum for 1/2 hour at 2300° C before assembly into the diode. As the old ONR emitter was inserted into its diode after a simple mechanical polish, and this was the main difference in the preparation of the two emitters, it is suspected that the pre-assembly stabilization was responsible for superior later performance of the current diode, but this is not established beyond all reasonable doubt; rather, it is a suspicion which leads us to stabilize all new emitters before assembly.

In the Second Quarterly, Chapter 5, Section B, it was stated that "hot checks" were left on the surfaces of the diode as a result of grinding, but that these were superficial. Further experience showed that the markings were in fact small-angle grain boundaries, created during the crystal-growing operation, and so they persisted during polishing.



In the conditions in which these specimens were fired, evaporation from the tungsten occurred, at a rate varying between a few Angstroms per hour at 2100° C and 13.7  $\mu$  in 21 hours at 2670° C. The latter amount is over half a mil; the specimen from which this evaporated is that illustrated in Figure 12 of the Third Quarterly Report, and here there is no evidence of facets or preferential evaporation, where it would be most expected to show. So preferential evaporation does not seem to be operating to produce any facets or steps on these surfaces.

The anomalous surface illustrated in Figure 20 of the Second Quarterly Report is attributed to not electropolishing enough to remove the work-damaged layer. Subsequent firing caused it to roughen under the influence of residual work damage. This phenomenon was not reproduced in other specimens.

### C. CONCLUSIONS

No optical-microscope observations have shown visible faceting. However, in three distinct cases, thermal treatment has developed surfaces with an average work function of 4.62 eV  $\pm$  0.05 eV. These are:

- (1) JPL polycrystalline emitter, in converter and scanner
- (2)  $\langle 110 \rangle$  emitter, in converter and scanner
- (3)  $\langle 110 \rangle$  and  $\langle 111 \rangle$  sectors of patchwork emitter.

In the light of this evidence, it seems possible that sub-microscopic faceting is occurring; there is no evidence to support this hypothesis at present, and further more sophisticated experiments are needed to elucidate this point.